

**ROLL-TO-ROLL FABRICATION OF CELLULOSE NANOCRYSTAL
NANOCOMPOSITE FOR GAS BARRIER AND THERMAL
MANAGEMENT APPLICATIONS**

by

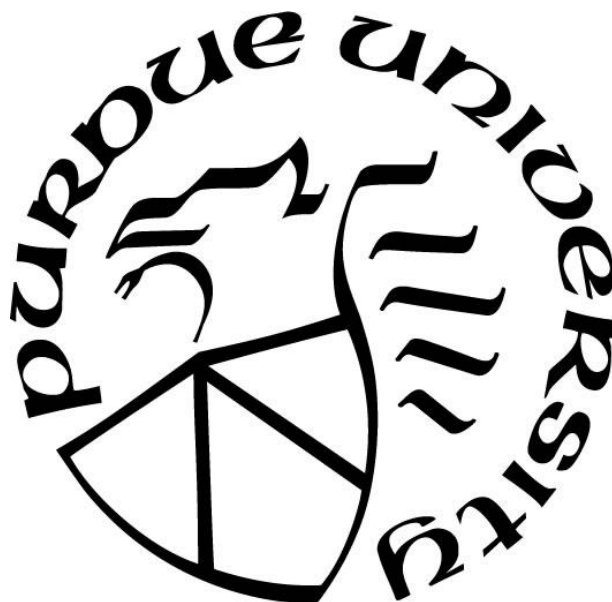
Reaz Ahmed Chowdhury

A Dissertation

Submitted to the Faculty of Purdue University

In Partial Fulfillment of the Requirements for the degree of

Doctor of Philosophy



School of Materials Engineering

West Lafayette, Indiana

May 2019

THE PURDUE UNIVERSITY GRADUATE SCHOOL
STATEMENT OF COMMITTEE APPROVAL

Dr. Jeffrey P. Youngblood, Chair

School of Materials Engineering

Dr. Pablo D. Zavattieri

Lyles School of Civil Engineering

Dr. Alexander Wei

Department of Chemistry

Dr. George T. C. Chiu

School of Mechanical Engineering

Approved by:

Dr. David Bahr

Head of the Graduate Program

Dedicated
To
Almighty the Creator

ACKNOWLEDGMENTS

First of all, I would like to express my deepest gratitude to my advisor, Prof. Jeffrey P. Youngblood, for his constant guidance throughout the thesis work and being a chair for this thesis committee. This work would not have been possible without his novel idea, constructive comments, and insightful suggestions despite of his busy schedule.

I am very thankful to my committee members, Prof. Alexander Wei, Prof. Pablo D. Zavattieri, and Prof. George T. C. Chiu for their expertise and holding me to a high standard.

This work would not be possible without the help of Dr. Jairo Diaz, Dr. Shane Peng, Dr. Gamini Mendis, Dr. Youngman Yoo, Dr. Francisco Montes, Shikha Shrestha, Caitlyn M Clarkson and a lot of other graduate students.

Finally, I would like to thank my family for supporting me throughout these four years, especially my wife, Samia Islam, for sacrificing so much for me so I could pursue my career.

This work has been supported by National Science Foundation Scalable Nanomanufacturing program under Award CMMI-1449358.

TABLE OF CONTENTS

LIST OF TABLES	8
LIST OF FIGURES	9
ABSTRACT	11
CHAPTER 1. INTRODUCTION	13
1.1 Background and motivation	13
1.2 Research objective	14
1.3 Overview of this work	15
CHAPTER 2. CONTINUOUS ROLL-TO-ROLL FABRICATION OF TRANSPARENT CELLULOSE NANOCRYSTAL (CNC) COATINGS WITH CONTROLLED ANISOTROPY	16
2.1 Introduction.....	16
2.2 Experiments	18
2.2.1 Materials and ink formulation	18
2.2.2 Substrate and ink compatibility	19
2.2.3 Film fabrication	19
2.2.4 Film characterization	20
2.2.5 Adhesion test	20
2.2.6 Surface morphology.....	21
2.2.7 Anisotropy measurement	21
2.3 Results and Discussion	22
2.3.1 Coating thickness control	22
2.3.2 Effect of film thickness on coating adhesion.....	30
2.3.3 Effect of CNC concentration on surface morphology and optical transparency	32
2.3.4 Gravure rotational effect on anisotropy (nematic configuration)	37
2.4 Summary	40
CHAPTER 3. ROLL-TO-ROLL FABRICATION OF CELLULOSE NANOCRYSTAL- POLY(VINYL ALCOHOL) COMPOSITE COATINGS WITH CONTROLLED ANISOTROPY	42
3.1 Introduction.....	42

3.2	Experimental section.....	45
3.2.1	Materials and Methods	45
3.2.2	Surface tension measurements.....	46
3.2.3	Coating equipment.....	47
3.2.4	Film characterization	47
3.2.5	Adhesion test	48
3.2.6	Surface roughness and 3D topography characterization	48
3.2.7	Anisotropy measurement	48
3.2.8	Water vapor transmittance rate	49
3.3	Results and discussion	50
3.3.1	Coating process.....	50
3.3.2	Coating characterization	53
3.3.2.1	Surface roughness and coating transparency	53
3.3.2.2	Coating adhesion strength	56
3.3.3	Effect of CNC loading on coating anisotropy	58
3.3.4	Water vapor transmission rate (WVTR).....	63
3.4	Summary	65
CHAPTER 4. CELLULOSE NANOCRYSTAL (CNC) COATINGS WITH CONTROLLED ANISOTROPY AS HIGH-PERFORMANCE GAS BARRIER FILMS		67
4.1	Introduction.....	67
4.2	Experimental	69
4.2.1	Materials and film fabrication	69
4.2.2	Film characterization	71
4.2.3	Gas permeability measurement.....	72
4.3	Results and discussion	73
4.3.1	Orientation of crystalline domains in bulk cellulose nanomaterials.....	73
4.3.2	Gas permeability in cellulose nanomaterials	74
4.3.3	Bharadwaj model and its modification for the CNC system	77
4.3.4	Bharadwaj model for the prediction of gas permeability.	80
4.3.5	Comparison with other materials.....	83
4.4	Summary	85

CHAPTER 5. SUPERIOR, PROCESSING-DEPENDENT THERMAL CONDUCTIVITY OF CELLULOSE NANOCRYSTAL-POLY(VINYL ALCOHOL) COMPOSITE FILMS	86
5.1 Introduction.....	86
5.2 Experimental	90
5.2.1 CNC Film Preparation and CNC Alignment Characterization.....	90
5.2.1.1 Film fabrication:	90
5.2.1.2 Orientation measurement:.....	90
5.2.2 Phase morphology of the composite films.....	91
5.2.3 Thermal conductivity measurement	92
5.3 Results and discussion	95
5.3.1 Effect of (CNC: PVA) composition with isotropic configuration.....	95
5.3.2 Effect of anisotropy for different (CNC: PVA) composition	100
5.3.3 Effective Medium Theory – Choy & Young (EMT-CY) Model applied to CNC-PVA composite thin films	105
5.4 Summary	110
CHAPTER 6. CONCLUSION AND FUTURE WORK	112
6.1 Roll-to-roll CNC coating	113
6.2 Roll-to-roll CNC-PVA composite coating.....	113
6.3 Barrier performance of CNCs thin films	113
6.4 Thermal conductivity of CNC-PVA thin films.....	114
APPENDIX A.....	115
APPENDIX B	123
APPENDIX C	133
APPENDIX D.....	141
REFERENCES	147
VITA.....	159

LIST OF TABLES

Table 2-1 Roughness measurements as a function of CNC content	34
Table 3-1 Coating formulations for different compositions	51
Table 3-2 WVTR with corresponding order parameter for different CNC-PVA coating compositions on a PLA substrate.....	65
Table 4-1 Different parameters of the Nanocellulose films with corresponding crystalline domains arrangement.....	74
Table 5-1 Thermal conductivity for different polymer/polymer nanocomposite systems	105

LIST OF FIGURES

Figure 2.1 The effect of roller speed for a constant web speed (1m/min) [line added to aid the eye].	23
Figure 2.2 The effect of roller speed for a constant web speed (1m/min) [line added to aid the eye].	25
Figure 2.3 The effect of speed ratio on the coating thickness for three CNC suspensions [Nonlinear regression based on 2 parameter rectangular hyperbola].	25
Figure 2.4 Rheological properties of 12wt%, 9wt% and 6wt% CNC suspensions.	27
Figure 2.5 3D mesh plot with corresponding contour plot for 12wt% (A-a), 9wt% (B-b), and 6wt% (C-c) CNC coating.	29
Figure 2.6 Crosshatch peel adhesion strength of 12wt%, 9wt% and 6wt% at varying coating thickness.	31
Figure 2.7 Surface morphologies of coatings from suspensions of A) 12 wt% CNC, B) 9wt%, and C) 6wt%.	34
Figure 2.8 Photographs of CNC coatings on PET substrate (15cmX15cm): (top left) PET substrate, (top right) 12wt% CNC solution, (bottom left) 9wt%, (bottom right) 6wt%.	36
Figure 2.9 Optical transparency for different CNC coated PET films.	36
Figure 2.10 Order parameter variation with roller speed (substrate speed= 1m/min) [Nonlinear regression based on a piecewise linear approximation].	38
Figure 2.11 CNC particles diffusion with different CNC concentrations. Here, scale bar= 0.5mm.	39
Figure 3.1 Surface tension for different CNC-PVA ink systems.	51
Figure 3.2 Rheological behavior of CNC-PVA ink composition at variable shear rates	52
Figure 3.3 Surface roughness of uncoated PET and CNC-PVA coatings on PET substrate.	54
Figure 3.4 Optical transparency for different CNC-PVA composition on PET films.	55
Figure 3.5 Photograph for CNC-PVA coatings on PET substrate (15 cm x 15 cm)	56
Figure 3.6 Adhesion strength for coatings.	57
Figure 3.7 Order parameter for different coating system	59
Figure 3.8 Apparent viscosity for CNC-PVA (12wt% solid loading) nanocomposites system with different CNC percentage at 300 s ⁻¹ shear rate (line added to aid the eye).	60
Figure 3.9 Real time birefringence observation for different ink compositions.	61

Figure 3.10 WVTR with corresponding order parameter for different CNC-PVA coating compositions on a PLA substrate.....	64
Figure 4.1 Permeability of cellulose nanomaterials. Here, red circle and blue circle area are denoted for isotropic and anisotropic CNCs, respectively, with higher barrier anisotropic CNC materials having higher progressively higher anisotropy. Literature data was based on pristine cellulose materials ¹⁴²⁻¹⁴³ , but no information was available regarding orientation or packing density.	75
Figure 4.2 Comparison of the modified Bharadwaj model data with experimental data for oxygen and carbon dioxide fit with either (a) chiral nematic as $S=0$ or (b) regression to $S=0$	81
Figure 4.3 Ashby plot of gas permeability response of cellulose films with various structural arrangements with respect to other engineering polymers. Details of quantitative data for this plot can be found in the Appendix C (Table CS1).....	84
Figure 5.1 Annotated 3D drawing of the measurement stage. Silver paint for affixing the sample not shown	93
Figure 5.2 Thermal conductivity of un-sheared CNC:PVA films versus CNC content of final film. Data shown is for 1, 5, and 10.7 initial CNC and PVA weight percent used during fabrication. The PVA molecular weight was 124-186K	97
Figure 5.3 Thermal conductivity of un-sheared CNC:PVA films versus CNC content of final film. Data shown is for 1, 5, and 10.7 initial CNC and PVA weight percent used during fabrication. The PVA molecular weight was 89-98K	98
Figure 5.4 Effect of PVA for reducing the interfacial resistance between CNC domains. Here, point A is showed for interfacial contact position where phonon can diffuse from one crystal to another crystal. (red arrow sign is denoted for the sum of every phonon vector projection in the chain direction of individual crystalline domain).....	100
Figure 5.5 In-plane thermal conductivity in the direction of shear of CNC-PVA nanocomposites with various degrees of orientation. S is Hermans order parameter for CNC-PVA nanocomposite system	102
Figure 5.6 Effect of PVA for reducing the interfacial resistance between CNCs for anisotropic composites. Here, point A is shown for the interfacial contact position where phonons can diffuse from one crystal to another crystal. (red arrow sign is denoted for the sum of every phonon vector projection in the chain direction of individual crystalline domain).....	104
Figure 5.7 Experimental κ of anisotropic CNC-PVA composite films shown along with results from the EMT-CY model as a function of S . The weight % of CNC is not in particular order. The stars represent the extrapolated values of κ obtained from the EMT-CY model at $S \approx 1$	107
Figure 5.8 Thermal images of CNC-PVA composites a) 100 % PVA sample with low κ , and b) 90:10 CNC:PVA sample with high κ during Joule heating of a serpentine metallic heater simulating flexible electronics elements. c) Line scans along the centerline of a) and b) quantify the temperature reduction associated with the high κ sample at the same Joule heating power (175 mW). Inset: Photograph of 90:10 CNC:PVA sample with shadow-evaporated metallic heater.	110

ABSTRACT

Author: Chowdhury, Reaz, A. PhD

Institution: Purdue University

Degree Received: May 2019

Title: Roll-to-Roll Fabrication of Cellulose Nanocrystal Nanocomposite for Gas Barrier and Thermal Management Applications.

Committee Chair: Dr. Jeffrey P. Youngblood

Cellulose nanocrystals (CNCs) and its composite coatings may impart many benefits in packaging, electronic, optical, etc. applications; however, large-scale coating production is a major engineering challenge. To fill this knowledge gap, a potential large-scale manufacturing technique, roll-to-roll reverse gravure processing, has been described in this work for the manufacture of CNC and CNC-poly(vinyl alcohol) (PVA) coatings on a flexible polymer substrate. Various processing parameters which control the coating structure and properties were examined. The most important parameters in controlling liquid transfers were gravure roll, gravure speed, substrate speed, and ink viscosity. After successful fabrication, coating adhesion was investigated with a crosshatch adhesion test. The surface roughness and morphology of the coating samples were characterized by atomic force microscopy and optical profilometer. The Hermans order parameter (S) and coating transparency were measured by UV–Vis spectroscopy. The effect of viscosity on CNC alignment was explained by the variation of shear rate, which was controlled by the micro-gravure rotation. Finally, the CNC alignment effect was investigated for gas barrier and thermal management applications.

In packaging applications, cellulose nanomaterials may impart enhanced gas barrier performance due to their high crystallinity and polarity. In this work, low to superior gas barrier pristine nanocellulose films were produced using a shear-coating technique to obtain a range of anisotropic films. Induction of anisotropy in a nanocellulose film can control the overall free

volume of the system which effectively controls the gas diffusion path and hence, controlled anisotropy results in tunable barrier properties. The highest anisotropy materials showed a maximum of 900-fold oxygen barrier improvement compared to the isotropic arrangement of nanocellulose film. The Bharadwaj model of nanocomposite permeability was modified for pure nanoparticles, and the CNC data were fitted with good agreement. Overall, the oxygen barrier performance of anisotropic nanocellulose films was 97 and 27 times better than traditional barrier materials such as biaxially oriented poly(ethylene terephthalate) (BoPET) and ethylene vinyl alcohol copolymer (EVOH), respectively, and thus could be utilized for oxygen-sensitive packaging applications.

The in-plane thermal conductivity of CNC - PVA composite films containing different PVA molecular weights, CNC loadings and varying order parameters (S) were investigated for potential application in thermal management of flexible electronics. Isotropic CNC - PVA bulk films with 10-50 wt% PVA solid loading showed significant improvement in thermal conductivity compared to either one component system (PVA or CNC). Furthermore, anisotropic composite films exhibited in-plane thermal conductivity as high as $\sim 3.45 \text{ W m}^{-1} \text{ K}^{-1}$ in the chain direction, which is higher than most polymeric materials used as substrates for flexible electronics. Such an improvement can be attributed to the inclusion of PVA as well as to a high degree of CNC orientation. The theoretical model was used to study the effect of CNC arrangement (both isotropic and anisotropic configurations) and interfacial thermal resistance on the in-plane thermal conductivity of the CNC-PVA composite films. To demonstrate an application for flexible electronics, thermal images of a concentrated heat source on both neat PVA and CNC-PVA composite films were taken that showed the temperature of the resulting hot spot was lower for the composite films at the same power dissipation.

CHAPTER 1. INTRODUCTION

1.1 Background and motivation

Petroleum-based, synthetic polymers are one of the dominant classes of raw materials used extensively across many industrial applications due to its low cost, easy processability, and superior performance. However, the imminent depletion of the petroleum-based resources and its long-lasting, adverse environmental effects are the primary reason for the development of next-generation raw materials. Ideally, next generation materials should be environmentally sustainable, renewable, and compatible with traditional engineering polymers. Bio-based raw materials may be an excellent alternative as they are easily compostable, renewable and environmentally friendly with a low carbon footprint¹⁻⁴.

Cellulose is the most abundant bioderived polysaccharides on earth. The main sources of cellulose raw materials are based on extraction from natural resources such as: wood, cotton, hemp, jute, straw, bacteria or algae⁵. The extracted cellulose fibers consist of both amorphous and crystalline components⁶. The acid hydrolysis of amorphous regions form rod-shaped, nano-sized anisotropic particles that are known as cellulose nanocrystals (CNCs). Based on sources and extracted methods, CNCs have variable aspect ratio (3 - 10 nm wide and 50 - 500 nm length), surface areas (30 - 600 m²/g), and crystallinity index (60 - 80 %)⁷⁻⁸. The individual domain of a cellulose nanocrystal is composed of multiple parallel stack of cellulose chains with intra/interchain hydrogen bonding. CNCs possess superior mechanical⁹⁻¹⁰, thermal¹¹, electrical insulation¹², gas barrier¹³, and optical¹⁴ properties compared to traditional engineering polymers; hence, the global scientific community is working on cellulose nanomaterials to validate its industrial applications in packaging, automobile, thermal management, and optical industries^{5, 15-}

The overall performance of CNCs is very promising, however, industrial application of such materials is very limited. The absence of scalable manufacturing techniques is one of the major reasons for this limitation. Roll to Roll (R2R) manufacturing is a continuous film fabrication technique that is extensively used in industrial scale production. For example, the R2R gravure system is utilized in the fabrication of flexible thin films, polymer solar cells, and flexible electronic devices¹⁹⁻²¹. However, the R2R manufacturing process requires coating formulation, substrate selection, ink-substrate compatibility, selective drying rate and controlled web speed for a defect free fabrication²²⁻²⁴.

1.2 Research objective

The aim of this study is total develop a large-scale manufacturing method for CNCs and its nanocomposite flexible coatings, to characterize the overall coating quality regarding nanostructured compositions, and to investigate the coating materials for gas barrier and thermal management applications. In particular, the specific objectives are listed below:

1. Develop a R2R microgravure process for CNC and CNC nanocomposites coatings on flexible substrates and characterize different process parameters such as coating formulations, gravure speed, speed ratio and substrate speed to control the liquid transfer rate and the coating thickness.
2. Investigate the coating quality to demonstrate the industrial grade coating properties from CNCs and its nanocomposites and examine the effect of coating formulations on adhesive strength, optical transparency, CNC orientation, and topographic properties of the coating materials.
3. Demonstrate the structure-property relationship of CNC orientation to control the effective free volume of the coating materials. In the process, examine the effect of packing density for the permeability of gas molecules through coating materials and validate its applicability for packing material. Also, explore the effect of anisotropy for in plane

phonon propagation through the coating materials and utilize for thermal management application

1.3 Overview of this work

In this work, pristine CNCs and CNC-poly(vinyl alcohol) (PVA) nanocomposites in an aqueous suspension are used as coating materials. The coating process is performed on flexible substrates like poly(ethylene terephthalate) (PET) and poly(lactic acid) (PLA). After a successful fabrication, characterization of the coating materials is performed to validate its possible application as gas barrier films and thermal conductive materials for flexible electronics. Chapter 1 demonstrates a roll-to-roll manufacturing process is presented for pristine CNCs suspension. Various process parameters are reported for a defect free coating fabrication. The effect of rheological property on the coating formulations is also investigated to validate the coating thickness, roughness, adhesive strength and CNC alignment of the coating materials. Chapter 2 describes the effect of CNC content on coating anisotropy for CNC-PVA nanocomposites. The isotropic-anisotropic coating transformation is correlated with shear from the process parameter (gravure rotation) and relaxation time of the coating formulations. Chapter 3 features the effect of packing density of pristine CNCs for effective control of gas permeability (i.e. gas molecule diffusion through the coating materials). The tunable barrier properties of the CNC coating have been investigated to develop low to super gas barrier nanocellulose films. Chapter 4 describes a novel approach to control the phonon propagation through the CNC- PVA nanocomposites. The effect of anisotropy and thermal interfacial resistance of the nanocomposites is correlated to demonstrate a structure-property relationship of thermal conductivity in the CNC-PVA coating materials.

CHAPTER 2. CONTINUOUS ROLL-TO-ROLL FABRICATION OF TRANSPARENT CELLULOSE NANOCRYSTAL (CNC) COATINGS WITH CONTROLLED ANISOTROPY

All lab work except surface morphology (SEM and AFM) was performed by Reaz Chowdhury. All analysis except surface roughness was performed by Reaz Chowdhury with guidance by Prof. Jeffrey P. Youngblood. All writing was performed by Reaz Chowdhury with guidance and editing by Prof. Jeffrey P. Youngblood.

The following chapter contains content reproduced with permission from R. A. Chowdhury, C. Clarkson, and J. Youngblood, "Continuous roll-to-roll fabrication of transparent cellulose nanocrystal (CNC) coatings with controlled anisotropy," *Cellulose*, vol. 25, no. 3, pp. 1769-1781, 2018. Copyright 2018 Springer Science + Business Media.

2.1 Introduction

Cellulose nanocrystals (CNCs) are an alternative renewable material derived from abundant resources: wood, plants, algae, tunicate, bacteria, etc. CNCs have a rod-shaped anisotropic crystalline domain with excellent properties, such as non-toxicity, biodegradability, high specific strength, high thermal conductivity, and optical transparency^{5, 25-26}. Based on these remarkable properties, CNCs are applicable as a reinforcement component in nanocomposites²⁷⁻²⁹, transparent media in organic electronics³⁰, anti-counterfeiting in security applications³¹, and barriers in packaging applications³². CNCs can form a coating³³, film³⁴, aerogel³⁵ or foam³⁶ depending on the desired final application.

The mechanical, thermal and optical properties of CNC materials depend significantly on the structural arrangement of the crystalline domain^{34, 37-40}. Depending on the crystal domain organization, CNC materials can be isotropic or anisotropic where an anisotropic configuration can exhibit directional enhanced properties in the orientation direction. For example, a four-fold higher thermal conductivity in the aligned direction compared to the isotropic configuration has been reported²⁵. Anisotropic CNC nanocomposites can offer better properties such as higher

Young's elastic modulus, yield stress, and ultimate tensile strength with improved transparency, which is essential for gas barrier application⁴¹. Anisotropic CNC film also presents exceptionally low hygroscopic strain in the axial direction that is important for any electronic packaging application⁴².

Solution casting using mechanical shear force is the most common technique for anisotropic CNC film fabrication^{34, 38, 43-45}. Solution casting is a convenient and inexpensive small-scale processing technique, however high viscosity solutions are primarily used. High concentrations of CNC (and thus high viscosity solutions) allow for limited mobility of the CNCs during processing and therefore, the coating retains shear-induced anisotropy in its final structure. However, difficulties exist in achieving a uniform homogeneous thickness and the fabrication process is time consuming for such solutions (an hour to several days). Spin-coating overcomes this limitation, but large area processing is a challenge for this method⁴⁶. In this context, roll-to-roll manufacturing offers an inexpensive, fast process with large-scale continuous fabrication compared to other laboratory-scale processing techniques.

The roll-to-roll (R2R) manufacturing process is a versatile technique for the fabrication of flexible coatings, polymer solar cells, and flexible electronic devices^{19, 47-52}. Both printing and coating are possible in a roll-to-roll system, which can be coupled with slot-die, gravure, spray, inkjet, nanoimprinting, or rotary screen. In an R2R gravure process, ink is continuously transferred from an ink bath to the gravure cylinder. A doctor blade is placed over the gravure cylinder to remove the excess ink and maintain a constant uniform ink thickness. A thermoplastic, flexible polymer film is used as a substrate, which continuously moves between the two rolls. A liquid bridge between the gravure cavity and the web (substrate) that is stretched and sheared with a moving contact line is the basic mechanism of the ink transfer from the gravure to the web.

Typically, the wet liquid film then passes through a drying chamber and dried. The overall coating quality largely depends on the ink's compatibility with the substrate, gravure speed rate, web speed, drying unit, and solvent type. Gravure coating has been used to fabricate organic thin film transistors, light-emitting polymer diodes, organic photovoltaics, and electrochromic devices¹⁹.

Very limited work has been done using R2R with cellulose nanomaterials. Previous studies focused on pure CNF and CNF mixtures for thin or thick coating formations⁵³⁻⁵⁴. To the best of our knowledge, R2R micro-gravure has never been used for CNC based coatings. Accordingly, we use micro-gravure R2R to develop and report an industrial scale, anisotropic CNC film coating technique on a flexible PET substrate. In this work, we detail the role of process parameters such as roller speed, web speed, and viscosity on the coatings and report the effect of gravure rotation rate on the coating thickness and anisotropy.

2.2 Experiments

2.2.1 Materials and ink formulation

Flexible polyester films (MELINEX® 462 2 mil) were purchased from TEKRA (New Berlin, WI, USA) and used as a substrate. The substrate film, 1000 m in length and 15.24 cm in width, was installed on the roll-to-roll coating system. Never-dried, pristine CNC (12.2wt%, batch no-2015-FPL-071CNC) aqueous suspension purchased from the University of Maine (Orono, ME, USA) and manufactured by the USDA Forest Service-Forest Products Laboratory (FPL) (Madison, WI, USA), was used as ink in this investigation. The stock CNC aqueous solution was diluted with nano-pure water to a final concentration of 6wt%, 9wt%, and 12wt% CNC. Henceforth the ink was referred to as the pristine CNC suspension. Solutions were ultra-sonicated (at 50% amplitude with 60 Hz frequency) for 10 mins to disperse CNCs and homogenize solutions. Sonication introduced fluidity into solutions by destroying its gel structure and enabling their use as an active

ink system without any further formulation. The rheological measurements of the CNC suspension were performed on a shear controlled rotational rheometer (Malvern Bohlin Gemini HR Nano) equipped with a cup and bob fixture. The steady shear viscosity was measured for 100 μm gap distance and the shear rate range was 0.01-500 s^{-1} . All measurements were performed at room temperature.

2.2.2 Substrate and ink compatibility

Substrate-ink compatibility is the most important parameter for any printing or coating technique. In general, the surface energy of the substrate must be higher than the surface tension of the ink system. Flexible polyester films have lower surface energy (45 dynes/cm) compared to CNC dispersion surface tension (55-65 Dynes/cm)⁵⁵; hence, surface treatment is essential to overcome de-wetting issue. We utilized a high speed, high power corona treater system (QC electronics, Inc.) for substrate processing, which introduced a surface modification to increase the wettability of the substrate roll. Treatment speed rate as well as power supply dominated the overall surface modification. We observed that a substrate treatment with a 0.5 KW power supply and 2 m/min speed rate can produce 60-65 dynes/cm surface energy on the film, which is compatible with an aqueous CNC suspension.

2.2.3 Film fabrication

A Mirwec Mini-Labo DeluxeTM system (Figure AS1 in the APPENDIX A) with a tri-helical R30-microgravure system has been utilized for our gravure coating. The gravure coating includes a gravure roller, ink bath, flexible substrate, and drying chamber. A doctor blade was placed over the gravure cylinder to remove the excess ink and maintain a uniformly solution thickness. The nip distance was minimized between the gravure and the substrate to achieve complete liquid transfer. Fabrication processes were performed with a variable substrate speed (0.3-6 m/min), and

gravure speed (4rpm-70rpm), which controlled the overall coating thickness and quality. After a successful liquid transfer from the ink bath to the flexible substrate, the wet-coated region passed through an inline drying unit. The temperature of the heating chamber was 80°C for the entire gravure coating process, which allows for complete drying of the coating. After drying, the transparent CNC coated substrate was collected on the rewinder.

2.2.4 Film characterization

A Carl Zeiss (Axio observer A1) inverted light microscope was used in transmission mode for thickness measurements. Both 5X and 10X magnification objectives were used for film thickness characterization. A cut sample was placed perpendicularly between the objective and the stage and film thickness was measured. Polarized light optical microscopy was used to image coatings with samples at 45° and 90° with respect to the plane of polarized light.

The transparency of neat PET and CNC coated PET films were measured with a conventional UV-Vis spectrophotometer (Spectramax Plus 384, Molecular devices Corp., Sunnyvale, CA). The transmittance data for each film were measured across 400-750 nm wavelength with air as the background.

2.2.5 Adhesion test

CNC coating adhesion to the flexible substrate was studied with a cross-hatch adhesion test method (ASTM-D3359). Briefly, a 5X5 cm specimen was adhered to a glass plate with adhesive spray and left untouched for 30 mins for complete drying. With a sharp blade, 11 parallel and 11 perpendicular cuts were made on the sample with respect to the center of the film, where each cut was 1 mm apart. A pressure sensitive tape was placed over the film for 5 mins and removed from the surface at a 180° angle. The quantification of the adhesion loss via coating performance was categorized on a scale of 0-100%. Based on the ASTM D3359, samples were classified into 6

different categories as follows: 5B (0%), 4B (less than 5%), 3B (5-15%), 2B (15- 35%), 1B (35- 65%) and 0B (> 65%) where 5B is considered optimal with 0% area removed from the substrate. Both the flexible substrate and CNC coating were colorless, so the removal of the CNC coating from the grid area was investigated by polarized light microscopy.

2.2.6 Surface morphology

A Dimension 5000 Atomic force microscope (AFM) in tapping mode was used to examine surfaces of organic coatings on the polyester substrate. Inspire CT300R-25 conical cantilever AFM tips were purchased for film characterization from NanoScience Instruments, Phoenix, AZ, USA. Samples were prepared by cutting a section of the film from the middle of the coated section and adhering the strip to a metal puck. Two samples were selected for each condition (6wt%, 9wt%, and 12wt %) and three sections of 50 μm x 50 μm on each sample imaged. Films were fabricated under the same conditions at a speed ratio of 1. Films for AFM imaging showed no visual signs of microscopic defects when viewed under an optical microscope.

2.2.7 Anisotropy measurement

A conventional UV-vis spectrophotometer (Spectramax Plus 384, Molecular devices Corp., Sunnyvale, CA) was used for the characterization of the CNC alignment. We used a similar method as reported by Chowdhury et al. and details can be found there³⁸. Briefly, a sample was delaminated from the substrate and placed between a cross polarizer and the transmitted light intensity was measured at 45° and 90° configurations. The transmittance data was recorded from 400 nm to 750 nm wavelength. The following equations were used for the order parameter, S calculation:

$$I_{\theta} = I_0 \sin^2 2\theta \sin^2 \left(\frac{\pi \Delta n d}{\lambda} \right) \dots \dots \dots (2.1)$$

Hence,

$$\frac{I_{45}}{I_{90}} = D^* = D \cdot g = \frac{(2S+1)}{(1-S)} \dots \dots \dots (2.2)$$

Here, I_0 , θ , Δn , d , λ , I , g and D represent the amplitude of the incident light, the angle of the material between the cross-polarizer, refractive index difference, film thickness, wavelength, transmitted light intensity, correction factor and dichroic ratio, respectively. The parallel and perpendicular refractive indices are relatively low for cellulose; therefore, we adopt $g = 1$ for our calculation. The order parameter for any material is between 0 and 1, where $S=0$ is defined as an entirely random/ isotropic configuration and $S=1$ is for a perfect anisotropic arrangement.

2.3 Results and Discussion

2.3.1 Coating thickness control

Parameters such as micro-gravure speed, substrate speed, speed ratio, capillary number, and CNC concentration collectively control the liquid transfer rate of this fabrication process. A thick liquid layer is the first requirement for maximum liquid transfer from the gravure to the substrate. The liquid thickness solely depends on a stable and continuous liquid bridge formation between the gravure and substrate. However, stretching and shear forces also exist in this liquid bridge which can destabilize it; these forces can be controlled by gravure roller and web speeds⁵⁶. A table of the coating thickness dependence on experimental parameters is presented in the APPENDIX A for each CNC concentration examined.

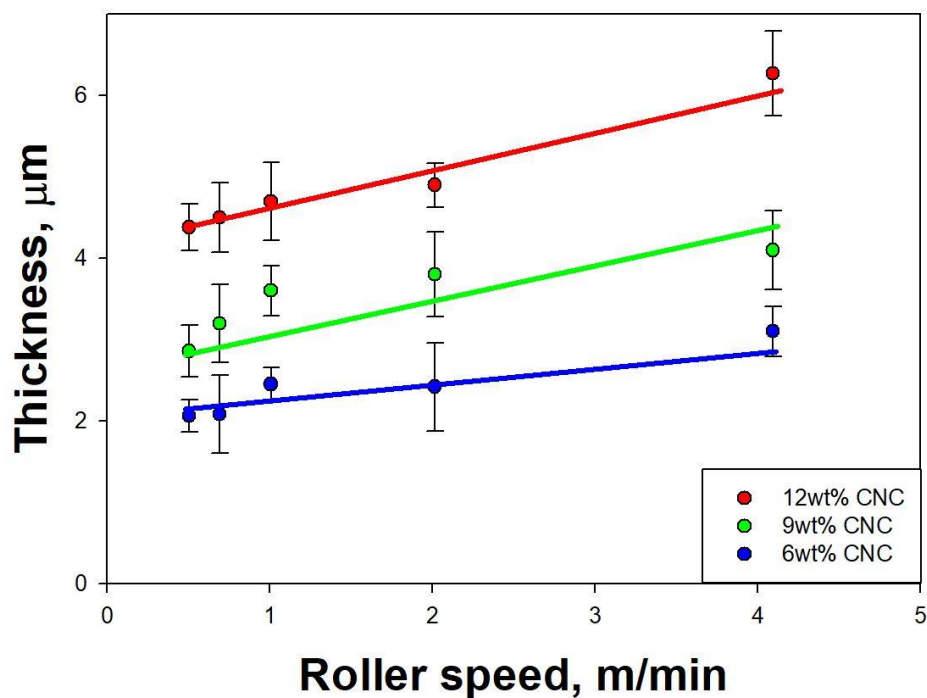


Figure 2.1 The effect of roller speed for a constant web speed (1m/min) [line added to aid the eye].

At a constant web speed, coating thickness increases with increasing roller speed and increasing CNC concentration, as shown in Figure 2.1. By doubling the CNC concentration from 6wt% to 12wt% the coating thickness approximately doubled for roller speeds less than 4m/min. Similarly, the 9wt% is approximately 1.5 times greater than the 6wt% coatings. For these conditions, solid loading of the CNC nanoparticles in the ink (i.e. concentration) primarily controls coating thickness. However, the viscosity, and therefore capillary number, which increases monotonically with viscosity, are also expected to contribute to coating thickness as these parameters should theoretically improve the liquid transfer rate⁵⁷⁻⁵⁹. At higher roller speeds, the capillary number for 12wt% is 12 times higher than 6wt% CNC suspensions, and coating thicknesses greater than twice the 6wt% coatings were achieved. At the higher roller speeds, the increase in thickness may be owing to the significant increase in capillary number and hence better

liquid transfer rate from the roller to the substrate. While the 9wt% concentration followed a similar liquid transfer behavior to the 12wt% CNC suspension, the 6wt% CNC displayed the lowest capillary numbers for this system; hence, the liquid ink exhibits Newtonian behavior and follows a symmetrical liquid bridge breakup⁶⁰⁻⁶¹. Consequently, a Newtonian liquid cannot de-wet completely from the gravure cell cavity resulting in low ink transfer and therefore, low coating thickness.

On the other hand, constant roller rotation with a variable web speed demonstrates the opposite behavior due to the reduced liquid transfer rate (Figure 2.2). At a low web speed, the roller can rotate more than one time over the web surface resulting in the maximum coating thickness at low web speeds. However, liquid transfer rate reduces gradually with increasing web speed, therefore lowering the coating thickness. In general, the direction of the stretching force should be along the web direction, and the inertia force of the liquid will be along the roller direction. Both are altered by changing the web speed. At higher web speed, the inertia force dominates the stretching force, which facilitates a lower liquid transfer rate to the web surface. For variable web speed, increasing concentration from 6wt% to 9wt% and 12wt% did not produce coatings with respective thickness 1.5 to 2 times greater, therefore, viscous and inertia forces played a role in liquid deposition. However, these effects are still small relative to solids loading.

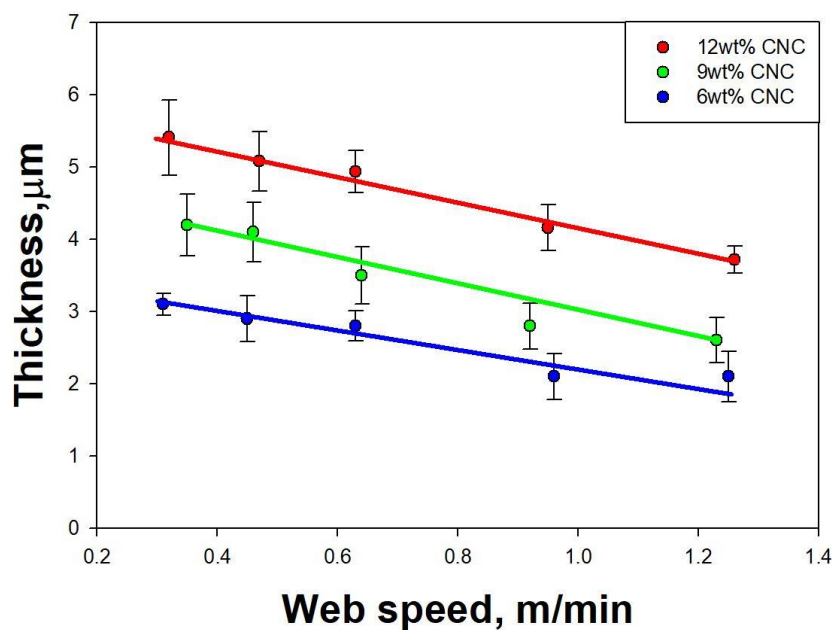


Figure 2.2 The effect of roller speed for a constant web speed (1m/min) [line added to aid the eye].

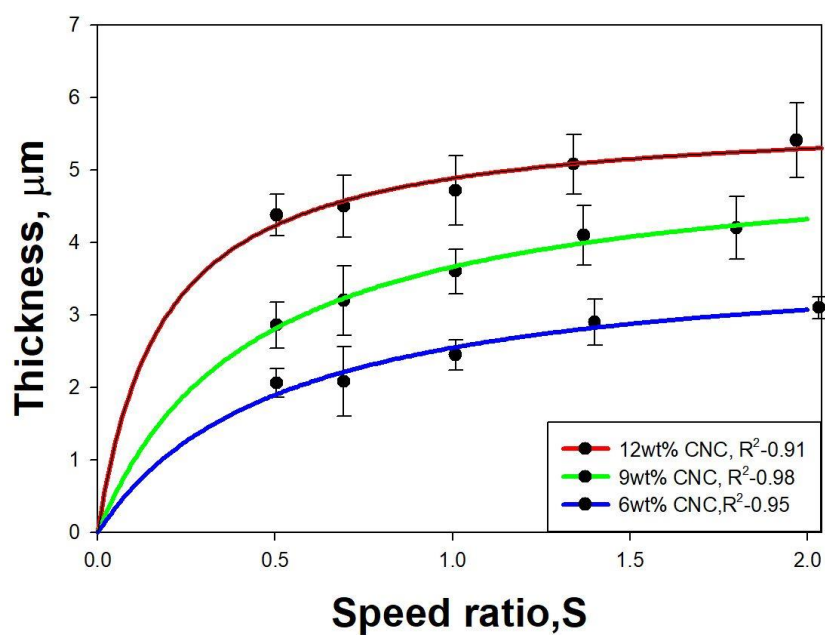


Figure 2.3 The effect of speed ratio on the coating thickness for three CNC suspensions [Nonlinear regression based on 2 parameter rectangular hyperbola].

The speed ratio is a critical parameter dependent upon on the roller and substrate speeds, where the capillary number of the liquid suspension controls the liquid transfer rate for the fabrication process. The thickness of the resultant films, and therefore liquid transfer rate from the ink bath to the substrate, increased by a small amount with increasing speed ratio for all CNC concentrations as shown in Figure 2.3. Per Hewson et al., the data was fit to a 2-parameter rectangular hyperbola^{60, 62-63}. The liquid transfer rate also depends on the viscous force and inertia force where viscous forces must dominate the inertia force to increase the coating thickness. At a lower speed ratio (0-0.5), the viscosity of the 12wt% CNC suspension is very high compared to the other concentrations. So, liquid transfer rate must be higher for the 12wt% suspension based on capillary number alone. Similarly, 9wt% has a higher viscous force compared to the 6wt% suspension and resulted in a higher transfer rate and overall higher coating thickness than the lowest concentration. Due to the extremely shear thinning nature of CNC dispersions, increasing shear rate (governed by increasing gravure rotation) will reduce ink viscosity significantly (Figure 2.4), which will reduce the liquid transfer rate at the higher speed ratio region. At this reduced viscosity, all CNC concentrations behave as Newtonian fluids in which symmetrical liquid bridge formation is the liquid transfer mechanism. Moreover, in the high-speed ratio region, the capillary number is also reduced because of the reduction in suspension viscosity at high shear rates, see Figure 2.4. The reduction of the capillary number and symmetrical liquid bridge formation are the primary reasons for steady state liquid transfer at high speed ratios where the sample thickness begins to asymptote for all suspensions (Figure 2.3).

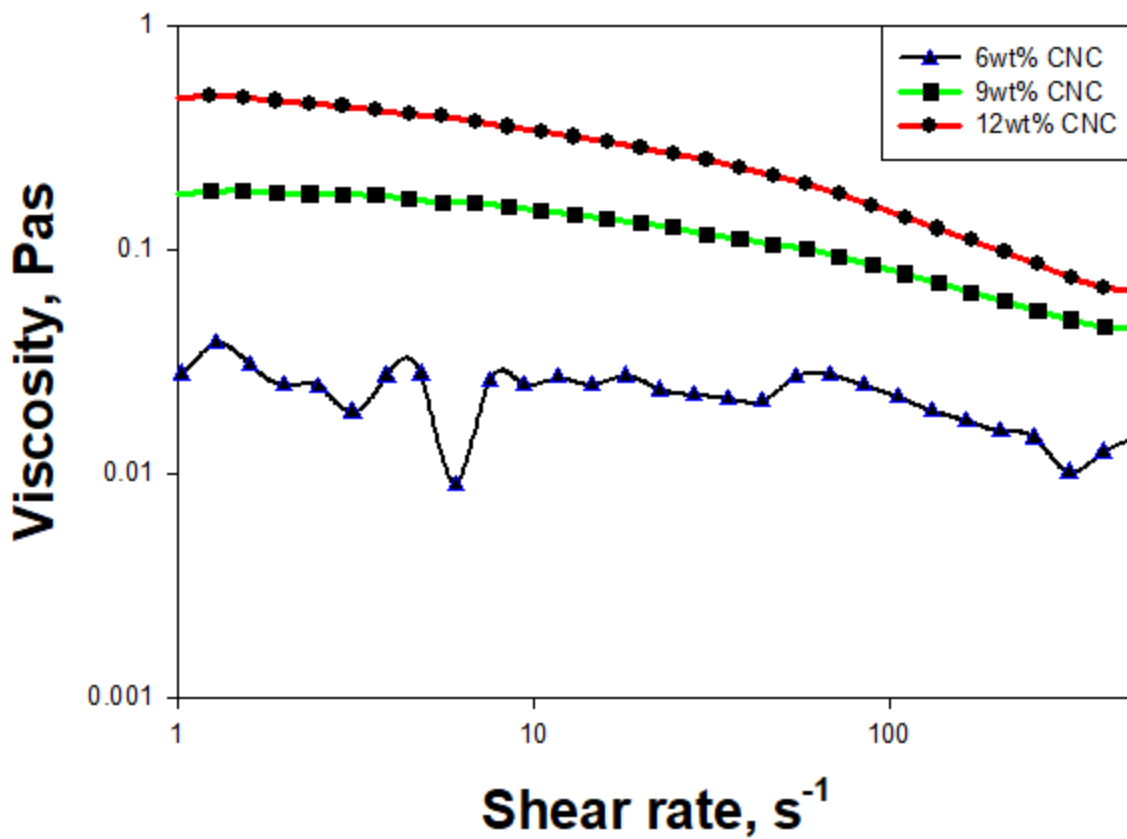


Figure 2.4 Rheological properties of 12wt%, 9wt% and 6wt% CNC suspensions.

We developed 3D mesh plots with corresponding contour plots for coating thickness as a function of web speed and gravure rotation. The highest concentration suspension shows a wider region of coating thickness with increased gravure rotation compared to the 6wt% and 9wt% counterparts in Figure 2.5. Speed ratios from 2 to 3.2 show a highly defected coating and so are of limited utility (see APPENDIX A, Figure AS2). However, defect-free coatings with reduced thickness were observed at lower speed ratios and higher web speeds. The 9wt% CNC suspension shows a much smaller region for the thickest coatings with slow gravure rotation. It appears that the maximum liquid transfer rate can be attributed to higher viscosity ink systems. We did not identify any significant effect on coating thickness for 6wt% CNC suspension which may be a consequence of the solution exhibiting a very low capillary number and Newtonian like liquid

properties. Moreover, Newtonian-like liquids exhibit symmetrical liquid bridge breakup, where the symmetrical liquid bridge breakup is always independent of viscosity, roller, and web speed effects, resulting in a constant liquid transfer from the roller to the web surface⁵⁶.

A balance between CNC concentration, roller speed, and web speed was obtained to achieve defect free coatings. Higher CNC concentrations are desirable as larger thicknesses are readily produced and shear induced anisotropy (which will be discuss later) is preserved as CNCs at high concentrations are less mobile. However, high concentration can prohibit entrapped air from escaping the solution and prevent the relaxation of the solution, which can manifest as defects in the dried coating. Likewise, fast roller speeds and slow web speeds result in multiple rotations of the roller across the substrate surface and produces a thicker coating. Although increasing web speed may be desirable for increasing production rate, at very high web speeds non-uniform coatings are produced with pinhole defects (see APPENDIX A, Figure AS2). At higher speed ratios where the web speed is less than roller speed, defects induced were de-wetting of the suspension due to bubble formation and line defects attribute to the Marangoni effect (see APPENDIX A, Figure AS2).

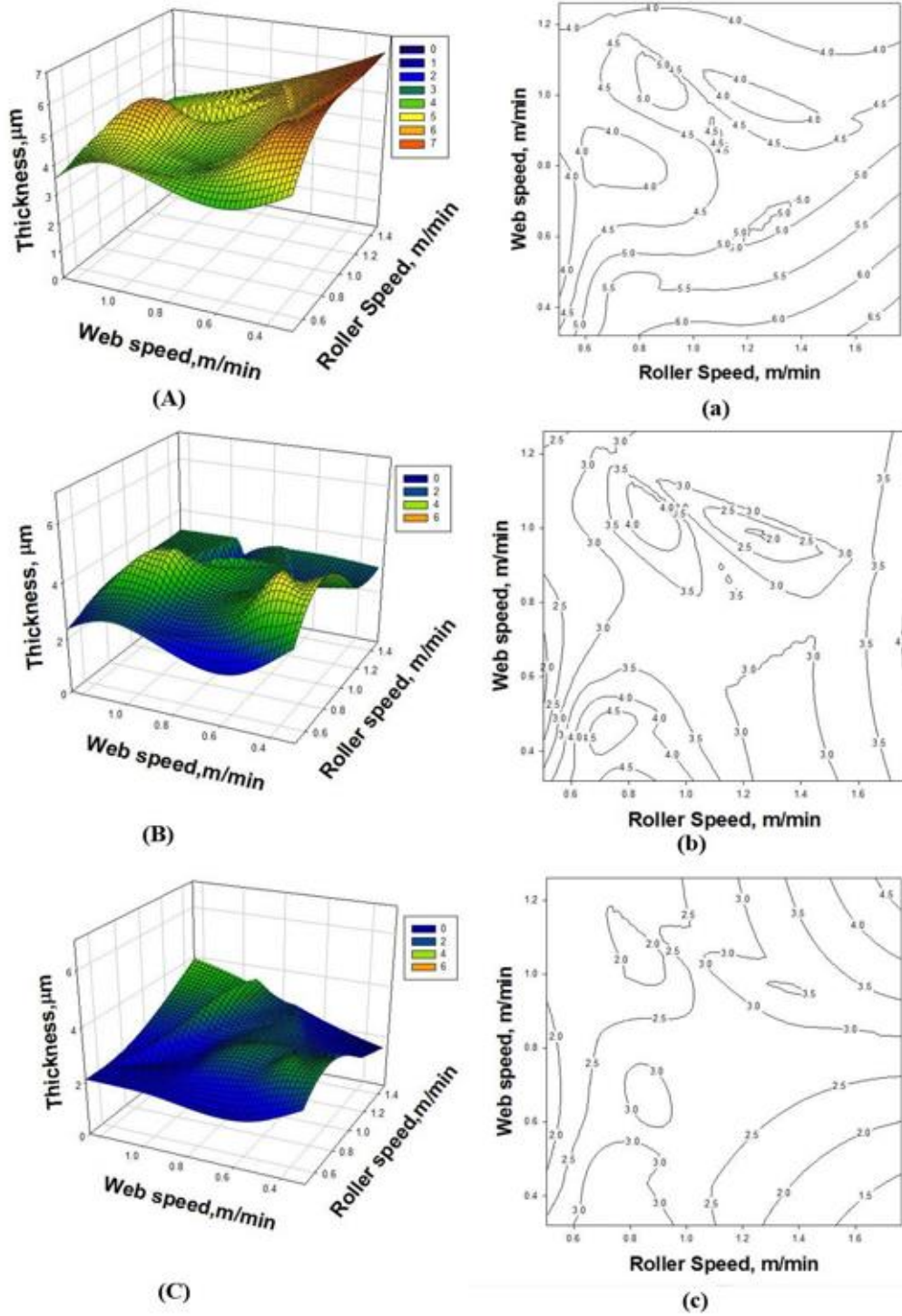


Figure 2.5 3D mesh plot with corresponding contour plot for 12wt% (A-a), 9wt% (B-b), and 6wt% (C-c) CNC coating.

2.3.2 Effect of film thickness on coating adhesion

Samples of various coating thicknesses were subjected to crosshatch adhesion tests to measure coating adhesion. Adhesive bonding within the coating and at the coating-substrate interface varies with the coating thickness. Since visual inspection of de-bonding on transparent coated PET film was challenging; polarized light was used to quantify the adhesion loss of CNC coatings. Samples were illuminated between crossed polarizers, and the damaged area was identified based on the color contrast. The coating array before and after the crosshatch test can be seen in Figure AS4 of the APPENDIX A.

CNC coatings exhibit high peel strength from the PET substrate. Substrate-coating interaction plays a significant role in the peeling strength and is determined by the surface energy and surface tension of the substrate and ink (CNC dispersion in water), respectively. Hence, a highly wettable coating shows very strong adhesion⁶⁴. Corona or plasma treated PET substrates, which have a higher surface energy and therefore are more wettable, show much higher adhesive strength compared to untreated PET substrates⁶⁵. A similar behavior was also observed for the crosshatch experiments here since a corona treatment was applied to the PET substrate.

Coating adhesion displays a strong dependence on coating thickness despite lowering the surface energy difference at the interface through surface treatment. The total coating thickness from 6wt% CNC suspension was between 2-3 μm , and no delamination was observed for this coating thickness range (Figure 2.6). Increasing the CNC concentration to 9wt% CNC suspension increases the final coating thickness to 3.5-4.5 μm and coincides with the onset of delamination in the adhesion test of coated films and therefore a decrease in coating performance. Furthermore, CNC coatings produced with the 12wt% CNC suspension (4.5-6 μm total thickness) demonstrate the lowest adhesive rating compared to 6wt% and 9wt% suspension. Conceivably a variety of factors could be leading to the higher adhesion of thinner layers. However, it is observed that the

coating adhesive strength on PET substrate is independent of the initial ink concentration. To test this observation, a 2-3 μm thick CNC coating from 12wt% CNC suspension was prepared with a R180 microgravure, and a crosshatch adhesion test was performed. No significant delamination was observed which confirm that adhesion is independent of initial CNC concentration.

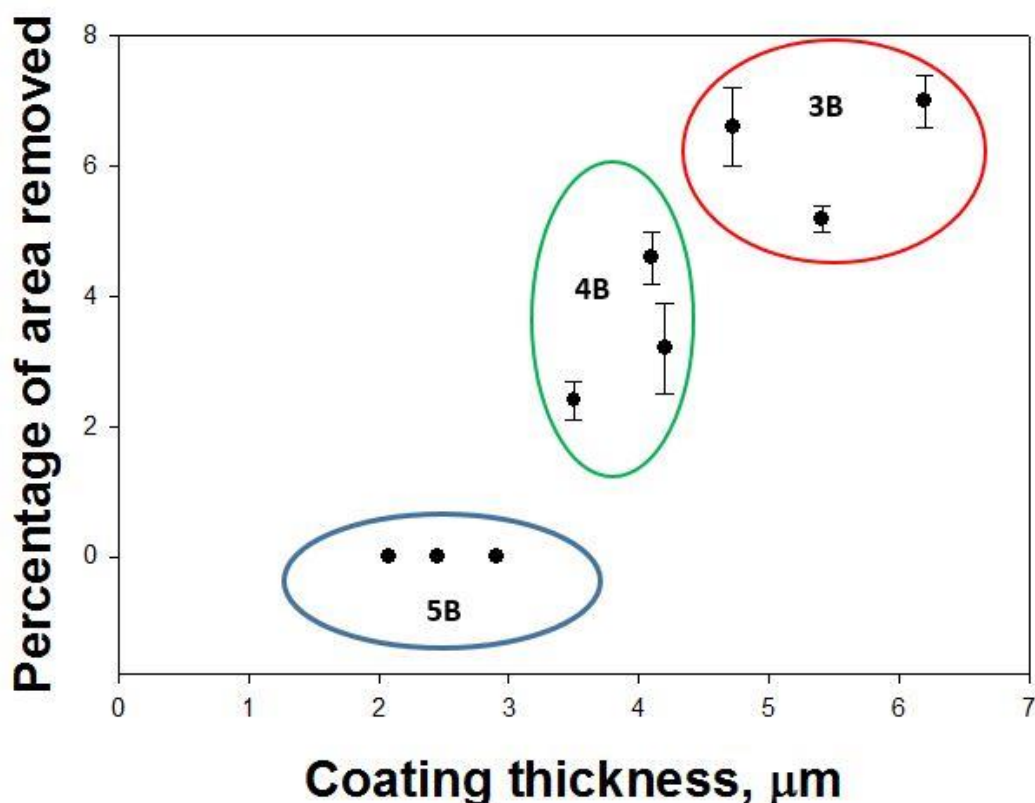


Figure 2.6 Crosshatch peel adhesion strength of 12wt%, 9wt% and 6wt% at varying coating thickness.

The cohesive strength of the bulk CNC coating, and the adhesive strength between the substrate-coating interfaces can explain the above observation. As a rule of thumb, a reduced coating thickness can improve coating adhesion⁶⁶. As the final coating thickness depends on the initial CNC concentration, the thinnest coatings produced by the 6wt% suspension possessed the maximum peel strength (Figure 2.6). Theoretically, the cohesive strength should not change

significantly for any thickness difference; moreover, the adhesive strength at the interface is independent of the coating thickness. We expected the adhesive rating to be similar for all CNC concentrations, but we observed delamination for 9wt% and 12wt% CNC suspension-based coating. Fabrication defects present on the surface and in bulk coating regions, which strongly depend on film thickness, may initiate cracks in the coating that result in delamination. As well, there may be residual stress in the films owing to their rapid drying and low solids gel point⁵.

The mechanism of defect formation in roll-to-roll system strongly depends on the viscosity and capillary number of the ink system. Here, high viscosity liquids (9wt % and 12wt%) will have higher capillary numbers. Higher capillary number fluids can entrap air bubbles on the gravure, which can lead to different coating defects (see Figure AS2 in the APPENDIX A). Moreover, high-speed gravure rotation of a viscous ink system can also produce air bubbles in the ink bath which in turn may produce defects in thicker coating samples not present in thinner coatings. The presence of a volume defect like cavitation can reduce the adhesive bond between the interfaces and therefore reduce the adhesive strength which results in delamination or de-bonding at higher coating thicknesses.

2.3.3 Effect of CNC concentration on surface morphology and optical transparency

Surface morphology varied greatly with CNC concentration. As CNC concentration was increased, the surface roughness was seen to increase, see Figure 2.7. Both the 9wt% and 12wt% surface morphologies were considerably rougher compared to the 6wt% suspension, which is reflected in R_q , the root mean squared height deviation, of Table 2.1. The presence of groove or current-like morphologies in the 9wt% indicate a strong directional dependence of the surface morphology. The direction of the grooves approximately coincides with the 0-20° orientation introduced by the gravure tilt along the direction of shear. For highly viscous suspensions like the

9wt% and 12wt% the relaxation time is longer and so solutions will retain more orientation during processing, as seen with the order parameter in the subsequent section, in the rolling direction. The scale and frequency of this morphology are both too small to be gravure patterning. The unique appearance may be a result of local de-wetting of the suspension from the surface similar to microscale defects seen at higher speed ratios. While the 12wt% is still rough, it did not exhibit a strong direction dependence did in the areas examined. It did have several pockets, which may be the result of cavitation. Cavitation can occur when air becomes entrapped in a viscous solution and is transferred to the surface. The 6wt% exhibited small variation in sample roughness, see Table 2.1. This is not surprising as the suspension behaved as a Newtonian fluid and has a fast relaxation time compared to the 9wt% and 12wt%. In particular, the maximum vertical height difference, R_{\max} , and R_q were proximately twice as large for the 9wt% and 12wt% CNC coatings compared to the 6wt%. Increased surface roughness creates a stronger adhesive bond between the coating and the tape in the peel test by strengthening the mechanical bond between the surface and tape. Increased surface roughness can be problematic as defects and uneven surfaces are sites for failure. The increased roughness of the higher suspensions may be one reason the 9wt% and 12wt% adhesion performance was so low compared to the 6wt%.

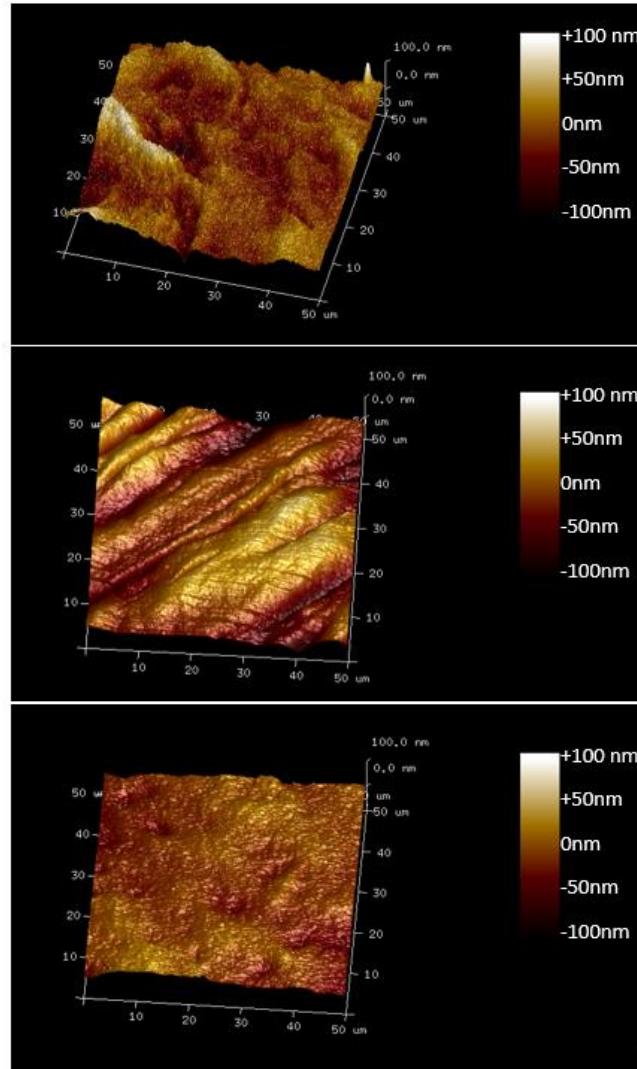


Figure 2.7 Surface morphologies of coatings from suspensions of A) 12 wt% CNC, B) 9wt%, and C) 6wt%.

Table 2-1 Roughness measurements as a function of CNC content.

CNC Content (wt%)	R_q (nm)	R_{max} (nm)
12	14.4 +/- 1.08	126 +/- 28.47
9	18.11 +/- 3.58	139 +/- 20.00
6	6.39 +/- 0.77	65.27 +/- 7.52

R_q : Root mean squared deviation in height.

R_{max} = Maximum vertical height difference.

Surface morphology is indicative of the liquid transfer efficiency as well. A liquid bridge exists between the gravure and the substrate in which ink is transferred. Across this liquid bridge there can be a surface tension gradient which will help drive liquid transfer. If the surface tension of the liquid is minimized by wetting the substrate, it will do so. A reasonable expectation is that the surface morphology would be smooth and flat if surface tension favors the transfer of the ink to the substrate. However, viscous forces will be competing against surface tension. As the viscosity of the liquid increases the capillary number increases. For high viscosity, high Ca, the viscous forces will dominate surface tension effects in flow behavior and the surface may still appear rough despite liquid transfer being a favorable process. In the present study, the capillary number is increasing with increasing CNC concentration which may explain why surface roughness is increasing significantly despite favorable wetting conditions after corona treatment and layer-by-layer coating.

Exceptional optical transparency was obtained for CNC coated PET films (see Figure 2.8). Flexible PET demonstrated 89-92% transparency for a wavelength range from 400-750nm, while CNC coating transparency degraded only 2% compared to the bare substrate (Figure 2.9). This reduction may be due to the differing refractive index of the CNC coatings or due to the higher surface roughness of the coatings compared to the substrate. Of the CNC coatings, the 12wt% transparency was 1.5% lower than the 6wt% and 9wt%. The presence of defects (due to a higher capillary number and gravure rotation) or higher surface roughness in 12wt% CNC coating may be responsible for the slight decrease. The diffuse reflection of incident light is promoted by surface roughness and may cause light scattering, reducing the ultimate transparency of the 12wt% film. Moreover, edges of defects can cause diffraction of the incident light and therefore also;

reduction of transparency. Regardless, all transparency loss of the coatings is small and not noticeable by the naked eye.



Figure 2.8 Photographs of CNC coatings on PET substrate (15cmX15cm): (top left) PET substrate, (top right) 12wt% CNC solution, (bottom left) 9wt%, (bottom right) 6wt%.

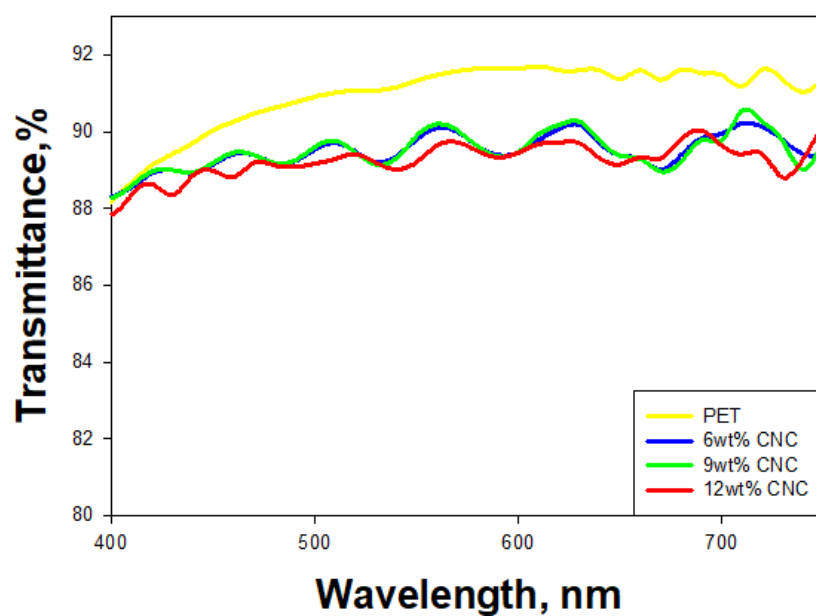


Figure 2.9 Optical transparency for different CNC coated PET films.

2.3.4 Gravure rotational effect on anisotropy (nematic configuration)

The liquid crystal domain arrangement (anisotropy, in this case) is largely determined by the combined action of the shear rate and domain retention time, which depends on the gravure rotation and the rheology of the CNC solution. To calculate Herman's order parameter, S , light transmittance of free-standing CNC films was measured. Films were created by varying gravure rotation (which determines shear rate) and CNC concentration at 6wt%, 9wt%, and 12wt%. A minimum of four layers were used to achieve coatings of 16-20 μ m in thickness which could be delaminated from the PET substrate for light transmittance measurements. The maximum transmitted light intensity increases with increasing CNC ink concentration for the 45° configuration while the 90° configuration is generally decreasing (see appendix-a, Table AS4). D , calculated as the ratio of the maximum transmitted intensity between the 45° and 90° configurations, increases from 1.79 for the 6wt% up to 4 for the 12wt% and fixed shear rate. This suggests that preferential alignment of the crystalline domains along the shear direction is improved by increasing CNC concentration. D is maximized for the 12wt% samples which implies that the difference in refractive index for longitudinal and transverse directions is also highest for the 12wt% compared to the other concentrations (see APPENDIX A, Table AS4).

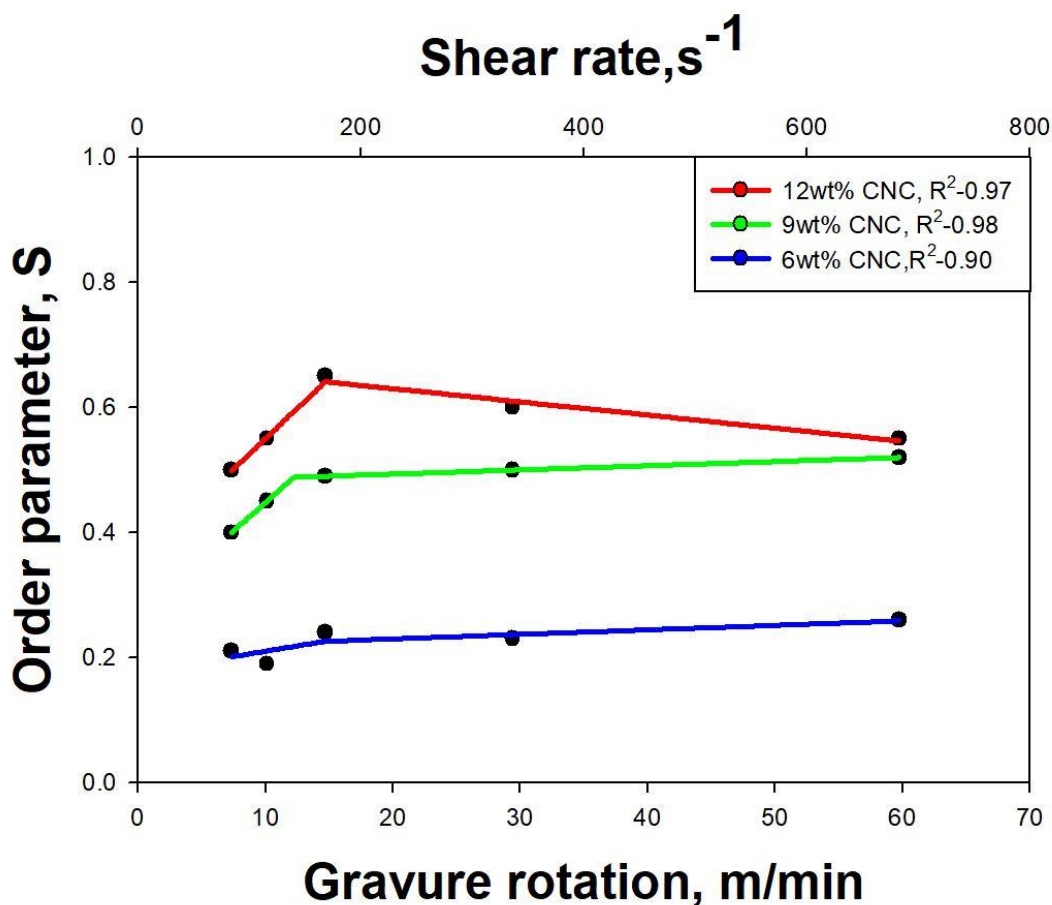


Figure 2.10 Order parameter variation with roller speed (substrate speed= 1m/min) [Nonlinear regression based on a piecewise linear approximation].

An increasing order parameter as a function of gravure rotation/shear rate (Figure 2.10) is observed and likely due to shear-induced alignment of the CNCs during the gravure process. At a low shear rate of 80 s^{-1} , 12wt% films show an order parameter of ~ 0.5 . As anticipated, an increase in shear rate enhances domain alignment along the shear direction, but only by a modest amount. A maximum order parameter of 0.65 is achieved at 170 s^{-1} shear rate for the 12wt%. However, a negligible reduction in the anisotropy of the CNC coating is observed at the higher gravure rotation, and the order parameter is almost constant at the elevated shear rate region. On the other hand, 9wt% samples show less anisotropy at any gravure rotation and increasing the shear rate had a smaller effect on the domain alignment. We did not observe any anisotropic (nematic configuration)

properties in 6wt% CNC samples. Regardless, in at all concentrations, the natural chiral nematic domain structure was sufficiently disturbed to allow for high transparency.

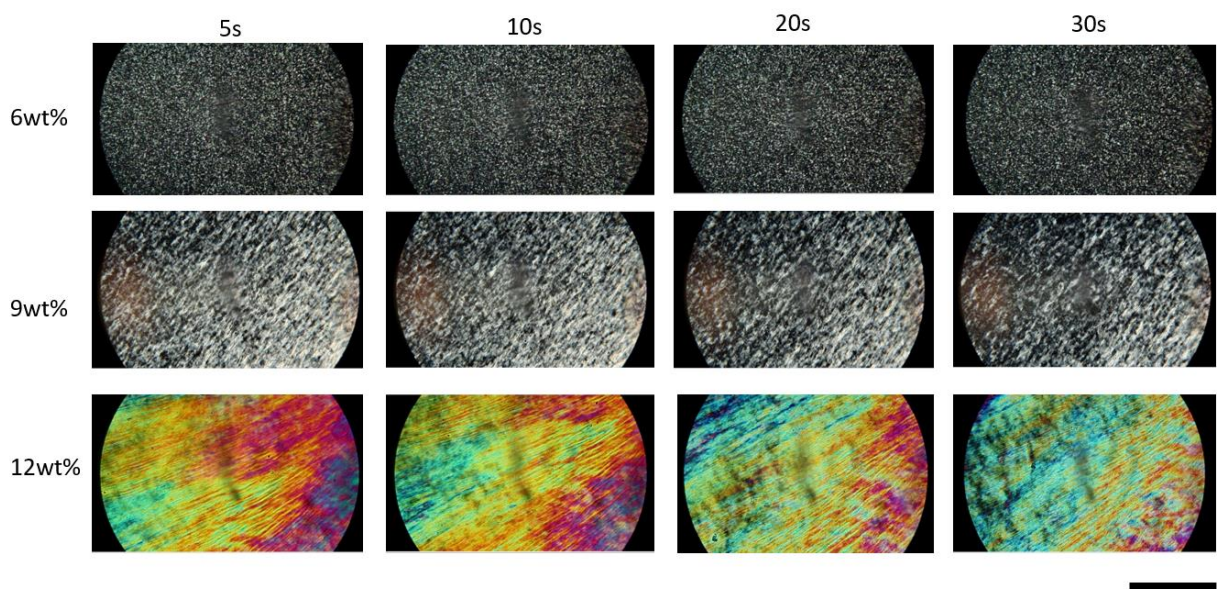


Figure 2.11 CNC particles diffusion with different CNC concentrations. Here, scale bar= 0.5mm.

The liquid crystal domain of the anisotropic CNC coating must align its crystal position along the shear direction during coating and the relaxation time for the CNC domain movement should be lengthy^{44-45, 67}. Thus, the initial CNC concentration contributes to alignment. A low concentration CNC suspension behaves like a Newtonian fluid and the domains show a fast relaxation time after applying shear. With enough time domains show a highly isotropic configuration⁶⁸. However, the Newtonian nature may also limit orientation in the first place. Figure 2.11 shows the liquid crystal domains movement of 6wt% CNC suspension along the shear direction of a doctor blade sheared specimen. Very little alignment remains after only 5 s of relaxation. At 9wt%, it can be seen in Figure 2.11 that CNC domains can be aligned along the shear direction. However, in previous work, the anisotropy was completely destroyed after 5-10 mins⁴³, despite having achieved 50% alignment for a 9wt% concentration. Here, we used a 1m/min

web speed where the ink bath to drying unit distance was 50cm, so the time before drying is 30 secs. Assuming a zero time to dry once it enters the oven (while not true, we do not know the time to when the films become dry, only that they are dry when they come out), then the long relaxation time as compared to the dry time would lead to a high alignment retention, so ~50% anisotropy is logical considering the previous work getting similar results with simple shear. Similarly, the alignment of the 12wt% CNC suspension has a relaxation time of 30 mins⁴³, but again, is locked into place in 30s so the even higher order parameter ($S=0.65$) is expected as Figure 2.11 shows very little disorientation over this time scale.

Based on previous work, the 12wt% concentration should have a higher order parameter for shear rates higher than 100s^{-1} . However, the micro-gravure surface morphology may be responsible for this effect. A standard micro-gravure with a 20° tilt angle was used for this fabrication. The shear direction was not 0° along the shear direction; hence, the CNC dispersion experiences a complex shear state and it could be expected that the CNCs should be oriented somewhere between 0 - 20° , therefore reducing the overall order parameter. An unconventional design like the 0° tilt angle micro-gravure may improve the alignment of the CNC suspension-based coating.

2.4 Summary

The effect of various parameters on CNC coatings for three aqueous suspensions has been described for R2R production. The effect of gravure rotation, substrate speed, and viscosity significantly control the liquid transfer mechanism from the ink bath to the flexible substrate, where the maximum coating thickness was observed at higher speed ratios for all CNC concentrations. Moreover, parameter optimization was crucial for ink transfer at the 12wt% CNC

concentration, while reduction in CNC concentration significantly reduced the necessity of parameter optimization to produce coatings.

It was noticed that the coating adhesion strength was inversely related with coating thickness. Maximum coating strength was observed for the low concentration ink system as maximum cohesive strength is attributed to a thinner coating which exhibited the lowest level of surface roughness. High concentration, high viscosity solutions exhibited qualitatively rougher surfaces which may adversely affect adhesion strength by creating weaker sites across the surface at which cracks may more easily develop.

Liquid crystal domain arrangement, quantified as the order parameter, was measured as a function of gravure rotation for various CNC concentrations. The 12wt% CNC concentration inks retain the highest level of alignment along the gravure rotation direction, resulting in an anisotropic (nematic) coating and maximum order parameter of 0.65. However, at smaller CNC concentrations, CNC domain alignment is reduced as ink fluidity enables rapid relaxation of the aligned crystal domains. Moreover, the presence of a tilt angle (20°) in the tri-helical micro-gravure is another significant reason for crystalline domain deviation from the shear direction, which reduced the overall order parameter for CNC coating.

CHAPTER 3. ROLL-TO-ROLL FABRICATION OF CELLULOSE NANOCRYSTAL-POLY(VINYL ALCOHOL) COMPOSITE COATINGS WITH CONTROLLED ANISOTROPY

All lab work except surface morphology (SEM, and Optical Profilometry) was performed by Reaz Chowdhury. All analysis except surface roughness was performed by Reaz Chowdhury with guidance by Prof. Jeffrey P. Youngblood. All writing was performed by Reaz Chowdhury with guidance and editing by Prof. Jeffrey P. Youngblood.

The following chapter contains content reproduced with permission from R. A. Chowdhury, C. Clarkson, V. A. Apalangya, S. N. Islam, and J. P. Youngblood, "Roll-to-roll fabrication of cellulose nanocrystal-poly (vinyl alcohol) composite coatings with controlled anisotropy," *Cellulose*, vol. 25, no. 11, pp. 6547-6560, 2018. Copyright 2018 Springer Science + Business Media

3.1 Introduction

Functional polymer coatings are found across many sectors from electronics to food packaging industries where these coatings can serve a variety of purposes, i.e. as thermal insulators, dielectrics, or as barrier materials, just to name a few. For instance, in food packaging polymer coatings are primarily used as barrier materials to reduce the rate of water and oxygen permeation (the culprits behind food spoilage and subsequent waste). Nanocellulose, a class of nanomaterials derived from natural resources containing cellulose, is being investigated in functional coatings for its ability to simultaneously improve performance in many of these areas⁶⁹⁻⁷⁰ and more^{33, 71-72}. Nanocellulose is a desirable coating material as it is abundant, renewable, and has a low environmental impact (cellulose is nontoxic, and biodegradable)⁵.

Cellulose nanocrystals (CNCs) and cellulose nanofibrils (CNFs) are the two most common types of nanocellulose in coatings. Cellulose nanocrystals (CNCs) are rod shaped, anisotropic nanoparticles of 3-5 nm wide and 20-50 nm which exhibit a unique set of properties such as high stiffness (Young's modulus 100–140 GPa)³³, high strength⁵, high thermal conductivity²⁵, low coefficient of thermal expansion³⁹, and excellent optical properties⁷³. CNFs are a larger aspect

ratio nanoparticle (4-20 nm and 0.5-2 μm) which have fibrillar structure. CNCs exhibit liquid crystalline behavior in aqueous media while CNFs do not, and the crystalline domain configuration can be altered with CNC concentration⁷⁴. Dilute solutions are typically isotropic, while at higher concentration under an external force (such as magnetic field, electric field or mechanical force), non-flocculating liquid crystalline domains can turn to align as a cluster of domains which can form anisotropic (nematic) structures^{25, 34, 75}. The presence of anisotropic crystalline domains has been reported to improve the mechanical, thermal and barrier properties (such as selective gas barrier or water vapor resistance) of coated films which is useful in packaging and other composite applications^{5, 76-78}. Although both CNCs and CNFs have been shown to improve barrier performance, CNFs have a higher viscosity at lower concentrations due to entanglements and larger particle size⁷⁹. High viscosity and high yield stress are particularly challenging for high-speed coating processes^{71, 79}. CNCs, which exhibit shear thinning behavior at high shear rates, can be used in higher concentrations to produce thicker coatings, however, control over anisotropic domains is essential for maximizing performance.

Large area bulk materials with anisotropic orientation of CNC domains is very difficult to achieve. Current fabrication techniques proposed are laborious and complex; these include several post-processing treatments to realign the crystalline domains in the bulk materials. For instance, Tan et. al. employed a series of stretching, heating and refrigeration treatments to mechanically realign the crystalline domains of shear casted films⁸⁰. Although this method produced well aligned crystalline domains resulting in improved mechanical, optical and hygroscopic strain performance⁴¹⁻⁴², the potential cost of a complex, multi-step process reduces its attractiveness for a large-scale production. Generally, high viscosity solutions are required for shear casting and it is extremely difficult to obtain uniform film thickness. Moreover, the realignment of liquid

crystalline domains also adversely degrades the anisotropic behavior. Spin coating of cellulose nanomaterials can significantly improve the coating quality with controlled thickness⁴⁶. However, only segmental anisotropy can be achieved with this method instead of overall alignment in the coating. Moreover, this method is only suitable for small area production.

Roll-to-roll (R2R) is a versatile and large-scale manufacturing technique for flexible coating/printing, which is applicable in various fields such as agriculture, semiconductors, medicine and packaging¹⁹. The R2R manufacturing process can be coupled with slot-die, gravure, spray, inkjet, nano-imprinting, or a rotary screen that makes it an indispensable tool for the large-scale manufacturing of flexible coatings, polymer solar cells, and flexible electronic devices, etc.^{19, 81}. Limited progress has been made for in R2R of cellulose nanomaterials. Most of the reported work was based on CNF and CNF nanocomposite coatings produced with a slot die system^{53, 82}. Most recently, Chowdhury et. al successfully used roll-to-roll microgravure to manufacture large area CNC coatings with excellent control of anisotropy⁶⁹. R2R production of CNC coatings are limited, but of key interest as these processes can be employed to control anisotropy which CNC coating performance strongly depends on. Additionally, R2R production of CNC nanocomposite coatings are absent in the literature despite the potential improvements to coating performance, such as flexibility, adhesion, and coating/substrate compatibility, with the addition of polymer.

Poly(vinyl alcohol) (PVA) is a nontoxic, semi-crystalline, and water-soluble polymer commonly used in food packaging as a barrier film⁸³. Due to strong hydrogen bonding, PVA and CNCs can produce completely miscible polymeric nanocomposites; making it an excellent candidate for fiber, aerogel or film production⁸⁴⁻⁸⁶. PVA reduces the brittleness of CNC films and CNC can significantly improve the mechanical properties (such as Young's modulus) and

crystallinity of PVA^{84, 87}. Inherent chemical compatibility, mutual affinity for water, and established industrial use makes PVA a natural candidate for CNC nanocomposite coatings.

With controlled anisotropy, CNC coatings exhibit good mechanical, thermal, and barrier properties which are attractive in many applications. CNC nanocomposite coatings may facilitate alignment of crystalline domains while providing additional benefits to the coating system. The present study investigates the use of a roll-to-roll reverse gravure process for controlled anisotropy in PVA/CNC nanocomposite coatings which is independent of polymer substrate type. The emphasis of this study is on the large-scale fabrication of PVA/CNC nanocomposite coatings for weight ratios where PVA is the primary phase to CNCs as the primary phase to determine the effect of PVA on CNC orientation. CNC orientation (random vs. anisotropic) was correlated with solution viscosity, which is strongly related with CNC-PVA solids loading ratio. PVA/CNC coatings were characterized with polarized light microscopy, UV-Vis spectrophotometry, cross-hatch adhesion testing and optical profilometry. Water vapor transmission rate (WVTR) was evaluated as it is of key interest in potential applications for this material.

3.2 Experimental section

3.2.1 Materials and Methods

Sudan Blue dye II and poly(vinyl alcohol) 89-98K with 98% hydrolysis were purchased from Sigma Aldrich. Never dried, pristine CNC (12.2 wt% batch no-2015-FPL-71 CNC) aqueous suspension that contains 1% sulphur and a sodium counter ion, was purchased from University of Maine and manufactured by the USDA-US Forest Service-Forest Products Laboratory (FPL) (Madison, WI, USA). All materials were used as active ink ingredients without any purification. A stock solution of 12wt% PVA suspension was prepared by adding 36 g of PVA in 300 g water and heated for 3hrs at 120°C. Stock solution of CNC (12% in water) was added to the PVA solution at

a fixed concentration to produce the final compositions. The final compositions of different CNC-PVA coating ratios are shown in the Table 3-1. Before fabrication, all ink suspensions were ultrasonicated (Branson Ultrasonics, Danbury, CT, USA) for 3 mins (at 50% amplitude with a 1 s plus and 1 s rest at 60 Hz frequency) to disperse CNCs and homogenize solution. Flexible PET, MELINEX® 462 2 mil (TEKRA) and PLA films (Cargill Dow LLC) were used as substrates for the coating process.

Rheological measurements for CNC-PVA suspensions were performed with a Malvern Bohlin Gemini HR Nano rheometer. A cup and bob fixture with 100 μm gap distance was used for each experiment. All measurements were performed with a variable shear rate (0.1 – 500/s) at room temperature. The setting of shear rate measurement for different coating formulations can be found in the APPENDIX B.

3.2.2 Surface tension measurements

Surface tension measurements were obtained at the ink/air interface by pendant drop tensiometry. A Ramé-Hart contact angle goniometer with DROPImage Advanced software (Model 500) was used for this characterization. The geometrical profile of the static pendant drop was compared with the theoretical (Laplace equation) drop profile. All measurements for various ink compositions were performed at room temperature and humidity.

Surface energy of the substrate was measured based on the ASTM D2578 standard test method. Fluids with increasing surface tension was applied on the substrate until a wetted film surface was observed. The corresponding surface tension of the fluid is equal to the surface energy of the substrate. For this experiment, dyne pens were purchased from Accu Dyne Test™ with different standard test marker (40, 42, 44,, 68,70 dynes/cm). The uncertainty of the measurement is between 1-2 dynes/cm.

3.2.3 Coating equipment

A Mirwec Mini-Labo DeluxTM system with a trihelical (mesh R30 and mesh R90 with 5.5-inch length) microgravure system was utilized for coating fabrication. Micro-gravure properties such as diameter, cell volume and cell depth information can be found in the APPENDIX B. Gravure roller, ink batch, doctor blade, flexible substrate and a hot air-drying chamber (about 1m length) are the major components for this instrument (Figure BS1 in the APPENDIX B). The gravure roller was placed with an ink bath that continuously transferred ink from an ink bath to the substrate. A doctor blade with 50 μm gap distance was placed over the gravure roller which continuously removed excess ink from the gravure roller, thus producing uniform coating thickness. The fabrication process was performed at 1 m/min substrate speed with 30 rpm gravure rotation. Two temperatures were used for this fabrication based on the heat deflection temperature of the substrate. Coating on the substrates was performed at 80°C and 45°C for PET and PLA, respectively.

Both PET and PLA substrates have low surface energy compared to the surface tension of the ink system. As a result, a surface treatment of the substrate was essential to overcome de-wetting (caused by ink/substrate incompatibility). A high-power corona discharge system (QC electronics, Inc.) was used for substrate processing. A 0.5 KW power supply with 0.5 m/min substrate speed rate was sufficient to increase the substrate surface energy and enhance ink/substrate compatibility (details can be found in the APPENDIX B, Table BS3).

3.2.4 Film characterization

A conventional UV-Vis spectrophotometer (Spectramax Plus 384, Molecular devices Corp., 133 Sunnyvale, CA) was used for the transparency measurements. All measurements were performed between 350 - 750 nm wavelength ranges with air as the background. Coating thickness of the samples were observed by a scanning electron microscopy (SEM, Pro X, Phenom). Before imaging, an electrically conductive thin layer of gold coating was sputtered on the specimen.

3.2.5 Adhesion test

The adhesion of CNC/PVA coating to the PET substrate was studied with a cross-hatch adhesion test method (ASTM-D3359). Briefly, adhesive spray (Loctite multi-purpose) was used to attach a specimen on the glass plate. After complete drying, 11 parallel and 11 perpendicular cuts (each cut was 1 mm apart) were made on the samples. Then, a pressure sensitive tape (Elcometer 99) was placed over the film for 2 to 3 minutes and removed from the surface at 180° angle. The grid area investigation was difficult for the colorless coating, so a colored dye (Sudan blue II) was added to the CNC/PVA to enhance the visual inspection.

3.2.6 Surface roughness and 3D topography characterization

3D topographical characterization with surface roughness was measured with a Bruker GT-K1 optical profilometer at 50X magnification for 1 mm x 1 mm sample dimension. White light interferometry was used to capture the surface roughness of the coating surface. Vertical scanning interferometry (VSI) with tilt filter was used for each test sample that confirms the comparison of each point with its neighbors which provides a 3D image of the surface area, free of tilt influence. The advantage of using optical profilometer can be found in the APPENDIX B.

3.2.7 Anisotropy measurement

The crystalline domain alignment of the coatings was determined using a conventional UV-vis spectrophotometer where the order parameter was measured as a function of CNC domain orientation in all samples. The measurement is described elsewhere in detail³⁸. Briefly, a delaminated sample was inserted between cross polarizers and the transmitted light intensity was measured from 350 to 750 nm wavelength regions for 45° and 90° configurations. Finally, the following equations were utilized for the order parameter, S calculation.

$$I = I_0 \sin^2 2\theta \sin^2 \left(\frac{\pi \Delta n d}{\lambda} \right) \dots \dots \dots (3.1)$$

So

$$\frac{I_{45}}{I_{90}} = \frac{I_0 \sin^2 (2 \cdot 45) \sin^2 \left(\frac{\pi \Delta n d}{\lambda} \right)}{I_0 \sin^2 (2 \cdot 90) \sin^2 \left(\frac{\pi \Delta n d}{\lambda} \right)}$$

Hence,

$$\frac{I_{45}}{I_{90}} = D^* = D \cdot g = \frac{(2S + 1)}{(1 - S)} \dots \dots \dots (3.2)$$

Here, I_0 , θ , Δn , d , λ , I , and D represent the amplitude of the incident light, the angle of the material between the cross-polarizer, refractive index difference, film thickness, wavelength, transmitted light intensity, and dichroic ratio, respectively. The order parameter for all material measurement is between 0 and 1, where $S=0$ is defined as an entirely random/ isotropic configuration and $S=1$ is for a perfect anisotropic arrangement.

3.2.8 Water vapor transmittance rate

The steady-state water vapor permeability for CNC-PVA coatings on PLA was measured according to ASTM- D1653 by a conventional permeability cup (purchased from Gardco, FL). Circular 35 mm diameter samples were precisely cut with a laser cutter and used as test specimens. The permeability cup was filled with water to within a ¼ inch of the top edge and sealed; leaving a small air gap between the specimen and water. The whole arrangement was kept in a desiccator with anhydrous CaCl_2 and maintained at $23 \pm 1^\circ\text{C}$ with very low (3 ± 1) relative humidity for this experiment. The cup was weighted for three days, and the WVTR was calculated.

The WVTR was performed to investigate the effect of anisotropy for different coating systems. Only PLA WVTR experiments were performed as the WVTR of PET is already very low by comparison. This allowed experiments to be performed over several days rather than several months.

3.3 Results and discussion

3.3.1 Coating process

A continuous liquid coating with homogeneous thickness is required for any uniform gravure coating. A roll-to-roll gravure coating depends on certain parameters such as substrate speed, gravure speed, and ink viscosity that collectively control the coating thickness and its product quality. The coating parameters for different nanocomposite systems have been shown in Table BS1 of the APPENDIX B. The corresponding coating thickness for different coating formulations are shown in Table 3-1.

The surface energy compatibility between a substrate and ink system is the most important factor for any coating system. In aqueous media, the pristine CNC demonstrated higher surface tension compared to PVA solution, as shown in Figure 3.1. Both CNC and PVA contain hydroxyl groups in their chemical structure, which can hydrogen bond with water. However, PVA has been shown to reorient at surfaces to expose its hydrocarbon backbone and reduce surface energy⁸⁸. Likewise, here PVA may be expected to migrate to the surface of the liquid to lower the overall surface tension, which was observed in this work. All ink systems demonstrated significantly higher surface energy compared to both substrates (details can be found in the APPENDIX B). The surface energy difference creates incompatibility between the substrate and ink system, which prevents strong interfacial bonding and uniform coating. In order to ensure ink/substrate compatibility, both substrates were treated with a corona treater to sufficiently raise the surface energy of the substrates to match those of the ink systems.

Table 3-1 Coating formulations for different compositions

Composition	12 wt% CNC suspension, g	12wt% PVA suspension, g	Film thickness on PET, μm	Film thickness on PLA, μm
PVA	0	100	$5.8\pm.33$	$1.93\pm.09$
CNC: PVA (25:75)	25	75	$4.6\pm.47$	$1.8\pm.23$
CNC: PVA (50:50)	50	50	$4.7\pm.25$	$1.58\pm.13$
CNC: PVA (70:30)	70	30	$4.3\pm.15$	$1.57\pm.15$
CNC: PVA (90:10)	90	10	$4.2\pm.21$	$1.47\pm.15$
CNC	100	0.0	$3.8\pm.06$	$1.23\pm.09$

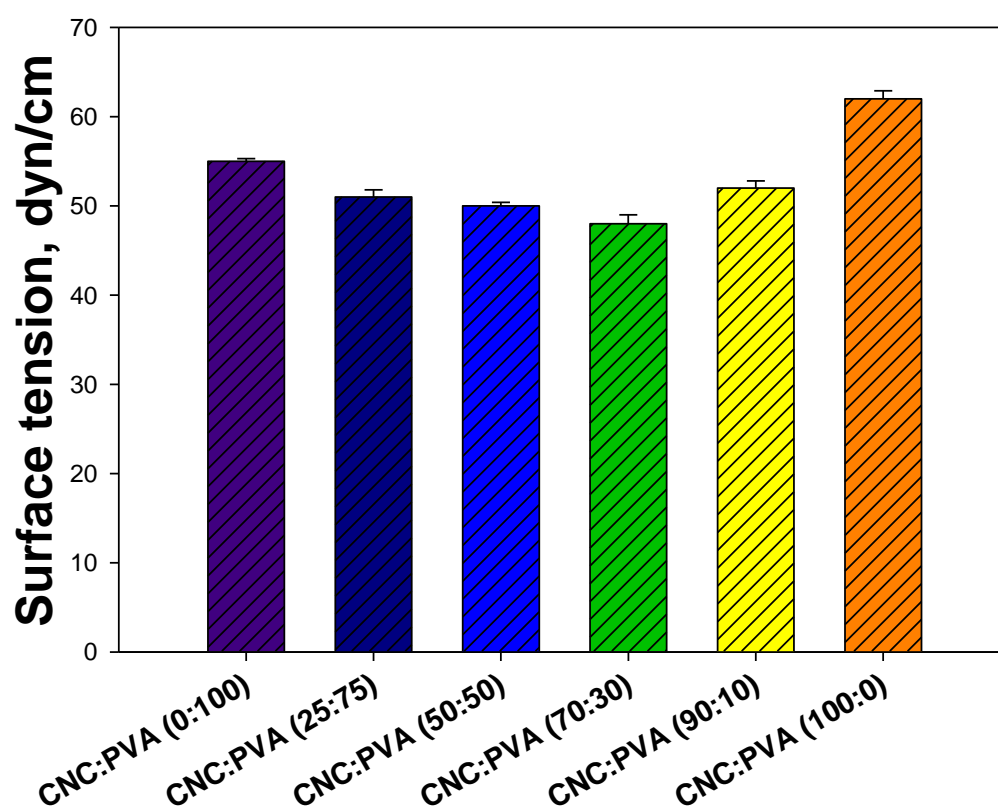


Figure 3.1 Surface tension for different CNC-PVA ink systems

The viscosity of ink is another important factor which immensely affects the uniformity and thickness of a coating. The aqueous CNC-PVA suspension showed very complex rheological behavior, as shown in Figure 3.2. The rheological behavior controlled the liquid transfer rate from the ink bath to the substrate. For the PVA solution, nearly Newtonian behavior was observed, which

implies that capillary number is insignificant for this ink system⁶⁹. After replacing part of the PVA with CNC, viscosity was reduced, and shear-thinning was prominent for CNC loading higher than 25 wt% in the CNC-PVA ink system. Due to the reduced viscosity and shear-thinning, the liquid transfer rate should be similar for every CNC-PVA composition above 25 wt% CNC at higher shear rates (200 -500 s^{-1}). Based on these rheological profiles, a moderately high shear rate (300 s^{-1}) was chosen for all coatings (details can be found in the APPENDIX B).

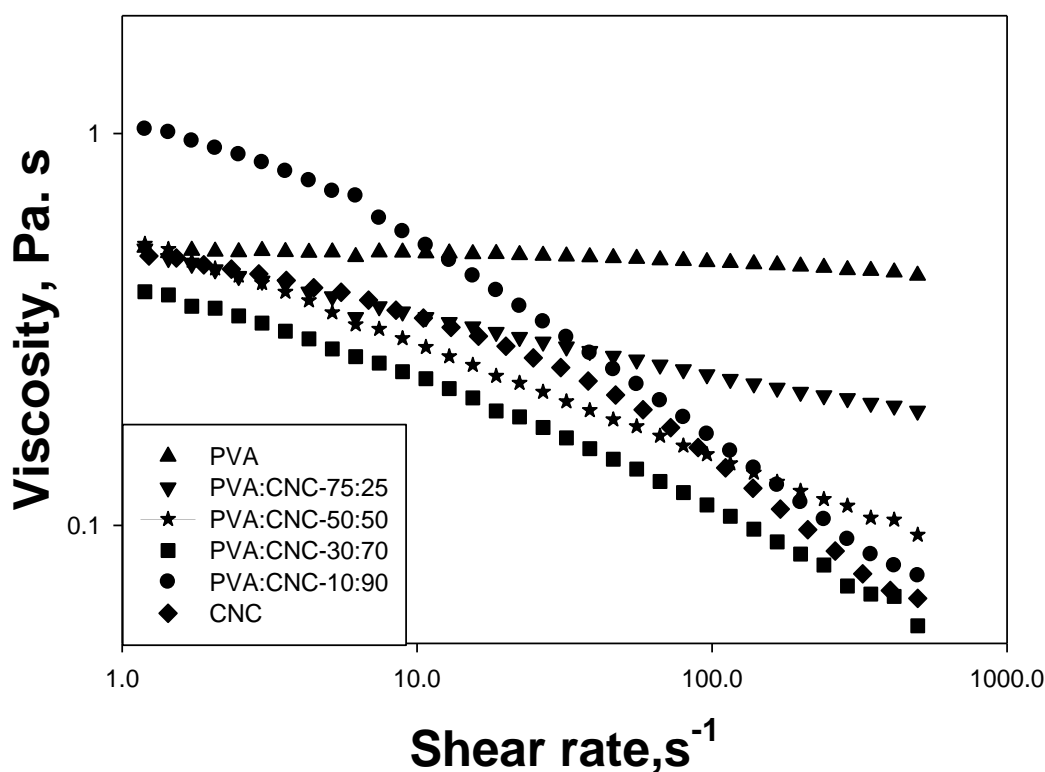


Figure 3.2 Rheological behavior of CNC-PVA ink composition at variable shear rates

The coating speed (or substrate speed that reflects maximum production rate) solely depends on the evaporation rate of the solvent, which in this case is water. As the ink system contains 88 wt% water, the ink suspension required long time for evaporation due to the high proportion of water in the ink. Due to only 2 m of substrate length before rewinding, a substrate coating rate of

1 m/min and gravure speed of 30 rpm were deemed optimal for this fabrication. At higher gravure rotation (>50 rpm for 1 m/min substrate speed), bubbles were produced on the coating surface which appeared to degrade the coating quality. The bubble formation is directly related to the capillary number of any ink system⁸⁹. The higher gravure speed leads to higher capillary numbers of the fluid system, which can entrap air bubbles on the gravure surface to produce pinholes and voids in the coating area.

3.3.2 Coating characterization

3.3.2.1 Surface roughness and coating transparency

Surface roughness (R_q , root mean square) varied with CNC-PVA composition ratio. As depicted in Figure 3.3, the two component coating systems (CNC-PVA) exhibited higher surface roughness relative to single component (CNC or PVA) coatings. This may be due to the combination of two factors; phase separation and tactoid behavior of the CNCs domains⁹⁰. At the higher content nanocellulose blends, pure PVA molecules may prefer to phase separate (nanoaggregation) from the CNCs⁹¹, which will lead to higher surface roughness. The dominant factor may be due to the formation of elliptical, spherical or spindle-shaped tactoids by liquid crystal domains of CNCs that can significantly increase the surface roughness of the coatings⁹². However, the highest surface roughness is less than 100 nm for all coating systems. The surface morphology profile for different coatings have been shown in APPENDIX B (Figure BS2).

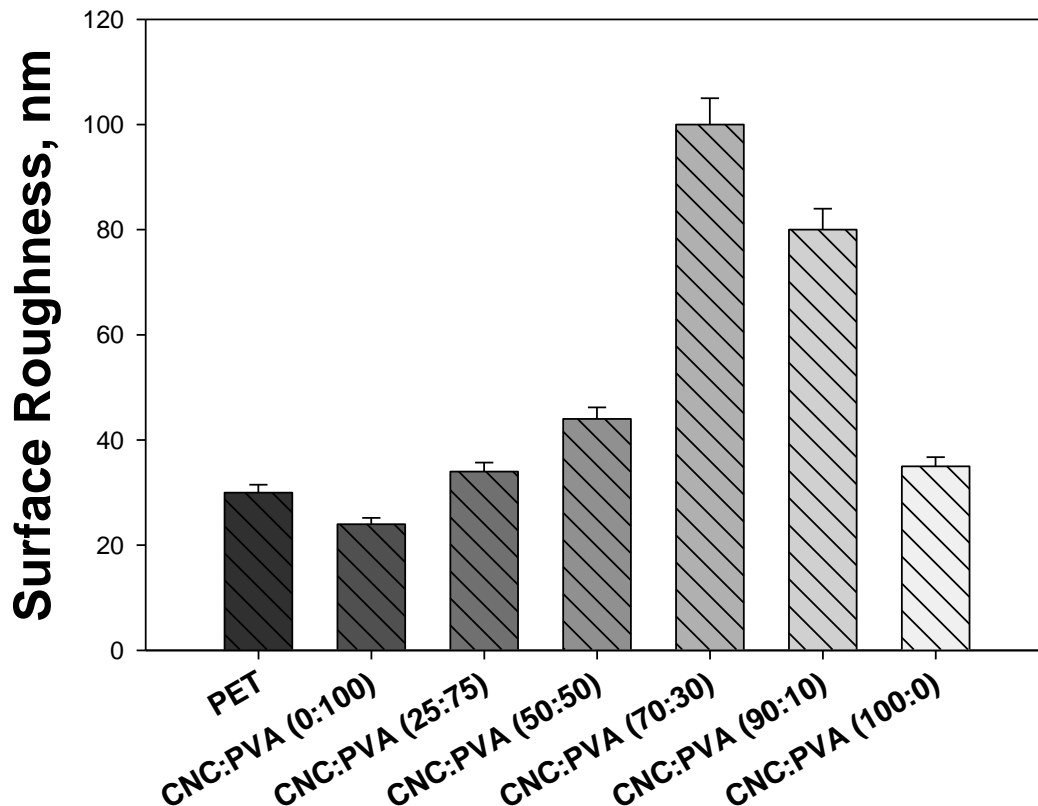


Figure 3.3 Surface roughness of uncoated PET and CNC-PVA coatings on PET substrate

Excellent optical transparency was observed for CNC-PVA coatings on the flexible PET substrate as shown in Figure 3.4. The uncoated PET substrate showed 89-92% optical transparency for a wavelength range of 350 - 750 nm. There was no significant transmittance reduction for any CNC-PVA composition relative to the uncoated PET film. Therefore, different coating compositions have minimal light scattering and reflection. In general, light scattering is attributed to surface roughness of transparent coatings, but the surface roughness for all the sample coating compositions is less than 100 nm. A maximum 3-4% transparency reduction was observed for any coating composition. While insignificant, any reduction in transparency may be due to diffraction of incident light by trace microbubbles that were observed on coating surfaces. Regardless,

transparency loss was too small to be noticed by an unaided eye (Figure 3.5). Furthermore, the samples should have very low wide angle and narrow angle scattering, hence; very low haze and high clarity was observed for CNC-PVA coatings (Figure BS7 in the APPENDIX B). This high transparency is important in commercial applications particularly in food packaging where clear display of the food product is required⁹³.

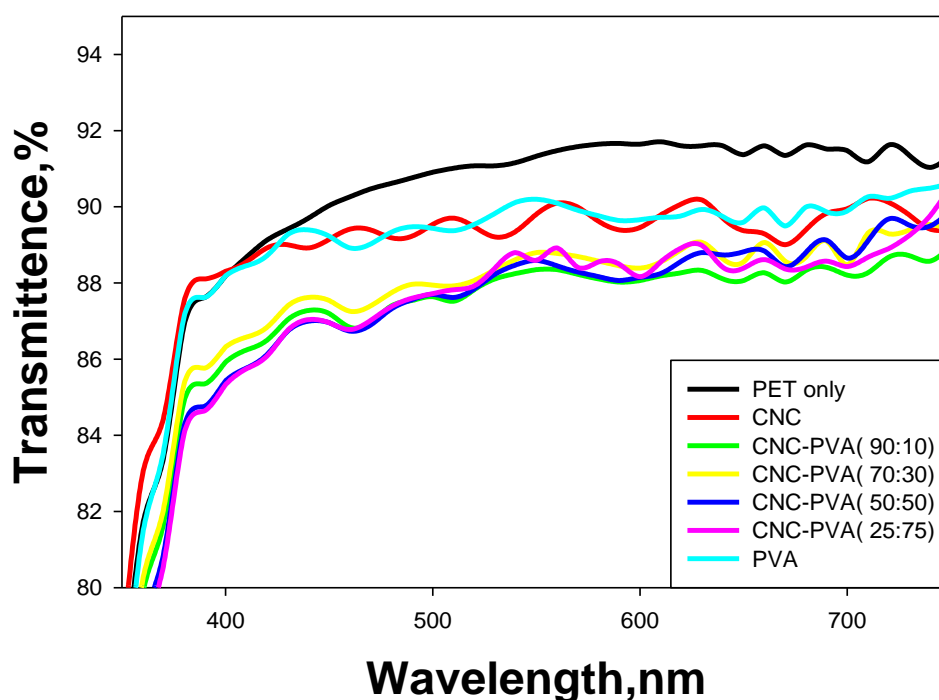


Figure 3.4 Optical transparency for different CNC-PVA composition on PET films

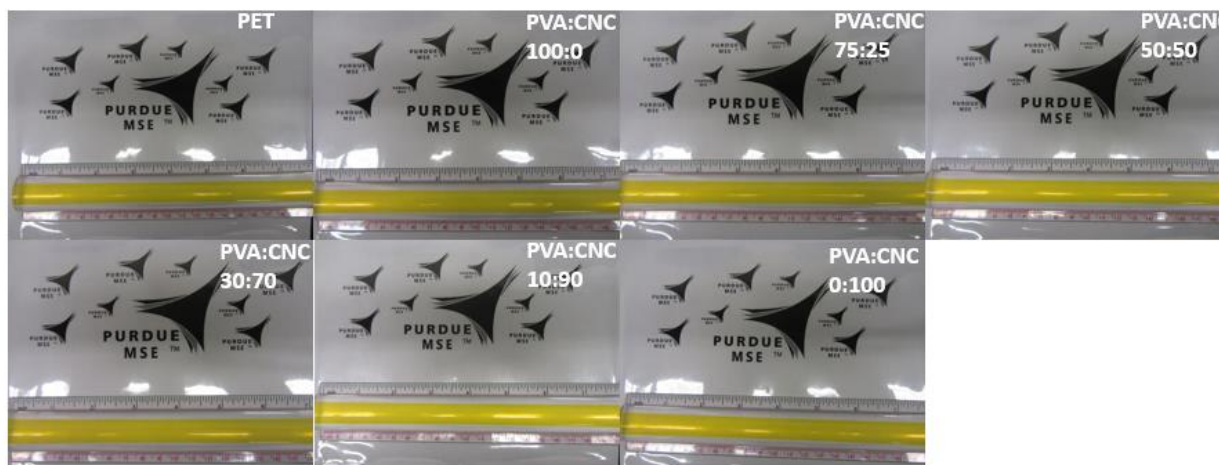


Figure 3.5 Photograph for CNC-PVA coatings on PET substrate (15 cm x 15 cm)

3.3.2.2 Coating adhesion strength

Samples of different CNC-PVA compositions were subjected to cross-hatch testing in order to determine the coating adhesion strength. The coating thickness was maintained at about 5-6 μm for each test. The adhesion loss for crosshatch adhesion test was based on visual inspection. According to the ASTM D3359 standards, samples were categorized as: 5B (0%), 4B (less than 5%), 3B (5-15%), 2B (15- 35%), 1B (35-65%) and 0B (> 65%) where 5B is considered 0% area removed from the substrate.

The adhesive strength of any coating system is determined by the interfacial strength between two dissimilar materials, coating thickness, and physical or chemical properties of the material. The interfacial strength is partly controlled by the substrate/coating compatibility. In this study, the substrate/coating compatibility for different coating formulations was ensured since the substrate have been subjected to the same corona treatment with comparable surface energies (details can be found in the APPENDIX B). Here, the surface energy of the substrate is higher than the surface tension of the various ink systems (Figure 3.1), which confirms a maximum adhesive or interfacial strength for this coating system⁶⁹. Similar coating thickness for different coating formulations was

used for this measurement. Moreover, both CNC and PVA contain OH groups in the surface and carbon-based hydrophobic backbone in their structure; hence, all coating compositions should have very strong coating strength.

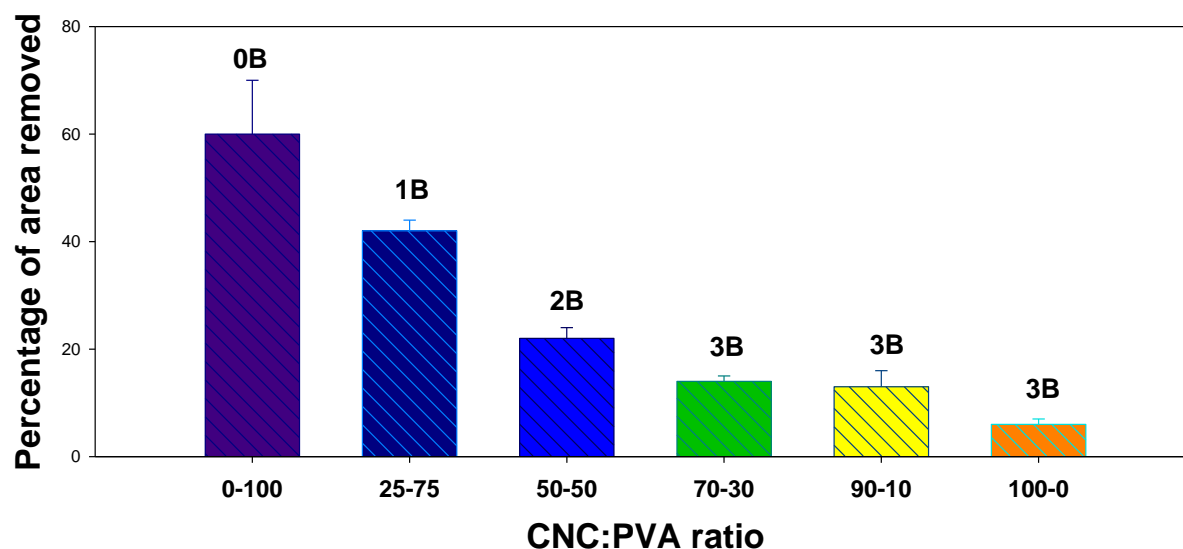


Figure 3.6 Adhesion strength for coatings

Contrary to this expectation, it was observed that the addition of CNC in CNC-PVA coating displayed progressively higher adhesive strength as illustrated in Figure 6. The reduction in adhesion strength with higher proportion of PVA could be due to a number of reasons. In the presence of shear force (due to microgravure rotation), long chain PVA molecules may not completely relax, resulting in a coating with high residual stresses⁹⁴⁻⁹⁵. The second reason could be due to the preferential entanglement of the long PVA molecular chains in the aqueous systems. The PVA polymer chains entangle among themselves and with CNCs to form a strong adhesive bond in the solid state⁹⁶. This entanglement leaves a stronger adhesion between successive PVA molecular chains or PVA - CNCs composite than between PVA or CNC - PVA and the surface of the substrate. So, when delamination of the coating is initiated, the entanglement propagates a rapid

removal of the rest of the coating from the substrate. Autophobic dewetting of PVA can be another reason for this delamination⁹⁷. However, the pure CNCs or coatings with higher CNC loading exhibited strong adhesion between the coating and the substrate. There should be some preferential specific interaction such as better hydrogen bonding or strong polar interaction between CNC and PVA molecules. Lastly, changes in modulus and elasticity could lead to differences in adhesion⁹⁸.

3.3.3 Effect of CNC loading on coating anisotropy

Herman's order parameter was calculated from transmitted light intensity for different coatings (on the PET substrate) to determine anisotropy based upon a previously reported method⁶⁹. Based on the transmitted light intensity profile for 45° and 90° configurations, the dichroic ratio, D , was determined for each coating. Finally, the order parameter, S , was determined by equation 2. For any isotropic arrangement, 45° and 90° configurations showed similar intensity profile ($D \approx 1$) due to negligible refractive index difference for longitudinal and transverse directions. But, the anisotropic arrangement showed maximum transmittance intensity difference between 45° and 90° configurations that suggests that there was a preferential alignment of the crystalline domains along the shear direction (APPENDIX B, Figure BS4).

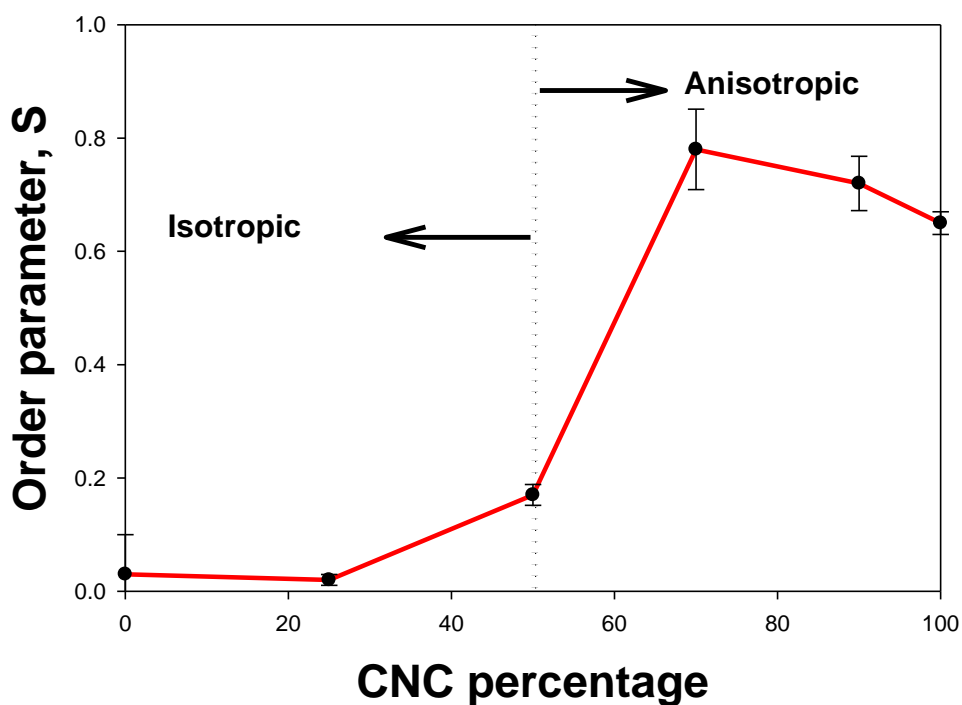


Figure 3.7 Order parameter for different coating system

For a constant shear rate (approximately 300 s^{-1}), the order parameter for different coating compositions is shown in Figure 3.7. It is observed that CNC loading controls the overall anisotropy of the CNC-PVA coatings. At 0-50% CNC loading in the dry film, the ink system mostly displayed an isotropic arrangement. However, there was a sudden increase in anisotropy up to a maximum order parameter of 0.78 at 70% CNC loading. The anisotropy was steady up to a 90% CNC loading. Finally, the order parameter reduced to 0.65 for pure CNC coating.

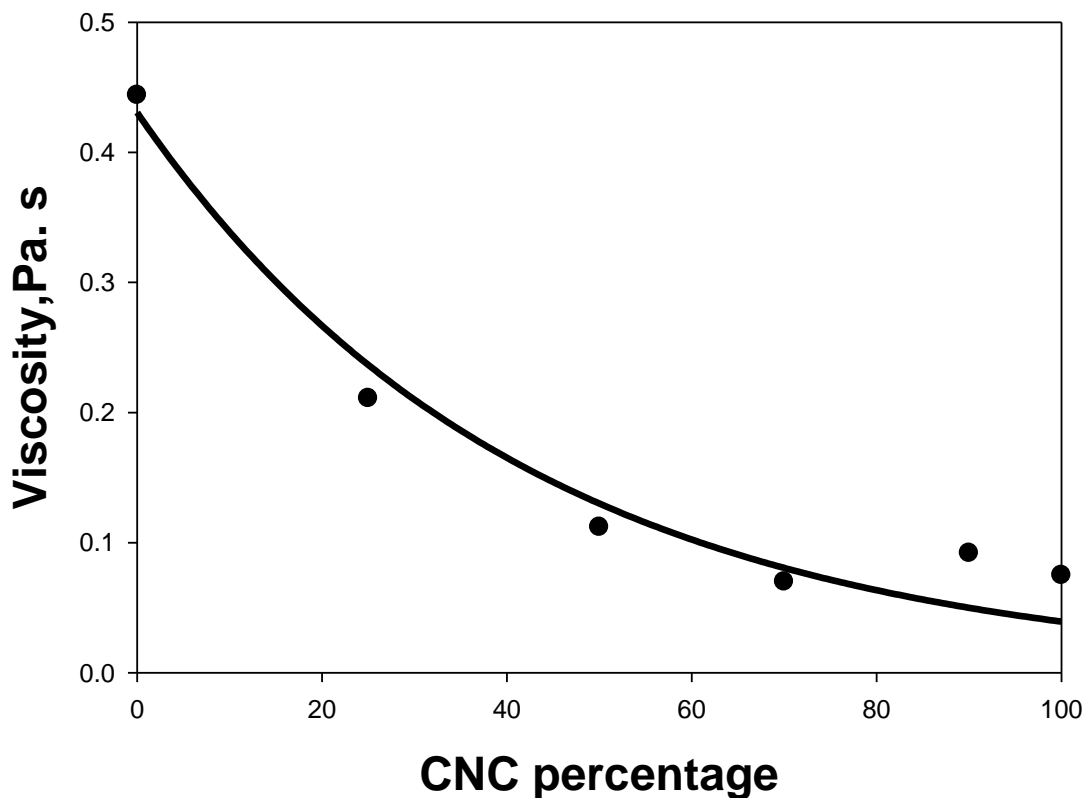


Figure 3.8 Apparent viscosity for CNC-PVA (12wt% solid loading) nanocomposites system with different CNC percentage at 300 s^{-1} shear rate (line added to aid the eye).

In the aqueous system, due to its long chains, PVA has a swollen gel structure with many entanglements. Hence, shear alignment must be difficult for the PVA solution. Therefore, the CNC is the key factor for the coating anisotropy, whose alignment is determined by the combined effect of shear rate and crystalline domains retention time. The shear rate depends on the gravure rotation. However, a constant gravure rotation was used for this fabrication, so the overall coating anisotropy should mainly depend on the CNC content and the domain relaxation time. The relaxation time for CNC movement is determined by the viscosity of the ink system⁴⁴. More viscous ink systems are expected to exhibit higher relaxation times as compared to less viscous ones. As viscosity is decreased with increased CNC percentage (Figure 3.8), it is expected that higher CNC loading ink

should have a faster relaxation time thus corresponding with a lower order parameter. However, highly anisotropic coatings were observed at higher CNC loadings even though ink viscosity decreased compared to lower CNC percentage loading. For CNC loading less than 50 wt%, the applied shear rate (300 s^{-1}) may not be sufficient to produce an anisotropic coating. This could be due to the entrapment of the CNC domains in the globular structure of the PVA chain that hinders the alignment of CNC domains along the shear direction. To validate this assessment, real time birefringence measurements were made for the various CNC-PVA compositions as illustrated in Figure 3.9.

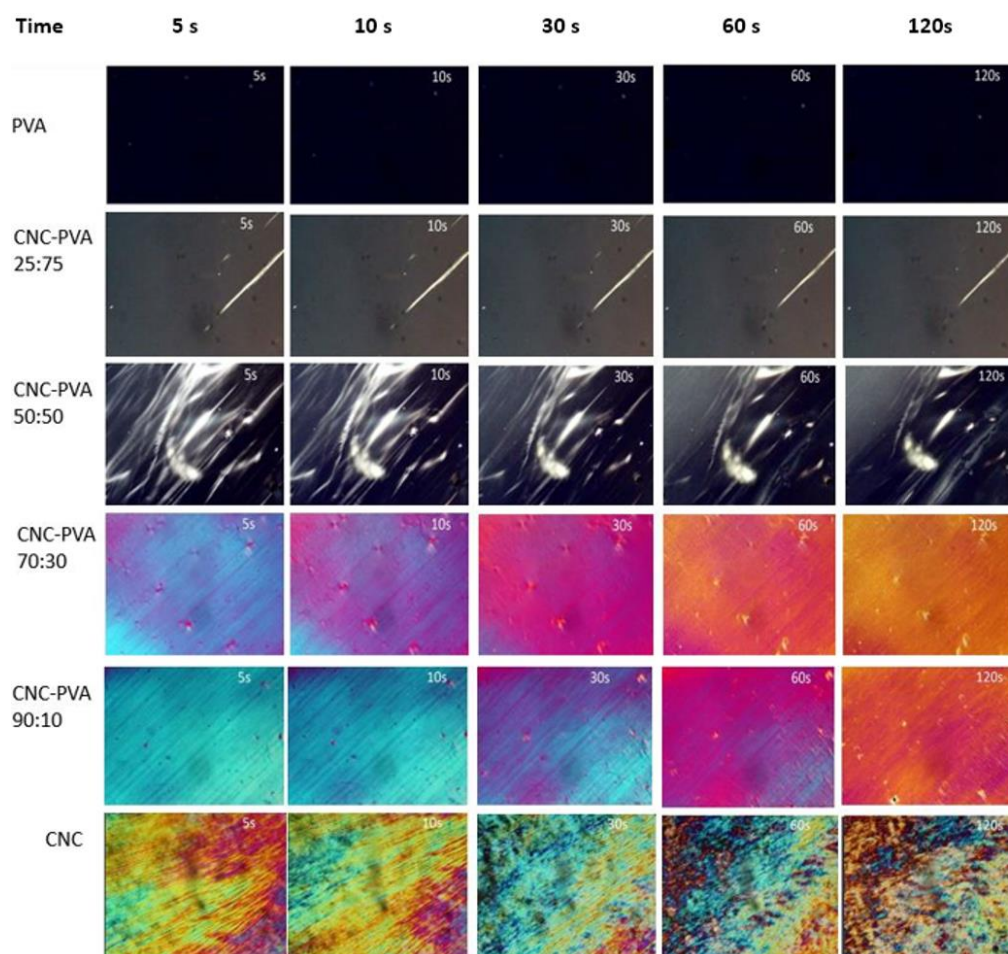


Figure 3.9 Real time birefringence observation for different ink compositions

Real-time particle movement was investigated along the shear direction for different CNC-PVA compositions (measurement process can be found in the APPENDIX B). It should be noted that this experiment has been performed in an aqueous system with a constant shear rate (300 s^{-1}). Little birefringence was observed for less than 50 wt% CNC loading. This is a clear indication of a mostly isotropic arrangement. As CNC percentage loading was increased to 70 wt%, the presence of birefringence was observed with intense coloration. Thus, a certain threshold CNC percentage loading is required to exhibit large-scale birefringence. The maximum color intensity of the 70% and 90% CNC composition confirmed maximum anisotropy, which is consistent with the order parameter study shown earlier. The pure CNC coating also showed birefringence, but color intensity reduced over the observation time which suggested faster domain relaxation. The experiment was performed under open atmosphere so three possibilities arise. In the first scenario, faster water evaporation may lead to rapid thickness reduction of the CNC-PVA solution, which resulted in the fading of the color over time. The second reason could be the effect of Brownian motion or rapid chain relaxation leading to thickness variation that produced the color change overtime. The change in momentum of the crystalline domains or polymer chains could be another reason for color variation. As a rapid shear force is applied on the CNC-PVA solution, the CNC crystalline domains and the PVA polymer chains could acquire energy by attaining higher momentum. However, as the source of this force is removed, the crystalline domains or polymer chains begin to relax. The CNCs or polymer chains lose their acquired momentum by dissipating the adsorbed energy which is accompanied by the various color changes.

It is worth mentioning that the birefringence of CNC-PVA ink systems with higher than 50% CNC loading did not change over time (from 0 to 120 s). But a reduction of birefringence (from 0-120 s) was noticeable for the pure CNC system. So, CNC-PVA ink systems with birefringence

should have higher order parameter compared to pristine CNC system. The entrapment or locking of CNC crystalline domains with the long chain PVA polymer may be a reason for this observation.

3.3.4 Water vapor transmission rate (WVTR)

Water vapor transmission rate (WVTR) is a fundamental parameter that details the degree to which water vapor (humidity) can transport through a solid film. A good barrier film/coating for food packaging applications will have a low WVTR value. The mechanism of water vapor transmission depends on free volume, packing density, crystalline-amorphous ratio and hydrophilic/hydrophobic nature of the polymeric materials. PET substrates possess excellent water resistance property compared to CNC-PVA composite coatings. Hence; PLA was chosen as it is known to have a relatively high WVTR that precludes its use in many applications⁹⁹. WVTR for different CNC-PVA coatings on the poly (lactic acid) (PLA) substrate has been shown in Figure 3.10. There was a noticeable reduction in the WVTR with increasing CNC loading, which was reported previously (where CNC was used as a filler)¹⁰⁰. The crystalline domains of CNC act as a physical barrier (due to higher packing density) and creates a longer tortuous path for the permeation of moisture molecules.

The lowest WVTR was observed at 70% CNC loading as compared to any other composition. As indicated earlier, this composition exhibited the maximum order parameter, 0.78, which reduced the free volume of the coating system. So, the combined effect of reduced free volume and increased path-length due to the CNC content lowered the WVTR. However, for CNC loading more than 70%, permeability again increased with increasing CNC loading which clearly contradicts expectation¹⁰⁰. Based on this experimental result, two possible reasons can be deduced for the increment of WVTR. There must be some critical PVA percentage loading where PVA chains can either fill the gap among CNC domains or form a network structure with the CNCs

through intermolecular hydrogen bonding with minimum free volume. Below this critical PVA percentage loading, there should be some free volume that enhances WVTR. Another possible reason can be attributed to swelling of the CNC – PVA polymer coating system. After moisture absorption, CNC domains can dislocate from their original position which may provide additional free volume by reducing the overall order parameter.

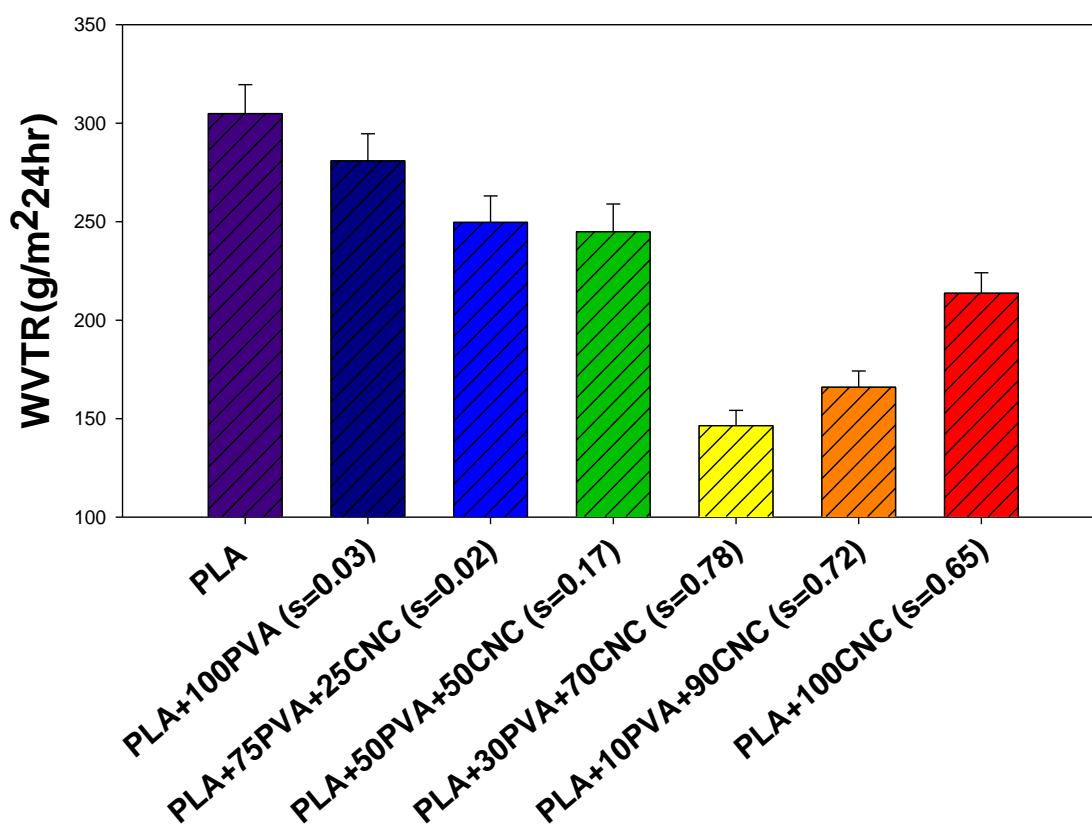


Figure 3.10 WVTR with corresponding order parameter for different CNC-PVA coating compositions on a PLA substrate

A Comparative data for cellulose nanomaterials has been shown in Table 3-2. It is also worth mentioning that WVTR reported here is based on anisotropic domains orientation and no literature data is available regarding the orientation effect. However, the WVTR values of CNC-PVA

coatings are similar compared to the different types of nanocellulose composite materials found from the literature.

Table 3-2 WVTR with corresponding order parameter for different CNC-PVA coating compositions on a PLA substrate

Sample	Matrix	Filler/ Additive	Substrate	Order parameter	Relative Humidity	WVTR (g/m ² / 24hr)	Method	Reference
Xylan-CNC	Xylan	CNC (whisker)	-----	-----	Not reported	174	Wet cup	101
CNC- Vermiculite	CNC	Vermiculite	----- -	-----	50%	70-15.4	Macon	102
CNF	CNF	-----	----- -	-----	50%	234	Dry cup	103
CNF coating	CNF	CMC	Paper board	-----	50%	100	Dry cup	53
CNF-Mica	CNF	Mica	----- -	-----	60%	200	Dry cup	104
CNF	CNF	-----	----- ---	-----	50%	132	Wet cup	105
CNC-PVA	CNC	PVA	PLA	0.78	3%	160	Wet cup	This work

3.4 Summary

Large-scale fabrication of anisotropic CNC – PVA coatings could be useful in the production of coatings for applications in several fields such as food packaging, flexible electronics, and other emerging applications. In this study, a method for CNC– PVA coatings on a flexible substrate has been developed with roll-to-roll production. Various weight ratios of PVA-CNC were examined to assess the effect on CNC anisotropy which governs coating properties. All films exhibited excellent optical transparency and very uniform coating thicknesses (roughness less than 100nm). The coating adhesion strength was improved with the addition of CNC and maximum coating adhesion was observed above 70 wt% CNC.

An isotropic to anisotropic transition was observed over 50 wt% CNC. This sudden increment in order parameter indicates that a certain critical concentration of CNC is necessary for the

alignment of the CNC along the shear direction. Real-time birefringence experiments also confirmed this phenomenon. As mentioned previously, the anisotropy plays an important role in coating properties. The WVTR initially decreased with the addition of CNC up to 70 wt% CNC ($S=0.78$). Above 70 wt% CNC, anisotropy began to decrease and the WVTR began to increase which suggests that there is a critical concentration of CNC required to achieve the lowest free volume of the coating system. This study further demonstrated the importance of control of anisotropy in CNC and CNC composite coatings, as well as the role of CNC concentration in anisotropy of CNC composite coatings.

CHAPTER 4. CELLULOSE NANOCRYSTAL (CNC) COATINGS WITH CONTROLLED ANISOTROPY AS HIGH-PERFORMANCE GAS BARRIER FILMS

All lab work except gas permeability, XRD, TEM and zeta potential measurements was performed by Reaz Chowdhury. All analysis except crystallinity index, and zeta potential was performed by Reaz Chowdhury with guidance by Prof. Jeffrey P. Youngblood. All writing was performed by Reaz Chowdhury with guidance and editing by Prof. Jeffrey P. Youngblood and Prof. John Howarter.

The following chapter contains content reproduced with permission from R. A. Chowdhury, M. Nuruddin, C. Clarkson, F. Montes, J. Howarter, and J. P. Youngblood, "Cellulose Nanocrystal (CNC) Coatings with Controlled Anisotropy as High-Performance Gas Barrier Films," *ACS applied materials & interfaces*, vol. 11, no. 1, pp. 1376-1383, 2018. Copyright 2018 American Chemical Society.

4.1 Introduction

Polymeric barrier films are essential for several applications ranging from electronics (flexible devices, OLED, solar cells, photovoltaic devices or vacuum insulation panels) to food packaging¹⁰⁶⁻¹¹². Different applications require different extents of barrier performance; for instance, electronic devices should have higher barrier performance compared to food packaging¹¹³⁻¹¹⁴. Polymers with inorganic coatings can offer superior barrier performance in these applications¹¹⁵. However, due to high processing cost and inevitable coating defects, use of inorganic coatings on polymeric film is limited in high barrier applications¹¹⁶. Moreover, many coatings such as graphene oxide exhibit reduced transparency which limits the use of these materials in optically sensitive applications such as opto-electronic devices (such as OLED, solar cells, or photovoltaic)¹¹⁷ or for transparent packaging. Multilayer polymeric films are another possible solution for the fabrication of high barrier films¹¹⁸⁻¹²⁵. However, post-processing after its life cycle is a significant drawback for multilayer film approaches. Alternatively, several research groups are working on the development of single layer high-performance barrier films¹²⁶⁻¹³³. Most of this research is based on polymer

nanocomposites where matrix-filler compatibility can be challenging, and additional study is needed on the effect of structural morphology on the polymeric barrier efficiency.

Cellulose nanomaterials such as cellulose nanocrystals (CNC) and cellulose nanofibrils (CNF) have drawn a wide interest for packaging due to its improved barrier properties compared to other bio-polymers¹³⁴⁻¹³⁶. CNF have a high aspect ratio (4-20nm wide, 500-2000nm in length) with amorphous and crystalline regions⁵. CNCs are rod-like (5-10nm wide, 100-200nm long) and typically higher crystallinity compared to CNFs. Both types offer superior properties like strength, stiffness, and thermal conductivity compared to more amorphous materials^{5, 25, 28}. Controlled arrangements of these anisotropic nanomaterials can exhibit unique structure-property interactions which may be useful for several applications such as optical sensors (photonics)¹³⁷, direction-dependent thermal conductivity²⁵, security printing³¹, flexible electronics¹³⁷, and packaging¹³⁸.

CNC/CNF in packaging applications are used as a filler or modifier in engineering polymers in which these materials improve the polymer barrier properties against oxygen, oil or grease, and water vapor¹³⁸. Addition of nanocellulose to a polymer can provide excess crystalline domains that reduce the overall free volume of the system. Moreover, the high crystallinity of CNC/CNF impedes permeability to gas and vapor, hence, overall barrier properties can be improved. CNC/CNF materials are also used as coatings to enhance the barrier performance. In general, these barrier properties (except water vapor barrier) are comparable to those of engineering polymers (like PP, PE, PLA, etc.), but, exhibit inferior/degraded barrier properties relative to most of the traditional barrier polymers (e.g., PET, EVOH, etc.).

While cellulose nanocomposite films (either as a polymer filler or by themselves) have been investigated for barrier performance, to the best of our knowledge, no in-depth investigation has been performed on the effect of the structural organization for a nanocomposite or pure nanocellulose system on their barrier properties. Isotropic films can be made simply by solution

casting, but, difficulties arise for anisotropic sample preparation. In general, anisotropic films are very brittle and cannot be easily delaminated to form free-standing films without the formation of microcracks after delamination. Obtaining defect-free, free-standing anisotropic films greater than a millimeter is very challenging which is why these films cannot be used to measure the barrier performance.

In the current study, gas permeability for pristine cellulose nanomaterials (both CNC and CNF) were investigated. Films with isotropic and CNCs with various degrees of anisotropy were prepared with a controlled thickness (because an anisotropic film less than 15 μ m thickness is flexible) and the corresponding O₂ and CO₂ gas barrier properties were measured for these coatings and films. The resultant barrier properties were correlated with crystalline alignment (Herman's order parameter) which is related to free volume (packing density) of system. Finally, the "Bharadwaj" model of polymer nanocomposite gas permeability data was modified for a pure nanoparticle system and the CNC data fitted.

4.2 Experimental

4.2.1 Materials and film fabrication

Never dried 12.2 wt% cellulose nanocrystal aqueous suspension (batch no-2015 FPL- 071 CNC) containing 1wt% sulfur with Na⁺ counterion) and 0.82 wt% TEMPO modified cellulose nanofibril aqueous suspension (batch no- 2014-FPL-CNF-080) were purchased from the University of Maine (Orono, Maine, USA), and manufactured by the US Department of Agriculture Forest Service-Forest Product Laboratory (Madison, Wisconsin, USA). These materials, which are currently produced at pilot scale, are relatively consistent between batches and widely available for research. TEMPO CNF was selected for comparison as TEMPO CNF possessed superior properties compared to mechanically fibrillated CNF, which is another common nanomaterial available.

Cellulose nanomaterial was used without any additional purification. Polylactic acid (PLA) flexible film was received from Cargill Dow LLC (Minnetonka, MN, USA) and used as a substrate for anisotropic CNC coatings. Linear polarizing film with 42% single pass transmission (AP42-007T) was purchased from American Polarizer, Inc, Reading, PA, USA. Dry gas for O₂ and CO₂ experiments were purchased from Indiana Oxygen (Lafayette, IN, USA). The purity of dry O₂ and CO₂ gases were 99.5% and 99.9%, respectively.

Cellulose nanoparticles were characterized for crystallinity index, particle dimension and zeta potential of the suspension and the characterization methods can be found in the literature. The average particle size and width (based on TEM image) were 100 nm and 5nm respectively. The average zeta potential for CNC suspensions was -45.5 mV and the crystallinity index for CNC was 89 %. Details for the TEM, XRD and Zeta potential analysis can be found in the APPENDIX C.

Self-organized CNC films were prepared from 2wt% aqueous suspension. Briefly, 20ml CNC suspension was poured into a Petri dish (8cm diameter) and dried at ambient conditions (23°C and 50% relative humidity) for 3-4 days. A test specimen (25 mm diameter with 42μm thickness) was obtained from the middle area of the film and conditioned in a desiccator before the experiment was performed. A similar fabrication process was used for the preparation of random CNF films.

Anisotropic free-standing CNC films are very brittle above 15-18μm thickness, and it is not possible to prepare a crack-free anisotropic film of larger dimension. A rod coater (K- hand coater) purchased from RK Print Coat Instruments Ltd. (United Kingdom) was used to produce anisotropic CNC coatings on a flexible PLA substrate. Various CNC concentrations were used for anisotropic coatings and the details can be found in Table 4-1. The surface tension (56-60 dynes/cm measured by pendant drop tensiometry) of the CNC suspension was higher than the PLA (46-56 dynes/cm measured by dyne pen) substrate. Hence, surface treatment on the PLA surface was essential for the suspension- substrate compatibility. It was observed that 5-10 mins of corona treatment on the

PLA substrate was sufficient to make it compatible with the CNC suspension. Immediately after the coating, the film was transferred to an oven (at 40°C for 5 mins) to completely dry and lock in anisotropy. Films were conditioned in a desiccator until future use.

4.2.2 Film characterization

A Carl Zeiss (Axio observer A1) inverted polarized light microscope in transmission mode was used for sample analysis. Samples were imaged at 45° and 90° to the linear polarized light in bright and dark field images.

A conventional UV-Vis spectrophotometer (Spectra max Plus 384, Molecular devices Corm. Sunnyvale, CA) was used for the measurement of alignment in cellulose nanomaterials. The detailed procedure can be found in the literature³⁸. Briefly, a free-standing sample (hence, delaminated from the substrate) was placed between a cross-polarizer and the transmitted light intensity (from 400 nm to 750 nm) was measured at 45° and 90° configurations. The Herman's order parameter (S) was calculated from the following equation:

$$I_{\theta} = I_0 \sin^2 2\theta \sin^2 \left(\frac{\pi \Delta n d}{\lambda} \right) \dots \dots \dots (4.1)$$

Hence,

$$\frac{I_{45}}{I_{90}} = D^* = D \cdot g = \frac{(2S+1)}{(1-S)} \dots \dots \dots (4.2)$$

Here, I_0 , θ , Δn , d , λ , I_{45} , I_{90} , g and D represent the amplitude of the incident light, sample angle regarding incident light, refractive index difference, film thickness, wavelength, transmitted light intensity for the 45° configuration, transmitted light intensity for the 90° configuration, correction factor and dichroic ratio, respectively. The value determined by this method is an average over the beam size of the spectrophotometer, and as previously shown by Chowdhury *et al.*, is independent of sample thickness within the range of this study. For any material, $S=0$ is defined as the random configuration and $S=1$ is for the perfect anisotropic arrangement.

4.2.3 Gas permeability measurement

The design of a permeability measurement instrument is shown in appendix-c (Figure CS1.). The permeation test of O₂ and CO₂ gas were performed at room temperature using a constant-volume/variable-pressure permeation system¹³⁹. The upstream pressure of the system was measured by a digital pressure transducer with a maximum pressure output of 100 psi (GS4200, Ellison Sensors, Inc., FL, USA). A Baratron 627E ethernet enabled capacitance manometer with a maximum pressure output of 10 Torr (MKS, Wilmington, MA) was used to measure the downstream pressure.

Polymer films with 25 mm diameter were cut precisely with high precision scissors. The thickness of the films was measured five times with a micrometer (Marathon Electronic digital micrometer), and the average value was taken as a thickness of the films. The film was enclosed inside a Millipore stainless steel high-pressure filter holder (Millipore Sigma, MA, USA) with an exposed area of 2.7 cm² for transportation. Initially, the entire permeation system was degassed by vacuum for 12 hours to remove entrapped air and moisture and then the valves connecting the film holder were closed. The slow pressure rises over time in the downstream volume due to leakage of the system (the leak rate) was measured. The feed gas (O₂, CO₂) was introduced to the upstream side at a fixed pressure and the pressure rise in the downstream volume as a function of time was measured. The leak rate was verified to be at least ten times less than the measured steady state pressure rise due to permeation of gas through the polymer films.

The gas permeability of the film was calculated using the following expression¹³⁹:

$$P_A = \frac{V_d l}{P_2 A R T} \left[\left(\frac{dP}{dT} \right)_{ss} - \left(\frac{dP}{dT} \right)_{leak} \right] \dots \dots \dots (4.3)$$

Where, V_d (cm³) is the downstream volume (volume of tank and tube), l is the film thickness (cm), P₂ is the upstream absolute pressure (cmHg), A is the film's exposed area for gas transportation

(cm²), R is the gas constant (0.278 cmHg cm³/[cm³(STP)K], and T is absolute temperature (K). Furthermore, $(\frac{dp}{dt})_{ss}$ and $(\frac{dp}{dt})_{leak}$ are the steady state pressure rise in the downstream volume during leak testing and gas permeation through the films.

The gas permeability of the polymer coating was calculated using the following expression¹⁴⁰:

$$P_c = \frac{h_c}{\frac{h_1}{P_1} + \frac{h_2}{P_2}} \dots\dots\dots(4.4)$$

Where P_c is total permeability, h_c is total thickness of the film, h_1 is the substrate thickness, P_1 is the substrate permeability, h_2 is the coating thickness and P_2 is the coating permeability of the polymer system.


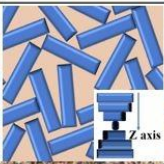
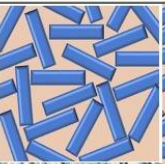
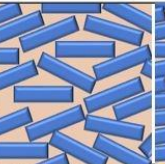
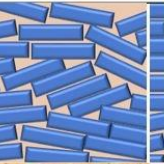
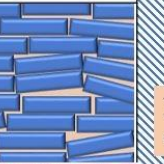
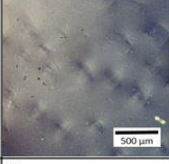
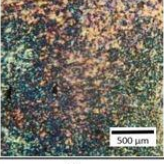
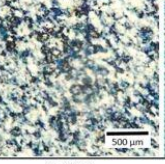
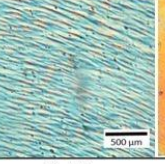
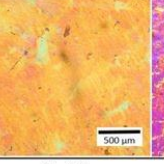
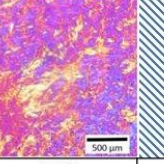
4.3 Results and discussion

4.3.1 Orientation of crystalline domains in bulk cellulose nanomaterials

The dried solution cast CNC and CNF films (without shear) exhibited two different types of microstructural organization of the crystalline domains (Table 4-1). CNC formed a chiral nematic orientation that is concentration dependent. The rod-shaped crystalline domains are in a cholesteric phase where each plane (local order) is rotated by a phase angle. Due to the presence of the phase angle between two planes, the chiral nematic configuration possesses a lower packing density that is determined by the helical pitch length⁵. In CNF films, long cellulose fibrils have very high aspect ratios that can entangle each other and form a random configuration. The packing density of CNF films are a little higher than the chiral nematic CNC films, but, both have an isotropic configuration. The degree of orientation for chiral nematic CNC and random CNF films was measured by birefringence and quantified by Herman's order parameter. Both films exhibited similar transmittance for 45° and 90° (to the polarizer) which confirmed an isotropic arrangement. For

anisotropic materials, the CNCs are parallel to the shear direction (Table 4-1). The transmitted light intensity difference between 45° and 90° configurations is related to the extent of the anisotropy³⁸. The transmitted light intensity for different cellulose nanomaterials has been shown in Table 4-1.

Table 4-1 Different parameters of the Nanocellulose films with corresponding crystalline domains arrangement

Transmitted light intensity at 90°	6.67	19.65	29.80	19.13	8.9	4.73	Not obtainable
Transmitted light intensity at 45°	5.32	20.86	64.57	74.29	60.15	85.21	
Initial solution concentration, wt%	0.82	2.0	6.0	9.0	10.0	12.2	
Schematic representation for crystalline domains arrangement (top view)							
Optical microscope image between cross polarizer for 45° configuration							
Order parameter(S)	0	0	0.28	0.49	0.66	0.85	<u>0.86-1.00</u>
	← CNF		CNC →				

Note: The transmittance for zero order parameter films are direction independent (45 and 90° configurations are interchangeable). The isotropic configuration of CNC can be chiral nematic or random where, for chiral nematic, X, Y=random but, Z=ordered, for random, X=Y=Z=random. The aspect ratio (A.R) of CNCs for schematic diagrams (A.R of CNF > A.R of CNC) is not in scale (here, X, Y are in plane for the axial and transverse directions, respectively, but, Z is out of plane in the perpendicular direction).

4.3.2 Gas permeability in cellulose nanomaterials

For polymeric materials, gas permeability depends on the solubility and diffusivity of the gas molecules in the material. Diffusivity contributes more than solubility for the improvement of barrier performance in a conventional polymer system. However, the solubility contribution cannot be ignored as gas sorption is crucial for selective gas permeability¹⁴¹.

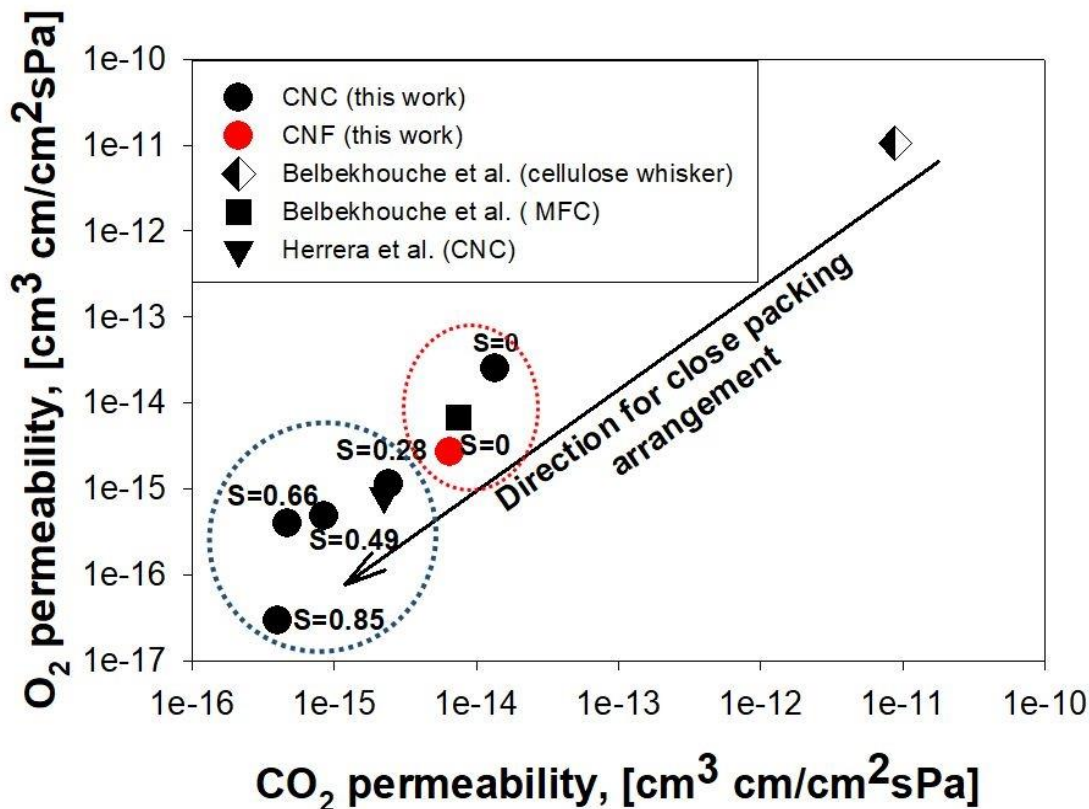


Figure 4.1 Permeability of cellulose nanomaterials. Here, red circle and blue circle area are denoted for isotropic and anisotropic CNCs, respectively, with higher barrier anisotropic CNC materials having higher progressively higher anisotropy. Literature data was based on pristine cellulose materials¹⁴²⁻¹⁴³, but no information was available regarding orientation or packing density.

It has been widely accepted that the degree of crystallinity and aspect ratio of crystalline domains play an essential role in the barrier property of cellulose nanomaterials¹³⁸. However, the degree of anisotropy (which changes the packing density/free volume of the polymer system) should change the overall gas permeability, however no previous study has been performed on orientation effects in cellulose nanomaterials. A distinct change in permeability has been observed for different alignments (Figure 4.1). Chiral nematic (CNC) or random (CNF) domains arrangement demonstrated much lower barrier performance compared to anisotropic CNC for both O₂ and CO₂. A 900-fold improvement for O₂ and 40-fold improvement for CO₂ was observed for the highest anisotropy CNC materials as compared to the isotropic CNC. Several parameters such

as polymer morphology, polymer chemistry, and physical property of gas molecules collectively explain this observation.

In general, polymer morphology and chemistry such as crystallinity, chemical bonding type, and finally free volume are the most critical properties to control the diffusion rate of gas molecules in a polymer system^{138, 144-145}. The crystallinity index for the CNC raw materials was 89% with amorphous and semi-amorphous regions (details can be found in the APPENDIX C). As no chemical treatment was conducted, the assumption is that there is no change in the overall crystallinity of the CNC and therefore this is not the controlling factor for improvement in barrier properties. However, the arrangement of CNCs solely controls the overall free volume in this materials system. As we previously described, the chiral nematic arrangement possesses the lowest packing density compared to the anisotropic arrangement. In the chiral nematic microstructure, any two adjacent liquid crystal domains are at non-zero angles, which also provides additional free volume that allow penetrant molecules a diffusive pathway for transport. In contrast, all CNCs are in the same direction for the anisotropic arrangement which leads to a high packing density, and therefore, a low free volume that provides for a tortuous path that lowers gas diffusion across the film. Thus, material structure, and therefore processing can have a large impact on the barrier properties of these materials.

Polymer-gas interaction is another important parameter that controls the gas sorption (solubility) of penetrant in a particular polymer system¹⁴¹. Based on the dual mode sorption model, sorption capacity and affinity of penetrant sorption in the polymer environment control the overall solubility¹⁴⁶. However, sorption capacity (active site for gas sorption that is related with free volume) is constant for any specific anisotropy/microstructure and can be ignored. The chemical composition of the polymer system and physical properties (such as polarity, and size) of gas

molecules collectively control the solubility within a specific polymer system. As in solvents, non-polar gas molecules show limited interaction with polar polymer systems¹⁴⁷. (Nano)cellulose materials are polar in nature due to the presence of large amounts of hydroxyls bonds. Thus, the solubility coefficient for oxygen molecules is very low, and therefore, the overall permeability will be very low as observed in Figure 4.1. Like O₂, CO₂ is also a non-polar molecule (because it does not have any permanent dipole moment), and will also have a relatively low permeability. Therefore, the permeability of CO₂ gas is always larger than O₂ in these materials (Figure 4.1) and the most anisotropic films showed about 13-fold higher permeability.

Molecular shape and its bond electron distribution significantly control the dipole moment of the gas molecule. Due to the presence of strong polar internal bonds (a partial positive charge on the carbon atom and negative charge on the oxygen atom), CO₂ gas molecules possess an electronic quadrupole moment that can induce a polar interaction with a polar material¹⁴⁷. CO₂ can act as a Lewis acid in the presence of electron donor groups and can form a coordinate covalent bond. Nanocellulose contains many hydroxyl groups with trace amounts of hemiacetal or aldehyde which are the potential sources as electron donor groups¹⁴⁸. Thus, a strong interaction between the carbon atoms in CO₂ and oxygen atoms (from –OH/C=O) in cellulose leads to CO₂ gas sorption in the cellulose nanomaterials. Additionally, at high pressures CO₂ sorption is known to induce plasticization in many materials, which leads to higher CO₂ gas permeability¹⁴⁹. Here, the sorption of CO₂ molecules may reduce the overall intermolecular polar interaction between the CNCs and create additional sites for CO₂ sorption, leading to higher permeability.

4.3.3 Bharadwaj model and its modification for the CNC system

The Bharadwaj model is one of the successful models that can predict the gas barrier performance of a nanocomposite system¹⁵⁰. Briefly, the Nielsen model was modified to correlate

the particles orientation factor for the longer diffusive path of gas molecules. Overall, for a nanocomposite, the filler nanoparticles act as a physical barrier in a polymer system and introduce a tortuous diffusion path to reduce overall permeability. However, anisotropic arrangement (orientation) of filler nanoparticles can provide additional tortuosity to increase barrier performance. Based on the Bharadwaj model, the relative permeability of a polymer nanocomposite and its corresponding polymer matrix is given by:

$$\frac{P_s}{P_p} = \frac{1 - \phi_s}{1 + \frac{L}{2W} \phi_s \left(\frac{2}{3}\right) \left(S + \frac{1}{2}\right)} \dots\dots\dots(4.5)$$

Where ϕ_s , L and W represent the volume fraction, length and width of the filler materials. S is for Herman's order parameter for the polymer composite. Thus, for a constant volume fraction, the overall permeability is significantly dependent on the nanoparticle alignment in the polymer matrix.

Here we have modified the Bharadwaj model for a one component CNC system. The pure CNC system can be seen as a nanocomposite of CNCs in “free space” where the CNC have an average orientation and can be fitted to the Bharadwaj model. However, a complication is that the chiral nematic, random, and anisotropic systems have different densities. Thus, the packing factor, and resultant permeability should be different as the Bharadwaj model is dependent upon the volume fraction of a nanocomposite. In other words, if the system is seen as a nanocomposite of CNCs in free space, then due to the density differences, the isotropic and anisotropic systems have different effective volume fractions of CNCs. The volume fraction of the anisotropic configuration is calculated from equation 4.6. The density value of chiral nematic and random configurations are

1.45 and 1.50g/cm³ respectively⁴². The packing density (1.65g/cm³) of the anisotropic configuration is higher than the isotropic arrangement⁴². The weight percentage of anisotropic and isotropic configuration is defined as X and Y, respectively. So, the volume fraction of the anisotropic component must be less than the weight percentage of the anisotropic component. The average length and width of the crystalline domains was 100nm and 5nm, respectively (details can be found in the TEM section of the APPENDIX C), for this modified model. It should be noted that isotropic configuration is indistinguishable between chiral nematic and random arrangement for this model. The anisotropic arrangement can have an orthogonal or planar configuration, but the orthogonal configuration cannot be present due to the fabrication process. Hence, the boundary condition for the order parameter should be between 0 – 1, where the isotropic configuration is represented by S=0, and S=1 for the complete anisotropic arrangement. The relative permeability of anisotropic and isotropic cellulose nanocrystal system is given by equation 4.7.

$$\phi_{anisotropic} = \frac{X(m/d_{anisotropic})}{((X(m/d_{anisotropic}) + (Y(m/d_{isotropic})))} \dots\dots\dots(4.6)$$

$$\frac{P_{anisotropic}}{P_{isotropic}} = \frac{1 - \phi_{anisotropic}}{1 + \frac{L}{2W} \phi_{anisotropic} (\frac{2}{3})(S + \frac{1}{2})} \dots\dots\dots(4.7)$$

Where, $\phi_{anisotropic}$, L and W represent the volume fraction of anisotropic phase, length of CNCs and width of CNCs. Based on the fabrication process, only isotropic and anisotropic planar configuration were considered for the barrier properties of the CNC system.

4.3.4 Bharadwaj model for the prediction of gas permeability.

The permeability data for the CNC films with different Herman's order parameter was fitted with our modified Bharadwaj model. It should be noted that isotropic arrangement ($S=0$) can be chiral nematic or random configuration, and the Bharadwaj model did not consider this phenomenon. However, both chiral nematic and random configuration permeability predictions were required to validate our experimental data; the permeability data for the chiral nematic system was acquired experimentally. Since the permeability of the random arrangement is unknown and could not be determined experimentally, a linear regression analysis (based on the anisotropic data) was adopted to determine the random permeability data for the CO₂ and O₂ gas systems (Figure CS2 and CS3 in the APPENDIX C). Relative permeability for different CNC orientations and the corresponding model data is shown in Figure 4.2. In Figure 4.2a, the experimental data set was based on the chiral nematic configuration. It was observed that the relative permeability data deviated from the model data for the order parameter region between 0.2-0.6. Moreover, the deviation was more prominent for O₂ gas compared to the CO₂ system. However, the relative permeability based on a random configuration (Figure 4.2b) was very close to the model data. Surprisingly, experimental data for the CO₂ gas system was perfectly matched with the model data. Different types of gas molecules have different size and polarity. For example, CO₂ is more polar compared to O₂, hence, CNC-CO₂ polar interaction must induce higher solubility, therefore, higher gas permeability compared to O₂ gas molecules¹⁴⁷. However, this model does not consider material-gas molecule interactions which might be a potential reason for the deviation of the experimental data for distinct types of gas molecules.

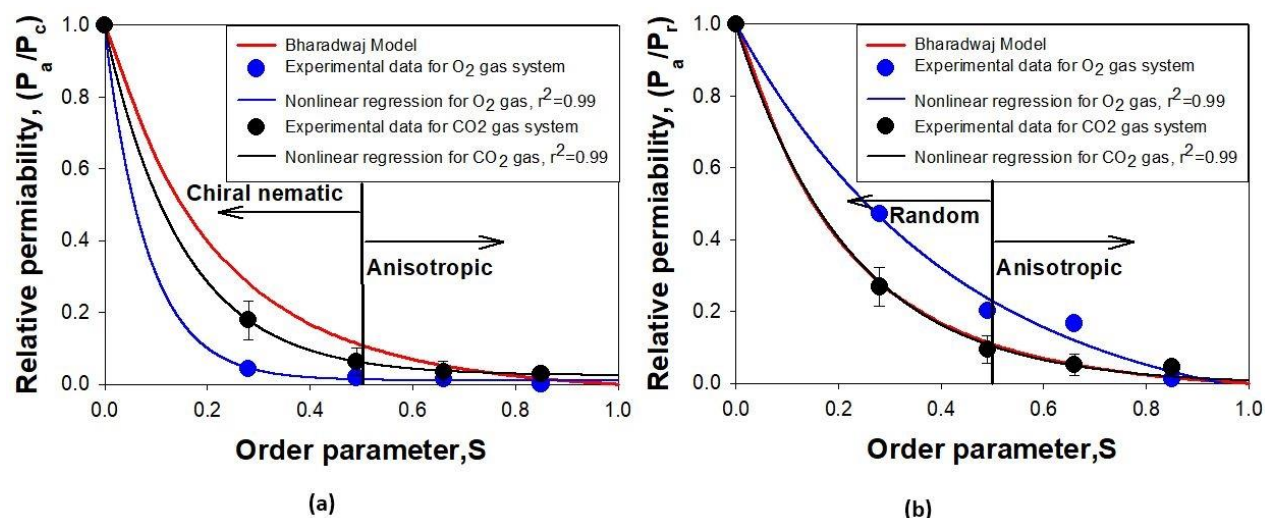


Figure 4.2 Comparison of the modified Bharadwaj model data with experimental data for oxygen and carbon dioxide fit with either (a) chiral nematic as $S=0$ or (b) regression to $S=0$

Based on Figure 4.2, the deviation of the experimental data from the model data was significant for the percentage of the anisotropic region and the types of gas molecules. The deviation was remarkable for the low/moderate region compared to the highly anisotropic region. In the moderate/low order region, the deviation was prominent for the chiral nematic configuration compared to the random arrangement of the liquid crystalline domains. CNC films with low-moderate order parameter ($S=0.3-0.6$) have both isotropic (chiral nematic vs random) and anisotropic domains orientation. But, this model could not differentiate the type of isotropic configuration (the percentage of chiral and random configuration). Moreover, the percentage of chirality and random phase in isotropic arrangement could not be determined with the current characterization technique. The percentage of orientation (chiral nematic vs random) can be controlled by the fabrication process. In general, the chiral nematic configuration is favorable with the slower rate of solvent evaporation, where faster evaporation is for the random arrangement. In this work, the anisotropic coating was prepared using a high-shear force with a faster drying process. So, the low-moderate anisotropic film should have higher random domains compared to

chiral nematic percentage (as a long time is required for chiral nematic arrangement). So, the model prediction based on the random configuration must be closer to the experimental data (Figure 4.2b). In the higher order parameter region, most of the domains must be aligned along the shear direction, hence, the experimental data for relative permeability must follow the model data (both Figure 4.2a and Figure 4.2b). However, the experimental data was slightly higher than the model data. This model considered the permeability of the anisotropic (crystalline) region to be zero which is not true for any experimental condition¹⁵¹. Moreover, CNC films are composed of amorphous, semi-amorphous and crystalline domains³⁸. In the anisotropic configuration, CNC films must have some short-order amorphous domains, which are also aligned with the crystalline domains. However, these short order amorphous domains must have higher permeability compared to the crystalline domains which was ignored by this model. In other words, the Bharadwaj model assumes the nanofiller is perfectly impermeable and intercepts at $P=0$ at volume fraction of 1; thus, our modification dictates that $P=0$ at $S=1$ (as $\Phi_{\text{anisotropic}}$ would also be 1), which as CNC is a polymer, cannot be true (Figure CS2 and CS3 in APPENDIX C). As CNCs are also not 100% crystalline, the amorphous regions should magnify this error at high order parameters. While it would be trivial to modify the model to account for a finite permeability, one would need to know, *a priori* the transport behavior of perfectly aligned CNC films (which we do not), although the values could be estimated by regression. Regardless, further model modification or regression does not seem to be necessary as the modified model fits rather well to the data obtained, due to the extremely small permeability of the anisotropic phase relative to the isotropic phase.

4.3.5 Comparison with other materials

In other works, CNF has typically been shown to have better O₂ and CO₂ barrier performance than CNC¹³⁸. However, the improved barrier property observed in the current work for aligned CNC materials is much higher than previous CNF and CNC studies¹⁴²⁻¹⁴³. As, to our knowledge, the effect of orientation has never been performed for cellulosic nanomaterials, the effect of structural arrangement was never explored, and the improved behavior missed. Additionally, the effect of structural arrangement may play a role in the lack of data consistency observed for the previous studies, where many values of transport have been obtained, although differences in the CNCs themselves may also be responsible¹³⁸. Going forward, the good fit to our modification of the Bharadwaj model can be instructive for improving behavior further. While it can be easily seen that increasing order parameter (*S*) further will lead to large reductions in permeability by increasing the anisotropic fraction and lowering free volume, decreasing the numerator and increasing the denominator simultaneously, it should be pointed out that higher aspect ratio CNCs should also reduce permeability (if anisotropy remains the same).

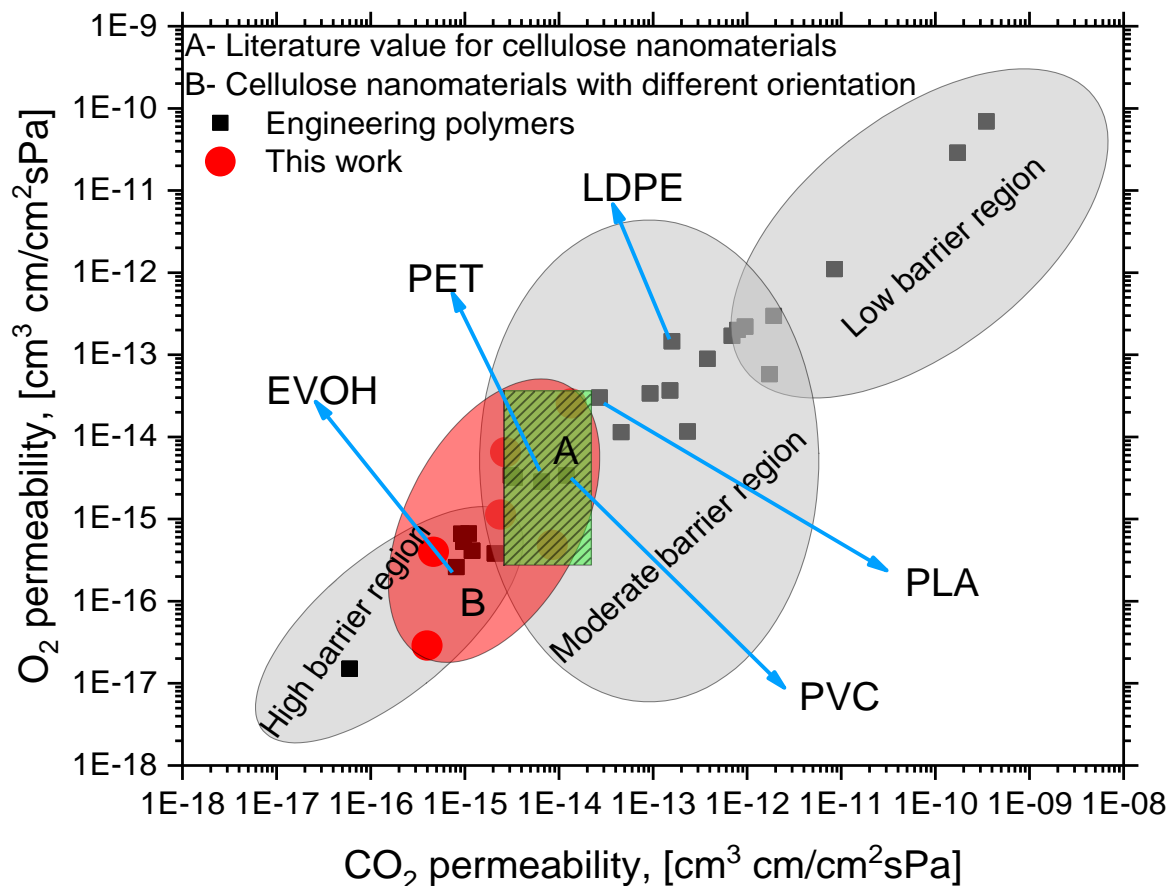


Figure 4.3 Ashby plot of gas permeability response of cellulose films with various structural arrangements with respect to other engineering polymers. Details of quantitative data for this plot can be found in the Appendix C (Table CS1)

Outside of nanocellulose, and more functionally, aligned CNC can have higher barrier performance than traditional packaging materials: 97 and 23-fold higher barrier property for oxygen gas compare to PET (Mylar A) and EVOH, respectively. An Ashby plot (Figure 4.3) for oxygen vs carbon dioxide gas permeability is illustrated for the barrier property of cellulose nanomaterials compare to traditional packaging materials. Thus, longer CNC sources may improve the barrier performance further. Regardless, the relatively high barrier performance of

anisotropic CNC films relative to other, highly utilized materials, along with sustainability, biodegradability, non-toxicity, and transparency may make aligned CNC coatings useful for future high-performance barrier applications. However, CNCs need a controlled structure (anisotropy) to reduce free volume that was limiting their films to fully take advantage of the high polarity and high crystallinity of CNCs relative to other polymers that is necessary for high barrier performance.

4.4 Summary

For the first time, an in-depth study of the structure-property relationships of nanocellulose films was investigated for O₂ and CO₂ permeability. High orientation of CNC films was found to be critical to achieving the highest barrier performance; a 900-fold increase in O₂ permeability was observed between the isotropic and anisotropic films. The Bharadwaj model of gas permeability was modified and applied to the CNC experimental system. There was overall agreement with the model, which suggests that CNC permeability is highly dependent upon packing factor, and therefore should be dependent upon degree of anisotropy. Overall, we show that in addition to outperforming CNFs, the O₂ and CO₂ permeability for highly oriented CNCs can exceed the performance of traditional barrier materials due to their exceedingly high polarity and crystallinity. As CNCs are renewably sourced, non-toxic, biodegradable and transparent, such materials may have utility for future barrier materials.

CHAPTER 5. SUPERIOR, PROCESSING-DEPENDENT THERMAL CONDUCTIVITY OF CELLULOSE NANOCRYSTAL-POLY(VINYL ALCOHOL) COMPOSITE FILMS

All lab work except thermal conductivity measurement, and modeling work was performed by Reaz Chowdhury. All analysis except effective medium theory was performed by Reaz Chowdhury with guidance by Prof. Jeffrey P. Youngblood. All writing except thermal conductivity measurement and Choy & Young model sections was performed by Reaz Chowdhury with guidance and editing by Prof. Jeffrey P. Youngblood and Prof. Arden L. Moore.

The following chapter contains content reproduced with permission from R. A. Chowdhury, A. Rai, E. Glynn, P. Morgan, A. L. Moore, and J. P. Youngblood, "Superior, processing-dependent thermal conductivity of cellulose Nanocrystal-Poly (vinyl alcohol) composite films," *Polymer*, vol. 164, pp. 17-25, 2019. Copyright 2019 Elsevier Ltd.

5.1 Introduction

Thermal management has become a critical issue for electronic devices due to the increased power densities and an increasing reliance on polymeric packaging materials. In traditional rigid electronics, electrically insulating polymers are extensively used as printed circuit boards (PCBs), device holders, or thermal interface materials (TIMs) due to the ease of processability, low cost, and low density compared to other materials¹⁵²⁻¹⁵³. Typical thermal conductivity (κ) values for neat, amorphous polymers are very low (typically $0.1\text{-}0.3 \text{ W m}^{-1} \text{ K}^{-1}$), which causes a major bottleneck in terms of thermal management¹⁵²⁻¹⁵⁴. Recently, there has been growing interest towards flexible electronics because of their potential applications in sensors, displays, energy harvesting, and electronic skins for robotics¹⁵⁵. Flexible electronics also face issues of thermal management as the entire supporting substrate is usually comprised of a low κ material. In traditional electronics, plastic-based materials such as polyethylene terephthalate (PET), polyethylene naphthalate (PEN), and polyimide (PI) are popular materials for such applications since they are mechanically strong, chemically stable, optically transparent, easy to fabricate and

have industrial-scale production capability through roll-to-roll printing methods¹³⁷. However, these petroleum-based materials are environmentally less attractive from a life-cycle point-of-view¹⁵⁶ and have low κ of $\sim 0.15\text{-}0.3 \text{ W m}^{-1} \text{ K}^{-1}$ at ambient conditions similar to those used in traditional electronics packaging¹⁵⁷⁻¹⁵⁹. For materials with low κ , even modest power densities can lead to overheating and, ultimately, permanent damage to the device¹⁶⁰. Overheating in electronics in general has been cited as a major factor in $\sim 55\%$ of electronic equipment failures which are attributed to malfunction, PCB board failure, or short circuit¹⁶¹⁻¹⁶².

To improve the κ of polymers used in electronics packaging, several types of inorganic fillers such as boron nitride (BN), metal nitride, metallic nanowires, carbon materials, metal oxide or clay have been used in the polymer matrix^{152, 163-167}. However, the addition of such fillers may sacrifice other important polymer properties like low density, processability, or electrical insulation. For example, carbon nanotubes (CNTs) have extremely high κ , but their application in polymer nanocomposites is limited due to the presence of high interfacial resistance (between nanotube and matrix) and high contact resistance (between nanotubes)¹⁶⁴. Graphene or graphite nanoplatelets in a polymer matrix can overcome the interfacial resistance issue and exhibit superior κ but at the expense of sacrificing electrical insulation¹⁶⁸⁻¹⁷⁰. In terms of processability, while including a greater percentage of particulates can increase composite κ , it also has a strong effect on viscosity which may make integration into electronics packaging impossible¹⁷¹. Due to the above circumstances, different research groups are looking for new substrate materials that are environmentally friendly, highly flexible, and at the same time thermally conductive in order to alleviate local heating from the flexible electronic devices.

Cellulose-based materials are considered to be potential candidates as eco-friendly substrate materials of flexible electronic devices with the capability of resolving thermal management

issues¹⁷². Cellulose derivatives are attractive bio-materials regarding environmental (low toxic, low carbon footprint, and biodegradable) and economical (abundant, renewable, and easily recyclable) concerns⁵. In addition, the low coefficient of thermal expansion and high mechanical strength of such materials show their potential for next-generation flexible electronic device substrates. However, few studies have been previously reported regarding the thermal properties of cellulose-based materials for their applications as substrates for flexible electronic devices. Shimazaki et al. created a highly thermally conductive cellulose nanofiber/epoxy resin nanocomposite with a κ of $\sim 1.1 \text{ W m}^{-1} \text{ K}^{-1}$, which was nearly seven times higher than that of the neat epoxy matrix ($0.15 \text{ W m}^{-1} \text{ K}^{-1}$)¹⁷³. Such a high value of κ was attributed to the crystalline nature of cellulose nanofibers that provide excellent phonon pathways through the nanocomposite. Uetani et al. observed in-plane κ values as high as $\sim 2.5 \text{ W m}^{-1} \text{ K}^{-1}$ for tunicate nanowhiskers (TNWs), which was about eight times higher than in the thickness direction due to the fiber orientation in heat flow direction¹⁷². In another study, Uetani et al. reported the in-plane κ value as high as $\sim 2.5 \text{ W m}^{-1} \text{ K}^{-1}$ for nanocellulose (NC)-acrylic resin composite, which was more than three times higher than the κ of the neat acrylic resin ($\sim 0.76 \text{ W m}^{-1} \text{ K}^{-1}$)¹⁷⁴. This value is roughly an order of magnitude higher than those of the plastic films that are currently used for flexible electronics substrates, and hence shows the potential of cellulose-based materials for use as the substrate to efficiently cool the next generation flexible electronic devices.

Of the various forms of cellulose, cellulose nanocrystals (CNCs) are intriguing from an engineering materials perspective. CNCs are rod-like anisotropic nanoparticles that possess a unique set of properties such as low density, high specific strength, optical transparency, and electrical insulation⁵. The material properties (mechanical, thermal, electrical, and optical) of CNC-based materials can be controlled with the structural arrangement of the crystalline

domains^{34, 38-39}. However, the organization of crystalline anisotropic domains within a CNC-based material is strongly influenced by the processing history, with the final arrangement being isotropic, chiral nematic, or anisotropic¹⁷⁵. Experimentally, chiral nematic and anisotropic transverse directions show four-fold lower κ compared to in the anisotropic longitudinal (aligned) direction²⁵. Based on this current understanding of the processing-structure-property relationship within CNC-based films, increased packing density with strong interfacial interaction are expected to be effective routes to enhancing the κ of CNC-based materials, which may act as an alternative for flexible electronic substrates to resolve the issue of thermal management.

Previous work(s) have examined the structure-property relationship for CNC-only films, with interstitial spaces between CNCs representing void space. Filling the void space with a compatible polymer with lower interfacial resistance should increase the κ by providing additional paths for phonon propagation between crystallites. In this context, PVA can be an excellent candidate to be a binding agent as it is a waterborne polymer with an abundance of hydroxyl moieties that can form relatively strong hydrogen bonds to form a stable network structure among CNCs. In this work, we create CNC-PVA composite films of varying internal structure and examine how processing affects the CNC ordering and, thus, the films' κ magnitude and directional dependence. Isotropic and anisotropic structural arrangements of CNCs in the composite films were prepared for various CNC:PVA ratios that governed the phonon scattering by controlling the available free volume in the composite films. The in-plane κ of the CNC-PVA composite films were determined using a modified steady-state bridge method. A combination of experimentation and modeling was used to study the effects of addition of PVA on the effective κ of the CNC-based films and the interfacial thermal resistance.

5.2 Experimental

5.2.1 CNC Film Preparation and CNC Alignment Characterization

Never-dried, pristine CNC aqueous suspension (12.2wt%, batch no-2015-FPL-071CNC) with 1% sulfur and sodium counterion was purchased from the University of Maine (Orono, ME, USA) and manufactured by the USDA, US Forest Service-Forest Products Laboratory. Poly(vinyl alcohol) (PVA) with different molecular weights were purchased from Sigma-Aldrich. Different properties such as molecular weight, crystallinity index and hydrolysis information for PVA can be found in APPENDIX D. All materials were used as received without any modification.

5.2.1.1 Film fabrication:

CNC-PVA composite with random/chiral nematic configuration was prepared from compositions as shown in APPENDIX D, Table DS1. Briefly, a 20ml solution was poured in a polystyrene Petri dish and slow evaporation (several days) at room temperature was utilized for the film fabrication. Two different approaches were used for oriented film fabrication. Anisotropic CNC films were prepared with a method reported by Reising et al. where about 300 S^{-1} shear rate was applied for shear alignment³⁴. Samples were dried at room temperature for several days. Finally, anisotropic CNC-PVA composites was prepared by Roll-to-Roll microgravure coating where details of the procedure can be found in the literature^{69, 176}. Here, PET was used as a flexible substrate and the overall fabrication was performed at a 32 rpm microgravure rotation with 0.63m/min substrate speed. The drying oven temperature was 85°C and the completely dried coated film was received in the rewinder.

5.2.1.2 Orientation measurement:

A conventional UV-Vis spectrophotometer (spectra max Plus384, molecular devices Corp., Sunnyvale, CA) was used for the order parameter measurement. A similar method described by

Chowdhury et al. was used for this characterization and details can be found there³⁸. Briefly, a 12mmX25mm free standing sample was placed between a cross polarizer and the transmittance data was measured for 45° and 90° configuration. The transmitted signal was measured from 400-750 nm wavelength. The following equations were utilized for the order parameter (S) calculation:

$$I = I_0 \sin^2 2\theta \sin^2 \left(\frac{\pi \Delta n d}{\lambda} \right) \dots \dots \dots (5.1)$$

So

$$\frac{I_{45}}{I_{90}} = \frac{I_0 \sin^2 (2 * 45) \sin^2 \left(\frac{\pi \Delta n d}{\lambda} \right)}{I_0 \sin^2 (2 * 90) \sin^2 \left(\frac{\pi \Delta n d}{\lambda} \right)}$$

Hence,

$$\frac{I_{45}}{I_{90}} = D^* = D.g = \frac{(2S + 1)}{(1 - S)} \dots \dots \dots (5.2)$$

Here, I_0 , θ , Δn , d , λ , I , g and D represents amplitude of incident light, sample position with respect of polarizer, refractive index difference, sample thickness, wavelength of incident light, transmitted light intensity, correction factor and dichroic ratio, respectively. As the refractive index difference for ordinary light and extraordinary light is insignificant, $g=1$ was used for the calculation. Finally, the order parameter for any material is between 0-1 where, $S=0$ defined as random/ isotropic configuration and $S=1$ is for perfect anisotropic configuration.

5.2.2 Phase morphology of the composite films

A Carl Zeiss (Axio observer A1) inverted polarized light microscopy in transmission mode was used for the characterization of phase morphology for CNC and PVA components. Briefly, samples were 45° and 90° position with respect to the plane of polarized light. It should be noted that the samples at 45° and 90° position formed bright field, and dark field illumination, respectively. The fracture surface of the composite films was observed by a scanning electron

microscopy (SEM, ProX, Phenom). Before imagining, a thin layer of gold coating was sputtered on the samples.

5.2.3 Thermal conductivity measurement

The in-plane κ of the CNC films near room temperature were measured using a modified steady-state bridge method similar to the one employed by Benford et al. to measure κ of free-standing tape/thin films¹⁷⁷. An annotated 3D illustration of the measurement stage used in this work is given in Figure 5.1. The measurement stage consists of two identical platforms, each of which is comprised of a 25 mm x 7 mm x 1 mm copper (Cu) plate, backside serpentine Nichrome wire heater, PFA-insulated 0.127 mm diameter Type J thermocouple, and a 20 mm long 2 mm diameter threaded Nylon support. Each Nylon platform support is anchored to an adjustable stainless-steel base with thermal mass much larger than that of the platforms. During measurements, electrical power is supplied to one of the platforms via 15 cm long, 0.255 mm diameter insulated lead wires (2 per platform) that attach to the Nichrome heater at the copper plate. This localizes Joule heating to the Nichrome wire heater that is in direct contact with the copper plate, while also minimizing parasitic heat conduction along the leads. It should be noted that both platforms are identical for the sake of the thermal circuit analysis used to determine κ , but that only one Nichrome heater is powered during a given experiment.

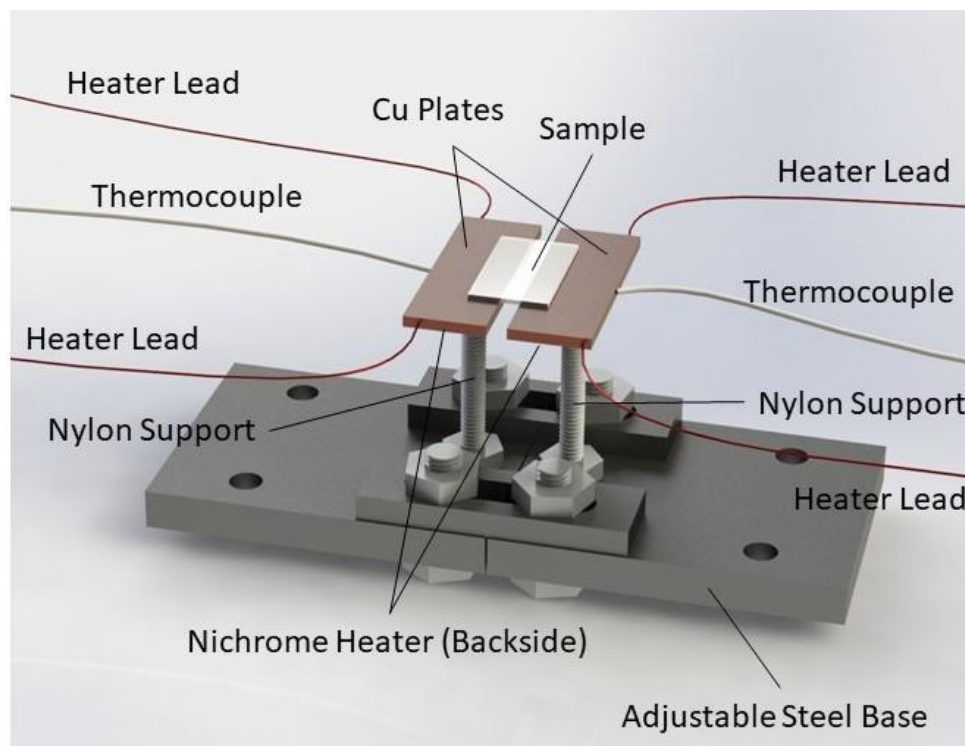


Figure 5.1 Annotated 3D drawing of the measurement stage. Silver paint for affixing the sample not shown

For sample preparation and mounting, rectangular sections 3-5 mm in width and up to 25 mm in length were first cut from the CNC film under study. For anisotropic films, this was done either perpendicular or parallel to the direction of crystal alignment. When possible, multiple sections of sample were stacked together to increase signal strength relative to background. Samples were affixed on either end to the Cu plates using a vacuum-compatible high conductivity silver paint (SPI Supplies). This left a segment of clean film sample with known length, width, and total thickness suspended between the two copper plates as shown in the Figure 5.1. The entire stage assembly was then loaded into a vacuum chamber and pumped down to $\sim 10^{-6}$ Torr via mechanically-backed turbo pump to minimize convection heat transfer. Electrical power and thermocouple lead extended across the chamber walls via a vacuum-compatible feedthrough.

Once the vacuum was stabilized, κ measurements could begin by inducing Joule heating in one of the Nichrome heaters via a precision DC power supply. This raised the temperature of the corresponding Cu platform, with heat being conducted along the suspended length of the sample as through the support and leads. The setup allows for measurement of the Joule heating in the Nichrome heater as well as the temperature of each Cu platform, from which the κ of the film sample can be determined via conduction analysis of the setup's thermal circuit as described in our previous work²⁵. To reduce measurement uncertainty, steady-state temperature differences were measured at multiple Joule heating powers for each sample and the observed linear trend of temperature difference versus heat conducted through the sample used to determine the sample's thermal resistance. Heat conduction through residual air within the chamber was accounted for by performing the measurement without a sample present to obtain the "background" thermal conductance and subtracting this from the thermal conductance values obtained with a sample present. The total measured thermal conductance was found to be at least 2X this background thermal conductance for all samples. The major source of experimental uncertainty stems from the inherent accuracy of two thermocouples (± 1.1 °C). When this inherent accuracy for a single thermocouple is propagated forward to measuring a temperature difference with two identical thermocouples, the uncertainty in the temperature difference becomes ± 1.6 °C. For context, during a typical measurement the maximum temperature difference between the heating and sensing platforms was generally ~ 10 - 13 °C. The use of the linear slope method described above involving multiple data points helps reduce the magnitude of this error, although it still dominates those associated with sample geometry, applied Joule heating, and parasitic heat losses. When considering all of these sources of error and using standard error propagation for both measurements (background and with sample present), an upper limit of ± 19.2 % measurement

uncertainty in thermal conductivity is associated with the results presented in this work. For future work, the overall measurement uncertainty could be significantly improved through the use of alternative temperature measurement methods which offer superior accuracy, such as well-calibrated silicon diodes.

5.3 Results and discussion

5.3.1 Effect of (CNC: PVA) composition with isotropic configuration

The κ of any polymer nanocomposite system depends on aspects of its internal structure such as nanofiller percentage, aspect ratio of nanofiller, nanofiller orientation, and the matrix-filler interaction, which collectively also determine the free volume (as an active defect site) of polymer segments; in short, how the structure affects phonon propagation and scattering within the material¹⁵². Figure 5.2 and 5.3 present the measured κ of CNC-PVA composite films with differing CNC to PVA ratios made with 124-186K and 89-98K PVA molecular weight, respectively. As structure of the nanocomposite can be affected by fluidity of the solution during drying, the effect of dilution factor on κ was investigated for three different initial concentrations (from dilute to concentrated solution). For both figures, increasing CNC percentage generally leads to higher κ compared to neat PVA (0% CNC) results. The long-chain PVA showed very low κ likely due to the presence of entanglements with a globular structure, which provide additional free volume; hence, higher phonon scattering. Bulk PVA films with different concentration and molecular weight showed κ between 0.1-0.4 W m⁻¹ K⁻¹. The long chain PVA molecules formed globule structure in the aqueous suspension and the hydrodynamic radius of the globule structure must be larger for the higher molecular weight PVA. At the time of the drying, the viscosity of the aqueous suspension must increase with time and the globule structure of PVA molecules must form a

favorable packing. PVA films with higher packing density should have higher thermal conductivity compared to lower packing density, which are the major reason for the variable thermal conductivity. However, the values obtained are within the range expected for such polymers. Bulk CNC films (100 % CNC) with different initial concentration showed variable κ , with the best results obtained for initial concentrations above 1 %. It is well known that, never-dried CNC suspensions can possess chiral nematic configuration which is strongly concentration dependent¹⁷⁸⁻¹⁷⁹. Higher concentration CNC suspensions may not have well organized chiral nematic structure due to frustrated ordering, so can instead be highly defected and nearly random while dilute CNC suspensions may have an organized chiral nematic configuration. However, a chiral nematic structure may have more free volume in the system that will be responsible for phonon scattering and therefore a low κ as was observed in this work. Moreover, CNCs are in a random configuration in the transverse and longitudinal direction due to the generally isotropic (or orthotropic) arrangement. The phase morphology for isotropic CNC-PVA films can be found in the APPENDIX D. Thus, the results given in Figures 5.2 and 5.3 represent values associated with a generally isotropic CNC orientation within the in-plane direction.

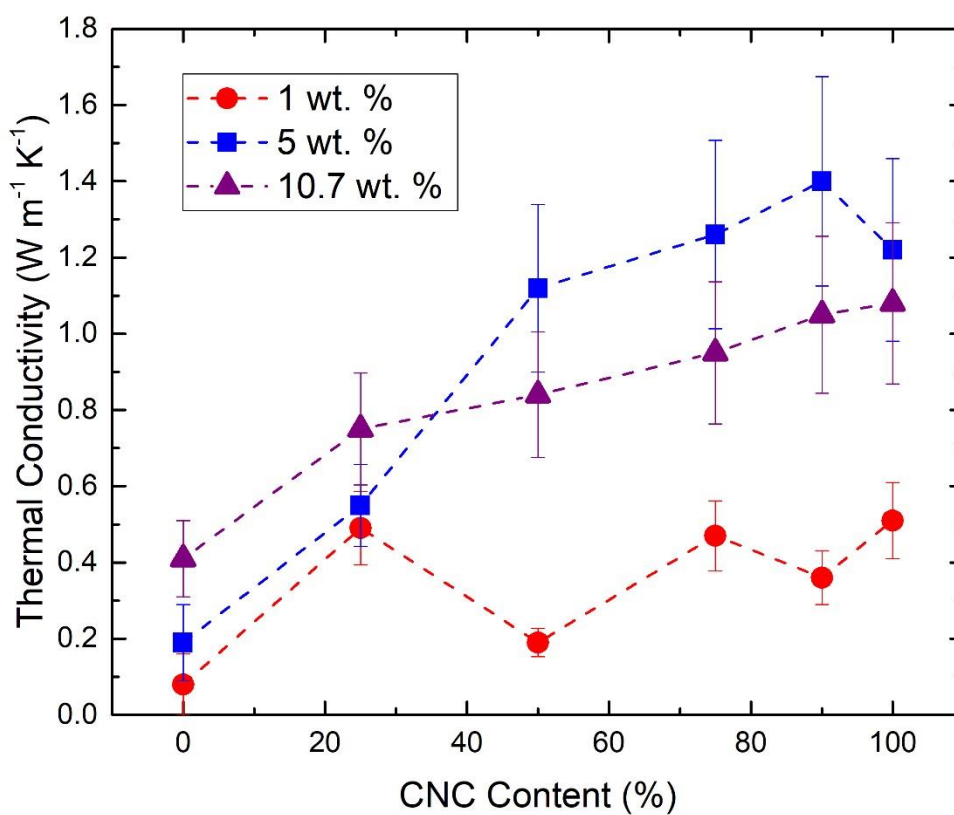


Figure 5.2 Thermal conductivity of un-sheared CNC:PVA films versus CNC content of final film. Data shown is for 1, 5, and 10.7 initial CNC and PVA weight percent used during fabrication. The PVA molecular weight was 124-186K

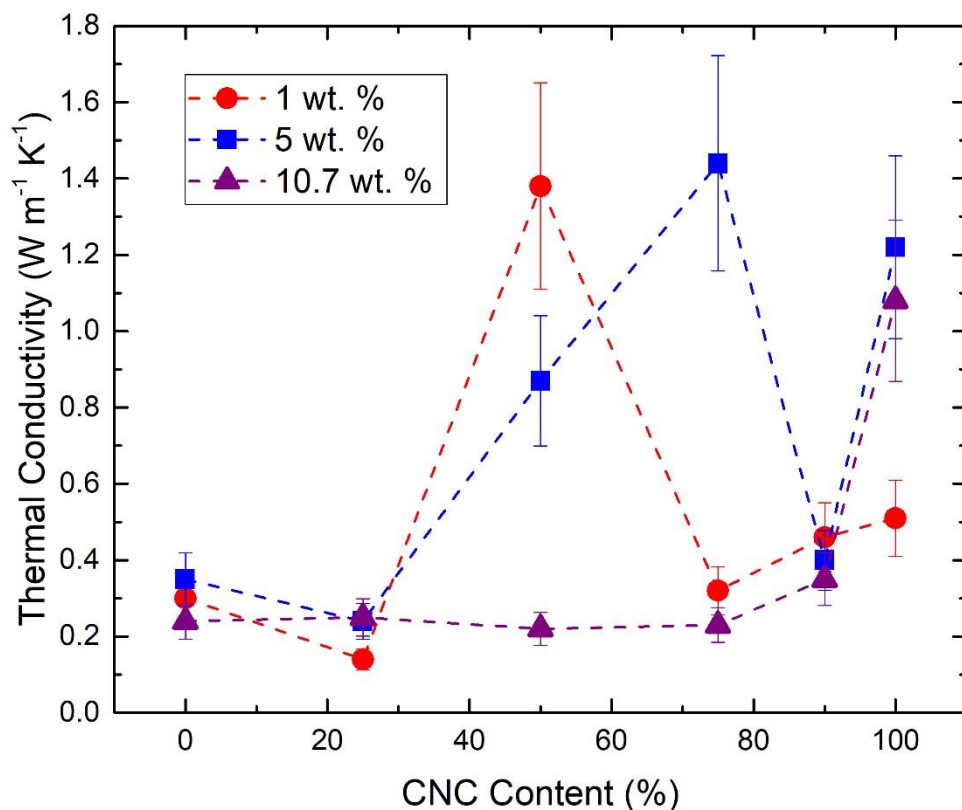


Figure 5.3 Thermal conductivity of un-sheared CNC:PVA films versus CNC content of final film. Data shown is for 1, 5, and 10.7 initial CNC and PVA weight percent used during fabrication. The PVA molecular weight was 89-98K

With the addition of PVA in the CNC suspension with different concentrations, the resulting films can have random or chiral nematic structure, which is determined by the initial concentration of nanocomposite aqueous suspension, PVA molecular weight and PVA solid loading (Table DS1 in APPENDIX D). The κ for CNC-PVA composites were very different than expected. Pure CNC film showed significantly higher κ (at least 2 to 6-fold) compared to neat PVA films and was concentration dependent. However, this binary composite system did not follow a general rule of mixtures. It was observed that PVA (Mw: 124-186K) solid loading between 10-25 wt% showed

an improved κ for CNC-PVA composites. Results for the lower molecular weight PVA (Mw: 89-98K) are more complex, showing an increase in the κ with PVA solid loading between 25-50 wt% that also depended on the initial solution concentration.

Based on the experimental evidence, it can be deduced that a maximum κ can be observed at the higher CNC solid loading region where PVA molecules can act as a binder or interstitial filler between the CNCs. The addition of PVA must therefore reduce the effective interfacial thermal resistance for this binary composite system compared to the pristine CNC materials (Figure 5.4). The effect of PVA for the reduction of interfacial resistance has been discussed in APPENDIX D. PVA molecules contain hydroxyl groups which can form hydrogen bonds with the CNCs, which are relatively strong and therefore have low interfacial resistance. Further, by filling the voids between CNCs, which would otherwise be air, the PVA helps form a continuous thermal network. As in percolation theory, PVA solid loading should be in an optimum percentage to form a homogeneous network structure for this improved κ ¹⁸⁰. However, the data suggests that PVA loading is dependent on the CNC organization and the molecular weight of the PVA.

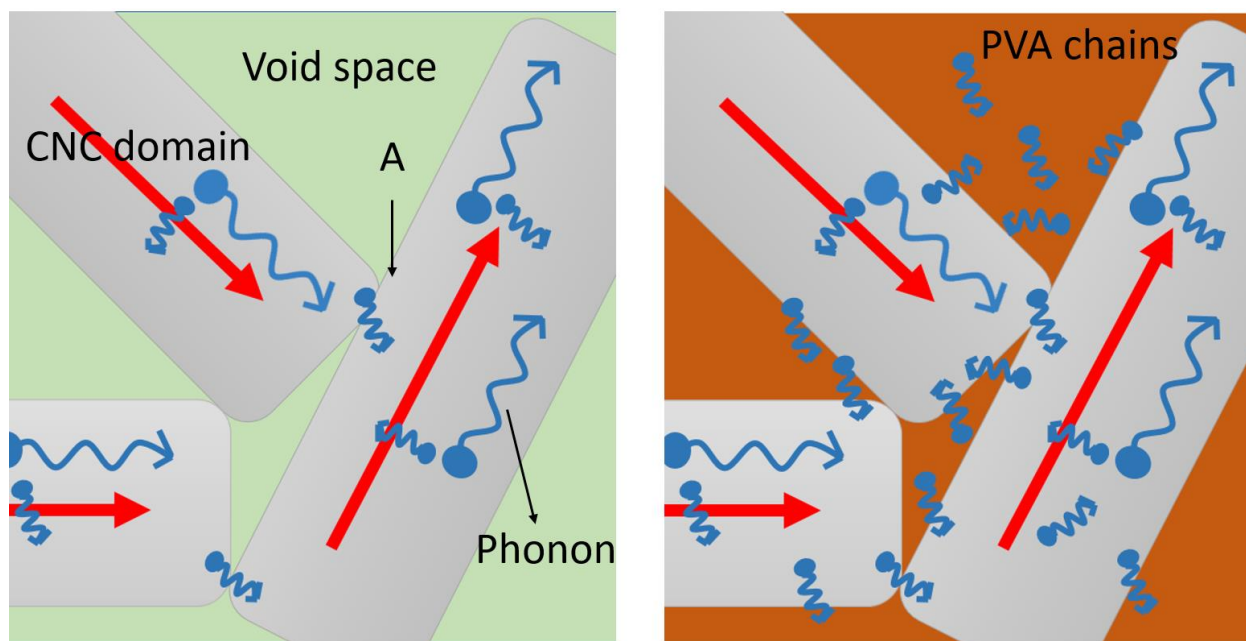


Figure 5.4 Effect of PVA for reducing the interfacial resistance between CNC domains. Here, point A is showed for interfacial contact position where phonon can diffuse from one crystal to another crystal. (red arrow sign is denoted for the sum of every phonon vector projection in the chain direction of individual crystalline domain)

5.3.2 Effect of anisotropy for different (CNC: PVA) composition

Due to the anisotropy of the crystalline directions of individual CNCs, they transmit thermal energy differently in each (longitudinal and transverse) direction relative to its primary axis. Therefore, the κ for bulk CNC film should depend on the CNC crystalline organization and likewise be anisotropic in films with anisotropic organization/orientation. As predicted, an anisotropic arrangement is shown to have a significant increase in the κ for CNC-PVA nanocomposite system (Figure 5.5). An analysis of variance (ANOVA) study using Tukey's approach of multiple pairwise comparisons was conducted at 95 % confidence level for the data plotted in Figure 5.5. The outcome of this comparison was that statistically significant differences existed between CNC:PVA (75:25) results and those of all other sample types. A statistically significant difference was also determined to exist between results for CNC:PVA (90:10) and the

two lowest CNC content sample types, specifically CNC:PVA (10:90) and CNC:PVA (25:75). All other inter-sample statistical comparisons did not reveal statistically significant differences.

Solution casting methods based on roll-to-roll processing were used for this fabrication, and no significant alignment (i.e. order parameter $S \sim 0$) was observed for PVA solid loading higher than 50 wt%. PVA long chain molecules in aqueous suspension have a globular structure with many entanglements. The applied shear is insufficient to align it in the shear direction¹⁷⁶. When PVA loading is less than 25 wt%, however, it is possible for it to be entrapped between CNC domains. In this case, the film anisotropy is dominated by CNC liquid crystallinity. Hence, anisotropy was observed for CNC-PVA composite coatings with CNC loading higher than 50 wt%. The phase morphology for a typical anisotropic CNC-PVA composite film can be found in APPENDIX D.

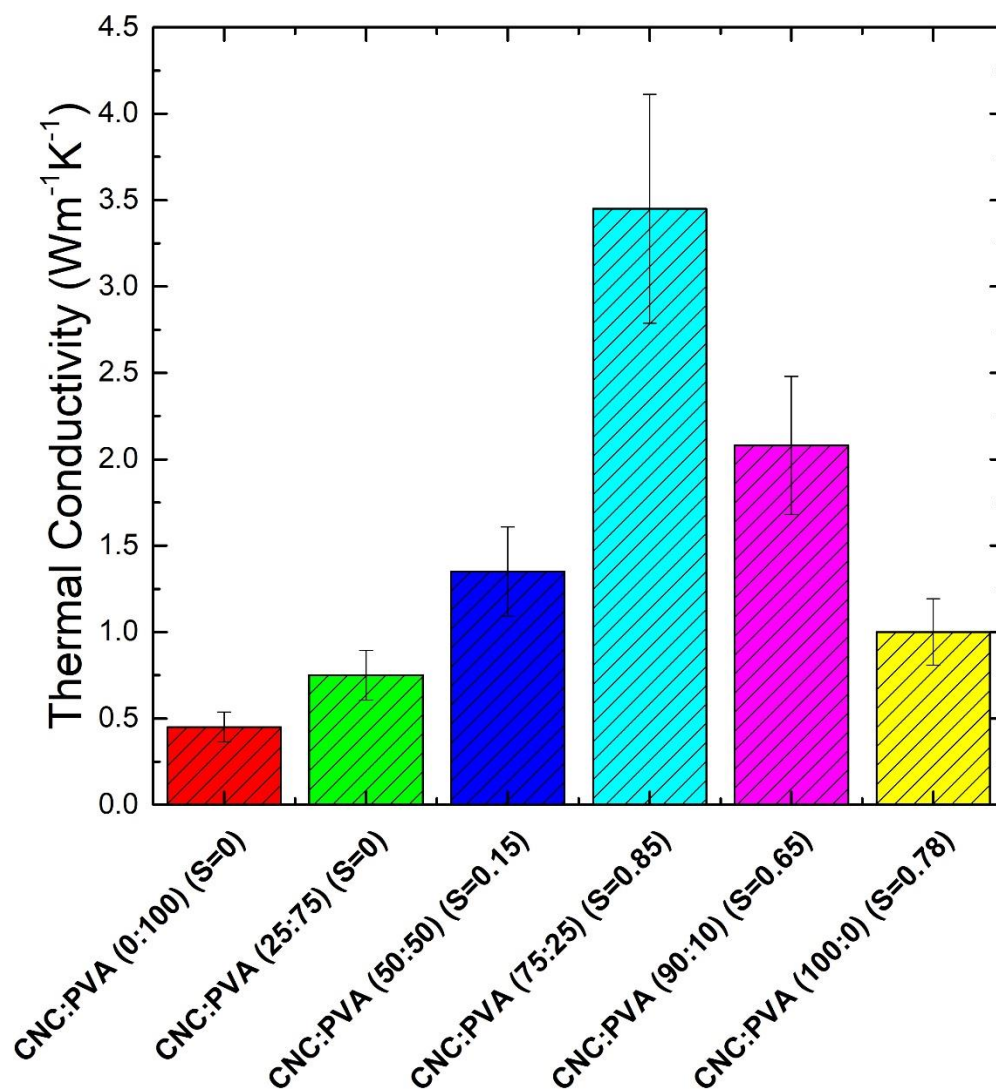


Figure 5.5 In-plane thermal conductivity in the direction of shear of CNC-PVA nanocomposites with various degrees of orientation. S is Hermans order parameter for CNC-PVA nanocomposite system

CNC-PVA composite films with anisotropic configurations demonstrated higher κ compared to the corresponding isotropic configuration, but only along the directions of alignment and was highly dependent on the degree of ordering, i.e. the order parameter S . Experimentally, films with an anisotropic arrangement of CNC-PVA (75:25) composition showed 2.5 times improvement in thermal conductivity along the shear direction compared to films with an isotropic configuration

with the same composition. Maximum orientation was observed for this composition ratio, which is the prime reason for the exceptionally high observed κ . Unlike Figure 5.4, individual CNCs are aligned uniaxially (along the shear direction) which allows phonon propagation down the highest κ direction of the CNC (Figure 5.6). Moreover, aligning the CNCs allows more interfacial contact between the CNCs for higher phonon transport across the interface (details can be found in APPENDIX D). As in the isotropic case, the interfacial resistance between two CNCs is reduced by the PVA filling of the void space and the high bond strength of the PVA molecules. As mentioned before, the PVA percentage should have an optimum percentage with CNC (based on percolation theory) that can act as binder for CNC domains¹⁸⁰. Other CNC-PVA compositions showed moderate to very low anisotropy, hence, the improvement of κ along the shear direction would not be expected to as high.

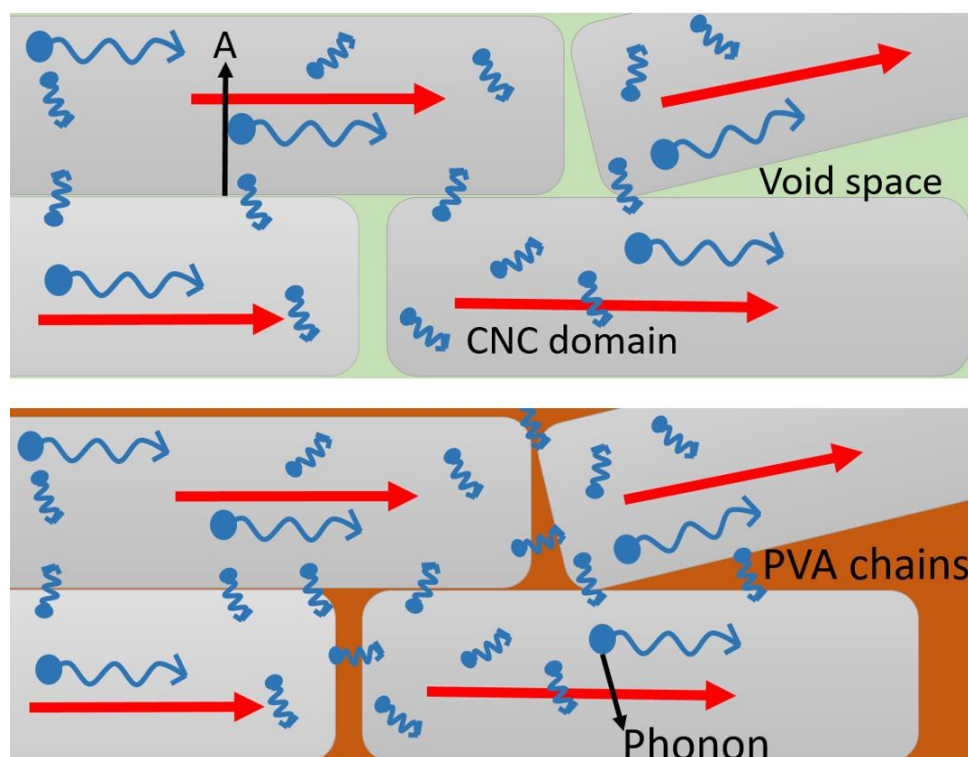


Figure 5.6 Effect of PVA for reducing the interfacial resistance between CNCs for anisotropic composites. Here, point A is shown for the interfacial contact position where phonons can diffuse from one crystal to another crystal. (red arrow sign is denoted for the sum of every phonon vector projection in the chain direction of individual crystalline domain)

It is also worth mentioning that κ reported here is much higher than the traditionally used electrically insulating polymers and associated nanocomposite systems. A comparative data with different polymer systems has been shown in Table 5-1.

Table 5-1 Thermal conductivity for different polymer/polymer nanocomposite systems

Sample	Matrix (wt%)	Filler (wt%)	S	κ	References
PPS-BN	PPS-(70)	BN-(30)	-----	0.62	165
Epoxy-graphite	Epoxy-(76)	Graphite-(24)	-----	1.8	181
Epoxy-CNF	Epoxy	CNF	-----	0.35	181
HDPE-Al	HDPE-(80)	Al- (20)	-----	0.7-1.25	152
Common Engineering thermoplastic	Polymer as matrix	No filler	-----	0.11-0.53	152
PMMA-CNT	PMMA-(96)	CNT- (4)	-----	3.4	164
Acrylic resin-NC	Acrylic resin	NC	-----	2.5	174
TNW	TNW	-----	-----	2.5	163
PI	PI	-----	-----	0.91	163
PET	PET	-----	-----	0.87	163
COP	COP	-----	-----	0.70	163
PPS	PPS	-----	-----	0.63	163
PA	PA	-----	-----	0.25	163
PES	PES	-----	-----	0.25	163
CNC-PVA	CNC	PVA	0	1.4 (maximum)	This work
CNC-PVA	PVA	CNC	0	0.7 (maximum)	This work
CNC-PVA	CNC	PVA	0.85-0.65	3.5 (maximum)	This work

PPS = Polyphenylene sulfide; CNF = Cellulose nanofiber; HDPE = High-density polyethylene; PMMA= Poly(methyl methacrylate); TNW = Tunicate nanowhisker; NC = Nanocellulose; COP = Cyclo-olefin polymer; PA = Polyamide; PES = Polyethesulfone.

5.3.3 Effective Medium Theory – Choy & Young (EMT-CY) Model applied to CNC-PVA composite thin films

For any polymer nanocomposite, the interfacial thermal resistance (ITR) between the fillers and between the filler and matrix plays a significant role in the overall thermal transport. For structured materials, anisotropy also plays a central role, as is the case here. Different models are available to describe complex nanostructured materials¹⁸², polycrystalline structures¹⁸³, and composites¹⁸⁴ where the interfaces and the organization of the materials are factors that dominate the thermal properties. Choy and Young¹⁸⁵ developed a model with an adaptation of Maxwell's

effective medium theory¹⁸⁶ (denoted EMT-CY here), which has been previously applied to study the change in the κ of oriented semi-crystalline polymers¹⁸⁷⁻¹⁸⁹ both along and normal to the orientation direction as a function of the orientation direction crystallinity.

The expressions derived from the EMT-CY model for the CNC-PVA nanocomposites are

$$\frac{\kappa_c - \kappa_m}{\kappa_c + 2\kappa_m} = x \left[\frac{2}{3} \left(\frac{\lambda_{\perp} - 1}{\lambda_{\perp} + 2} \right) + \frac{1}{3} \left(\frac{\lambda_{\parallel} - 1}{\lambda_{\parallel} + 2} \right) \right] \dots\dots\dots (5.3)$$

$$\frac{\kappa_{\perp} - \kappa_m}{\kappa_{\perp} + 2\kappa_m} = x \left[\left(\frac{\lambda_{\perp} - 1}{\lambda_{\perp} + 2} \right) \left(\frac{1 + \langle \cos^2 \gamma \rangle}{2} \right) + \left(\frac{\lambda_{\parallel} - 1}{\lambda_{\parallel} + 2} \right) \frac{\langle \sin^2 \gamma \rangle}{2} \right] \dots\dots\dots (5.4)$$

$$\frac{\kappa_{\parallel} - \kappa_m}{\kappa_{\parallel} + 2\kappa_m} = x \left[\left(\frac{\lambda_{\perp} - 1}{\lambda_{\perp} + 2} \right) \langle \sin^2 \gamma \rangle + \left(\frac{\lambda_{\parallel} - 1}{\lambda_{\parallel} + 2} \right) \langle \cos^2 \gamma \rangle \right] \dots\dots\dots (5.5)$$

$$\lambda_{\perp} = \frac{\kappa_{c\perp}}{\kappa_m} \dots\dots\dots (5.6)$$

$$\lambda_{\parallel} = \frac{\kappa_{c\parallel}}{\kappa_m} \dots\dots\dots (5.7)$$

$$S = \frac{3\langle \cos^2 \gamma \rangle - 1}{2} \dots\dots\dots (5.8)$$

Where x is the weight fraction of the CNC, which is approximately 0.75 for the samples under study²⁵ (details about selection of the value of x can be found in APPENDIX D), and κ_c is the thermal conductivity of an isotropic film which is approximated as $1.22 \text{ W m}^{-1} \text{ K}^{-1}$ from our measurement results presented previously in this work. The effective matrix thermal conductivity κ_m is obtained by solving Equations 5.3, 5.6, and 5.7 simultaneously. Equations (5.4) and (5.5) are used to calculate the macroscopic κ of the CNC-PVA composite films in the directions parallel (κ_{\parallel}) and perpendicular (κ_{\perp}) to the shear direction. The orientation angle of the crystals with respect to the shear direction is represented by γ , while $\kappa_{c\parallel}$ and $\kappa_{c\perp}$ represent the thermal conductivities of a single CNC in the axial and the transverse crystalline directions respectively

and their corresponding values were predicted to be $\sim 5.7 \text{ W m}^{-1} \text{ K}^{-1}$ and $\sim 0.72 \text{ W m}^{-1} \text{ K}^{-1}$ by Diaz et. al.²⁵.

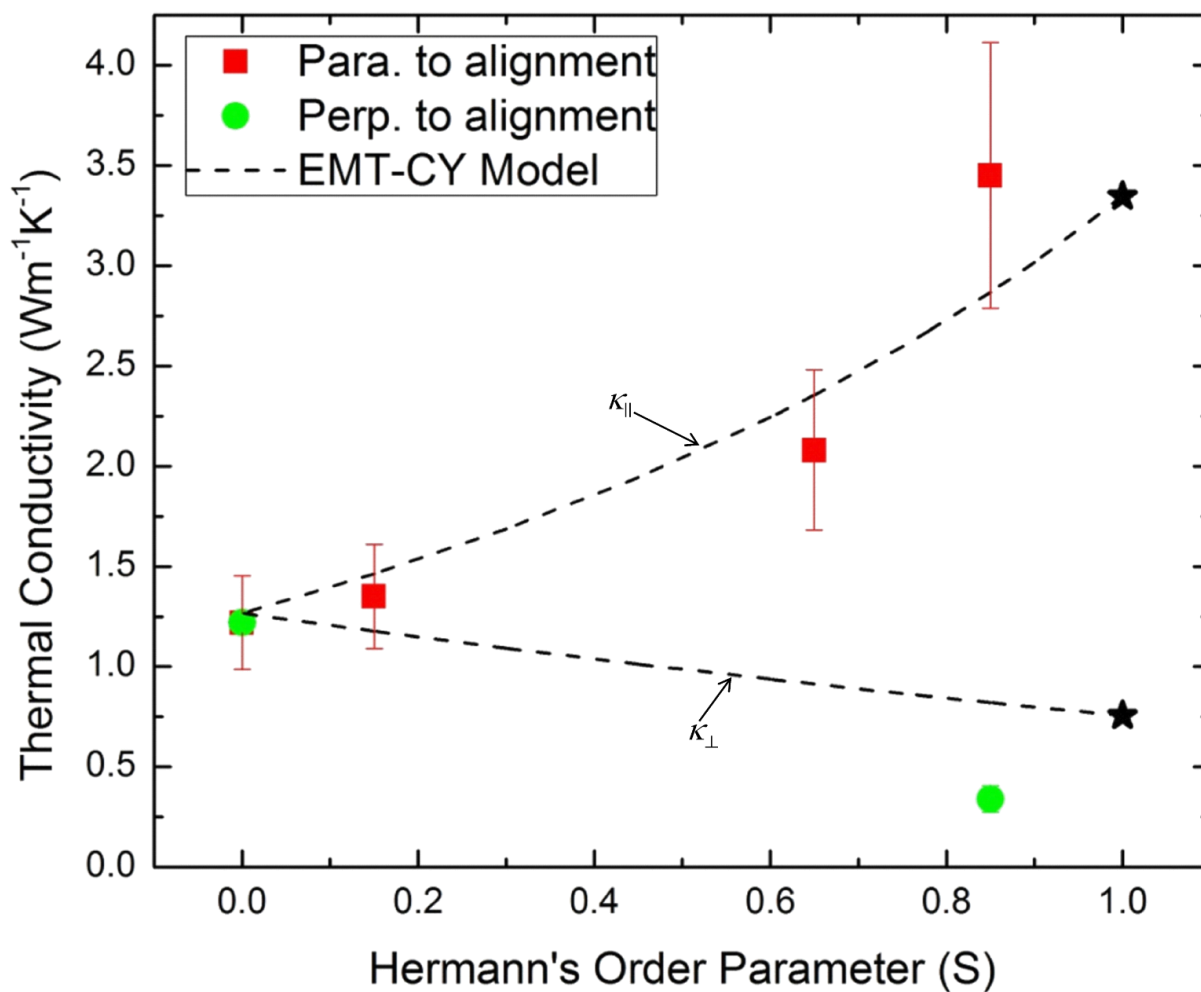


Figure 5.7 Experimental κ of anisotropic CNC-PVA composite films shown along with results from the EMT-CY model as a function of S . The weight % of CNC is not in particular order. The stars represent the extrapolated values of κ obtained from the EMT-CY model at $S \approx 1$

Figure 5.7 shows the experimentally obtained values of the κ of anisotropic CNC-PVA composite films along with those predicted by the EMT-CY model in the directions parallel ($\kappa_{||}$) and perpendicular (κ_{\perp}) to the shear direction. This model predicts a κ of $\sim 1.27 \text{ W m}^{-1} \text{ K}^{-1}$ for an isotropic film which is close to that of the experimental value ($\sim 1.22 \text{ W m}^{-1} \text{ K}^{-1}$). The model also

predicts the upper bound and lower bound values of κ_m to be $\sim 1.23 \text{ W m}^{-1} \text{ K}^{-1}$ and $\sim 0.46 \text{ W m}^{-1} \text{ K}^{-1}$, respectively. The lower end of this range is comparable to the upper end of the experimentally obtained κ value of neat PVA, specifically $\sim 0.08 \text{ W m}^{-1} \text{ K}^{-1}$ to $\sim 0.41 \text{ W m}^{-1} \text{ K}^{-1}$ for initial PVA weight % of 1 % to 10.7 %. This close agreement between κ_m and the κ of neat PVA suggests that other contributions to interfacial thermal resistance such as CNC-CNC or CNC-matrix interfaces are relatively small in comparison. In addition, the values of κ_m obtained are significantly larger than the effective κ_m value of $0.022 \text{ W m}^{-1} \text{ K}^{-1}$ obtained in our previous work on CNC-only films²⁵. Together, these insights show that the addition of PVA as an interstitial secondary material can have significant positive influence on the effective κ of CNC-based films, likely due to the removal of free volume and nanoscopic voids, which have extremely high effective resistance.

Relative to competitor materials, Table 5-1 shows that the in-plane κ of the best performing CNC-PVA composite film developed in this work is ~ 4 -14 times higher than that of other plastic films that are currently used for transparent, flexible devices indicating the potential of the CNC-PVA composite films an application for thermal management of flexible electronic devices. Regarding other CN-based materials the results presented here are ~ 1.4 times higher than that of the TNW sheet developed by Uetani et al.¹⁷². However, there are significant differences between the work here and Uetani. Primarily, the best results of Uetani were for Tunicate Nanowhiskers (TNWs) which are significantly longer (microns) than the wood-based CNCs here (100nm)⁵. As Diaz et al. showed that the long axis has a much higher κ than either orthogonal direction, the isotropic TNW materials should show much higher κ than the isotropic wood-based CNCs here, which is the case. However, the TNW materials show high effective interfacial resistance and low sound velocity in direct contrast to Diaz, although as Uetani stated, this was at least partially due

to small pores in the structure. Thus, reduction of interfacial resistance, and a concomitant increase in κ , would be expected to result from filling the free volume/small pores with a strongly bonded solid material. Additionally, Uetani showed a strong correlation with nanocrystal width, with TNW showing the highest κ , ostensibly as it was the widest material. Notwithstanding the correlation of width to length of the materials, which would have a large effect as described above, an isotropic random arrangement of CNC or TNW, as in a random mat, would be expected to have a large percentage of crossed crystal contact points. As contact points are where nearly all heat transport takes place and cross-points have less contact area than parallel axial contact along the width, it would be expected that isotropic arrangements would have higher effective interfacial resistance than anisotropic axial arrangements due to the higher amount cross-points relative to parallel axial contacts leading to less overall contact area to transport heat in the isotropic arrangement. Interestingly, as seen in Uetani, logically one would assume a high dependence on crystal width as, in a given volume, there would be more intracrystalline transport as opposed to across interfaces for larger widths. Regardless, combining the data sets, while the work here has a high κ , we should expect even higher for aligned composite structures of longer materials such as TNW.

The CNC-PVA composite films developed through this work show the potential for dissipating a significant amount of heat from electronics-like concentrated heat sources. Figure 5.8 shows thermal images obtained from a 100 % PVA sample and a CNC-PVA (90:10) sample as a demonstration of their relative ability to dissipate heat away from a localized hot spot. Identical serpentine gold heaters were shadow-evaporated on the surface of each of these samples and the same Joule heating power (175 mW) induced via a DC power supply. Thermal images were taken using almost identical temperature scales. As can be observed, the maximum temperature of the

resulting hot spot for the CNC: PVA composite sample was significantly lower ($\sim 7^\circ\text{C}$) than that of the neat PVA sample. The DC power was applied across the top left and bottom right contact pads of both samples, which results in the slight asymmetry as seen in the images.

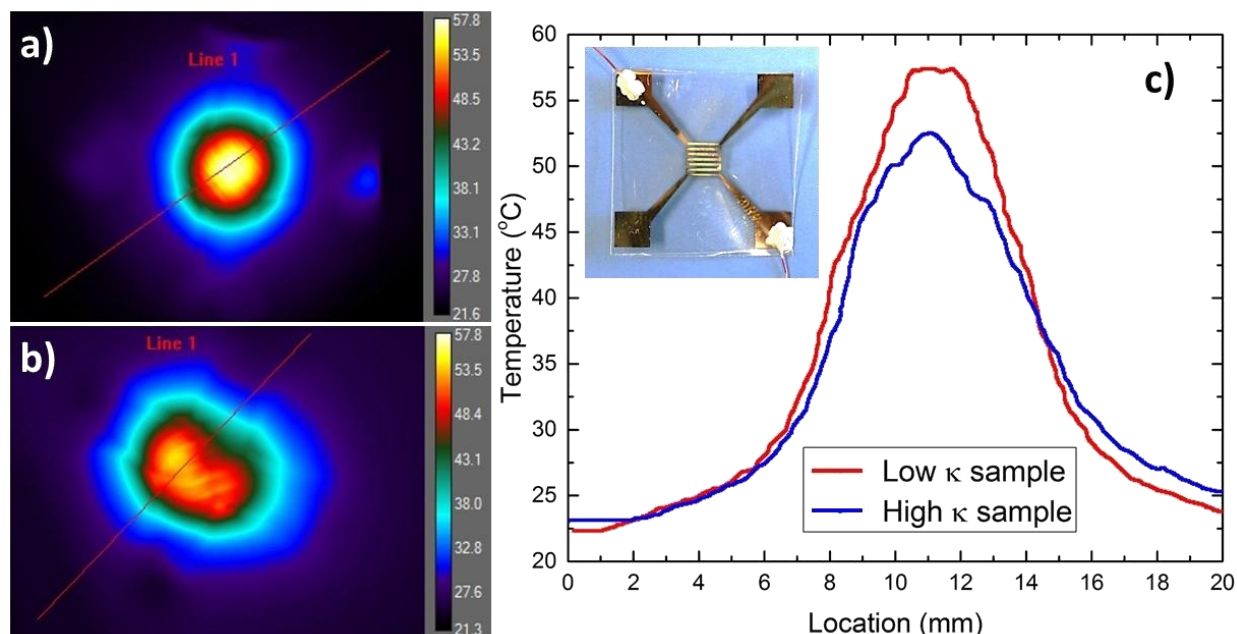


Figure 5.8 Thermal images of CNC-PVA composites a) 100 % PVA sample with low κ , and b) 90:10 CNC:PVA sample with high κ during Joule heating of a serpentine metallic heater simulating flexible electronics elements. c) Line scans along the centerline of a) and b) quantify the temperature reduction associated with the high κ sample at the same Joule heating power (175 mW). Inset: Photograph of 90:10 CNC:PVA sample with shadow-evaporated metallic heater.

5.4 Summary

In this work, CNC-PVA composite films consisting of PVA of different molecular weights and different CNC: PVA ratios were prepared with a variation of S between 0 to 0.85 for anisotropic films. The measurement of the κ showed significant improvement on isotropic CNC-PVA films with 10-50 wt% PVA solid loading compared to one component system. Further, the anisotropic composite films showed κ as high as $\sim 3.45 \text{ W m}^{-1} \text{ K}^{-1}$ in the shear direction which was a $\sim 2.5\text{X}$ improvement over the CNC-PVA composite films with the isotropic configuration.

Such improvements on κ of CNC-PVA composite films can be attributed to the role of PVA as excellent void filling agent for forming conductive paths for phonon transport with reduced interfacial resistance and the orientation of CNCs towards heat flow direction in anisotropic films. Compared to the commonly used plastic films for flexible electronic devices, our CNC-PVA composite films showed ~ 4 - 14 -fold higher κ while also demonstrating better heat spreading capability from a localized hot spot as would be experienced by a flexible electronics element. These results provide the basis for use of CNC-PVA composite films as substrates for potential application in the thermal management of flexible electronics and can be an eco-friendly and sustainable alternative to the petroleum-based polymeric material

CHAPTER 6. CONCLUSION AND FUTURE WORK

In this work, a large-scale waterborne coating process has been described for pristine CNCs and CNC-PVA nanocomposites. For the processing approach, controlled viscosity and substrate-coating compatibility are the most important parameters for the development of industrial quality coating. The coating formation is limited to a maximum 1 Pa.s for micro-gravure-based processing. Other parameters such as – substrate seed, speed ratio and gravure speed can combinedly control the capillary number of the coating formulations; hence, a defect free uniform coating is possible. In addition, mechanical shear rate (directly related with microgravure rotation) on the coating formulation controls the overall CNC alignment in the coating material. However, relaxation of the liquid crystal domains not only depends on the mechanical shear rate, but also on the viscoelastic nature of the coating formulations. Based on the extent of anisotropy, improved gas barrier performance is observed in the coating materials. The gas permeability of the CNC coatings depends on the crystallinity index, aspect ratio of individual domains, volume fraction of the anisotropic phase, and solubility of the gas molecules. Furthermore, an improved thermal conductivity (in-plane) is observed for CNC-PVA nanocomposite systems. Long PVA chains act as filler materials to reduce the interfacial thermal resistance between CNC domains, and effectively improve the phonon propagation in the bulk materials. The combined effect of anisotropic arrangement and reduced interfacial thermal resistance leads to an exceptional thermal conductivity that is essential for flexible electronics applications. From this work, some directions can be explored for future research.

6.1 Roll-to-roll CNC coating

One of the major drawbacks of the study is that the production rate is less than 2 m/min. The fabrication process is based on an aqueous suspension and longer time is required for evaporation. The drying unit is 1 m or less and only hot air is used for this fabrication. A new instrument design may overcome this limitation. Increasing drying unit length (directly proportional to production rate) with multiple hot dryer unit can significantly increase the production rate.

6.2 Roll-to-roll CNC-PVA composite coating

CNC-PVA coating formulations at PVA content of 10-30 wt % produced bubbles under micro-gravure rotation; hence, the solid coating surface contains defects like pin hole (about 10 bubbles/cm²). Reduction of viscosity of the coating formulation can be one of the solutions. However, reduced viscosity liquids showed faster relaxation of CNC domains, therefore, sacrificing the overall anisotropy. The overall objective of this work was to produce coating materials with controlled anisotropy. So, addition of a surfactant or defoamer should be a possible solution without sacrificing the order parameter.

6.3 Barrier performance of CNCs thin films

The Bharadwaj model is only the available theoretical approach that considers the effect of anisotropy on the barrier performance. However, the model does not take into account the interaction of gas molecules with coating materials. Moreover, CNCs film can form both chiral nematic and random configuration, and this model considers those as isotropic arrangement. Chiral nematic and random configuration possess different arrangements; hence, the gas permeability may not be identical. So, correction of Bharadwaj model is required for an appropriate validation of experimental data.

6.4 Thermal conductivity of CNC-PVA thin films

Inhibition of phonon propagation between liquid crystalline domains is the fundamental reason for the presence of interfacial thermal resistance. In this work, PVA is used as filler material and only secondary bonding was considered for the reduction of interfacial resistance. However, other filler materials that can form covalent bonds with CNCs might work more effectively for enhancing the thermal conductivity of nanocomposite systems.

APPENDIX A

Chapter 2: CONTINUOUS ROLL-TO-ROLL FABRICATION OF TRANSPARENT CELLULOSE NANOCRYSTAL (CNC) COATINGS WITH CONTROLLED ANISOTROPY

Definition

Capillary number, Ca, is defined by the following equation:

$$Ca = \frac{\mu V}{\gamma} \dots \dots \dots (1)$$

Here, V is velocity of the object relative to liquid, μ is the viscosity of liquid and γ is the surface tension. Modification of this standard equation can successfully explain the liquid transfer phenomenon. The capillary number can be written in terms of gravure and web velocity.

$$Ca = \frac{\mu (U_{roll} + U_{web})}{\gamma} \dots \dots \dots (2)$$

Here, U_{roll} is the gravure roll velocity.

Speed ratio: The velocity ratio of the roll speed to web speed is defined as speed ratio.

$$S = \left(\frac{U_{roll}}{U_{web}} \right) \dots \dots \dots (3)$$

Section 1.1: Parameter data for different CNC concentrations

Table AS1: 6wt% CNC suspension speed variables, capillary number, and thickness.

Uroll, m/min	Uweb, m/min	Speed ratio	Ca	Thickness, μm
0.504	1.000	0.504	7.8154e-3	2.06 \pm .2
0.693	1.000	0.693	7.0277e-3	2.08 \pm .48
1.008	1.000	1.008	6.2400e-3	2.45 \pm .21
2.016	1.000	2.016	5.8385e-3	2.42 \pm .54
4.095	1.000	4.095	6.5577e-3	3.1 \pm .31
0.630	1.250	0.504	8.2385e-3	2.1 \pm .35
0.630	0.960	0.656	6.9308e-3	2.1 \pm .32
0.630	0.630	1.000	5.6231e-3	2.8 \pm .21
0.630	0.450	1.400	4.8385e-3	2.9 \pm .32
0.630	0.310	2.032	4.0538e-3	3.1 \pm .15
1.033	1.010	1.023	6.3702e-3	2.7 \pm .44
0.882	0.880	1.002	5.9400e-3	2.5 \pm .38
0.762	0.760	1.003	5.7012e-3	2.09 \pm .31
0.630	0.630	1.000	5.6231e-3	2.05 \pm .24
0.504	0.500	1.008	4.7938e-3	1.9 \pm .41
2.016	1.010	2.000	6.1498e-3	3.39 \pm 0.30
1.764	0.880	2.005	7.9920e-3	3.25 \pm 0.58
1.512	0.756	2.000	6.2954e-3	2.94 \pm 0.42
1.298	0.650	1.997	5.4718e-3	2.88 \pm 0.50
1.021	0.510	2.001	4.8096e-3	2.75 \pm 0.29

Table AS2: 9wt% CNC suspension speed variables, capillary number, and thickness.

Uroll, m/min	Uweb, m/min	Speed ratio	Ca	Thickness, μm
0.504	1.000	0.504	0.0313	2.86 ± 0.32
0.693	1.000	0.693	0.0307	3.20 ± 0.48
1.008	1.000	1.008	0.0364	3.60 ± 0.31
2.016	1.000	2.016	0.0311	3.80 ± 0.52
4.095	1.000	4.095	0.0525	4.10 ± 0.48
0.630	1.230	0.512	0.0339	2.60 ± 0.31
0.630	0.920	0.685	0.0285	2.80 ± 0.32
0.630	0.640	0.984	0.0232	3.50 ± 0.40
0.630	0.460	1.370	0.0199	4.10 ± 0.41
0.630	0.350	1.800	0.0167	4.20 ± 0.43
1.033	1.010	1.023	0.0337	3.59 ± 0.54
0.882	0.880	1.002	0.0320	3.70 ± 0.54
0.762	0.760	1.003	0.0285	3.55 ± 0.50
0.630	0.630	1.000	0.0232	3.01 ± 0.54
0.504	0.500	1.008	0.0227	2.90 ± 0.43
2.016	1.008	2.000	0.0311	4.66 ± 0.46
1.764	0.880	2.005	0.0342	4.4 ± 0.63
1.512	0.756	2.000	0.0286	4.59 ± 0.62
1.298	0.650	1.997	0.0251	4.11 ± 0.72
1.021	0.510	2.001	0.0231	4.37 ± 0.37

Table AS3: 12wt% CNC suspension speed variables, capillary number, and thickness.

Uroll, m/min	Uweb, m/min	Speed ratio	Ca	Thickness, μm
0.504	1.000	0.504	0.0625	4.38 ± 0.29
0.693	1.000	0.693	0.0615	4.5 ± 0.43
1.008	1.000	1.008	0.0572	4.72 ± 0.48
2.016	1.000	2.016	0.0584	4.94 ± 0.27
4.095	1.000	4.095	0.0787	6.27 ± 0.52
0.630	1.260	0.500	0.0727	3.72 ± 0.19
0.630	0.950	0.663	0.0612	4.16 ± 0.32
0.630	0.630	1.000	0.0496	4.94 ± 0.29
0.630	0.470	1.340	0.0427	5.08 ± 0.41
0.630	0.320	1.969	0.0358	5.41 ± 0.52
1.033	1.010	1.023	0.0579	4.38 ± 0.26
0.882	0.880	1.002	0.0548	4.22 ± 0.19
0.762	0.760	1.003	0.0532	3.94 ± 0.24
0.630	0.630	1.000	0.0496	3.72 ± 0.26
0.504	0.500	1.008	0.0404	3.72 ± 0.21
2.016	1.008	2.000	0.0584	5.05 ± 0.47
1.764	0.880	2.005	0.0546	4.94 ± 0.40
1.512	0.756	2.000	0.0492	4.94 ± 0.38
1.298	0.650	1.997	0.0487	5.08 ± 0.55
1.021	0.510	2.001	0.0423	5.20 ± 0.42

Instrument configuration

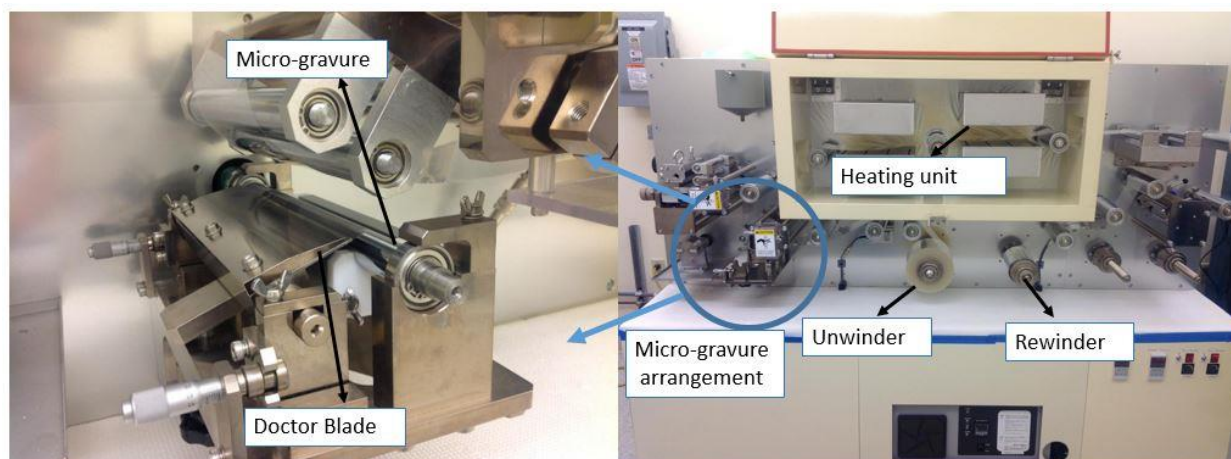


Figure AS1: Mirwec Mini-Labo Deluxe™ roll-to-roll micro-gravure instrument.

Introduction of defect on fabrication process

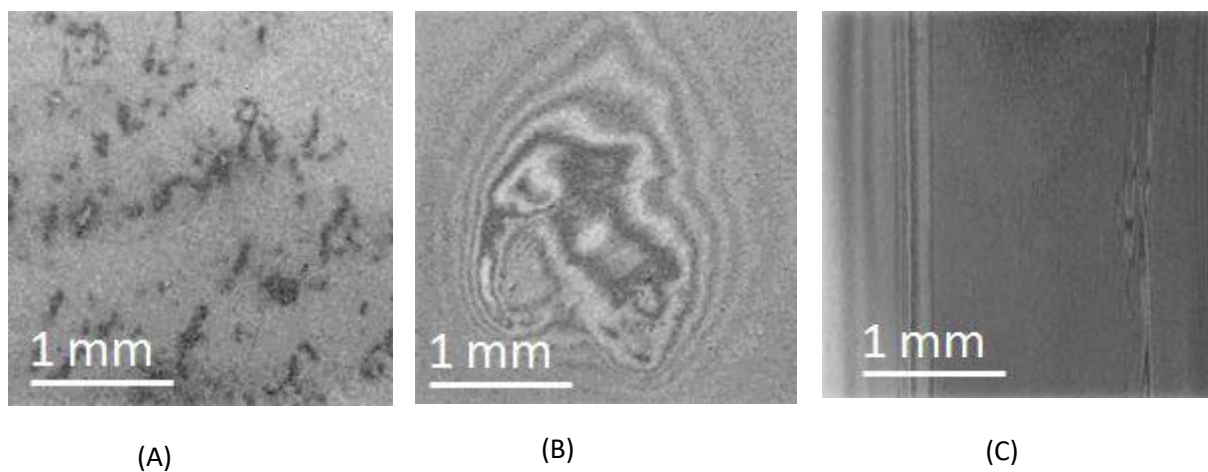
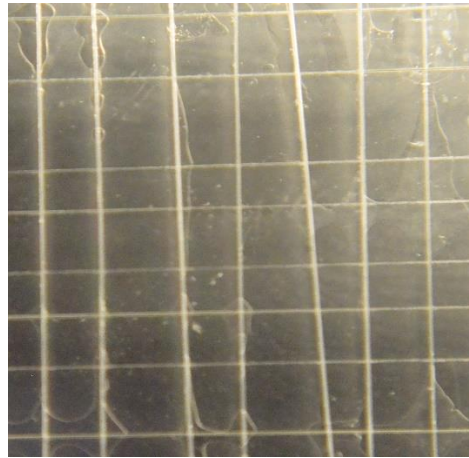


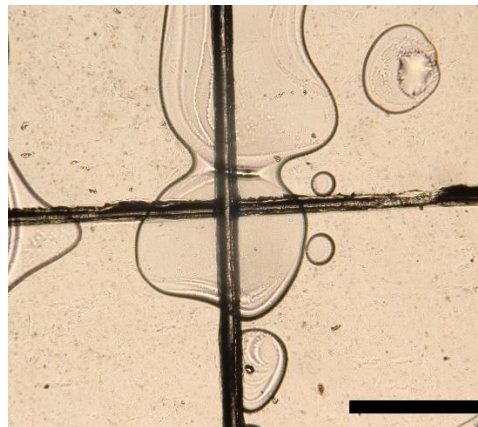
Figure AS2: Defect formation at very low speed ratio, (A) uneven coating, and at very high-speed ratio, (B) de-wetting, and (C) line defect.

Detection of CNC coating in cross-hatch peeling test

visual inspection



Under optical microscope



Optical microscope with
cross polarizer

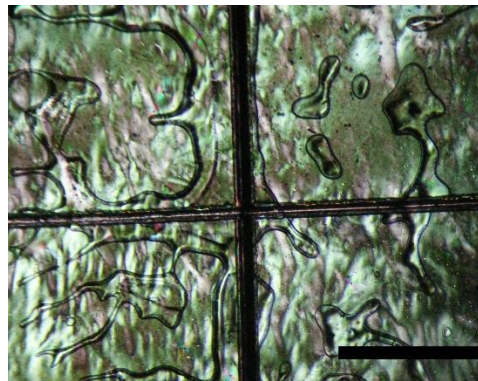


Figure AS3: detection of CNC coating with polarized optical microscope.

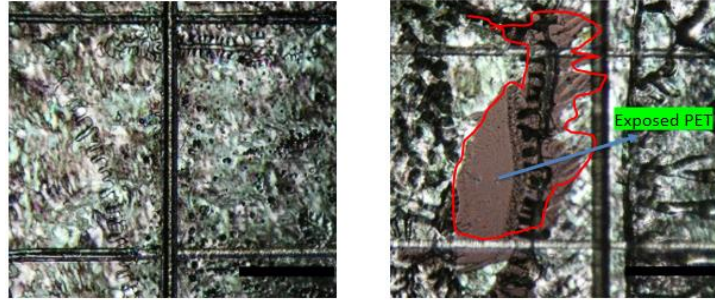


Figure AS4: Coating array before and after crosshatch test with the de-bonding spot of individual grids with exposed PET surface.

Order parameter calculation for different CNC concentration

Table AS4: Dichroic ration from maximum transmittance intensity for different specimen and resulted Herman order parameter (S).

CNC concentration	Transmittance light intensity for 45° configuration	Transmittance light intensity for 90° configuration	Dichroic ratio	Order parameter
6wt%	21.3	11.9	1.79	0.21
	22.9	13.5	1.70	0.19
	27.4	14.1	1.94	0.24
	23.3	12.32	1.89	0.23
	30.1	15.1	2.05	0.26
9wt%	34.2	11.4	3.00	0.40
	38.6	11.4	3.40	0.45
	40.1	10.6	3.80	0.49
	31.4	8.5	3.70	0.48
	36.7	10.2	3.60	0.47
12wt%	40.6	10.2	4.00	0.50
	37.9	8.2	4.60	0.55
	42.6	6.5	6.50	0.65
	44.9	8.2	5.50	0.60
	38.6	8.4	4.60	0.55

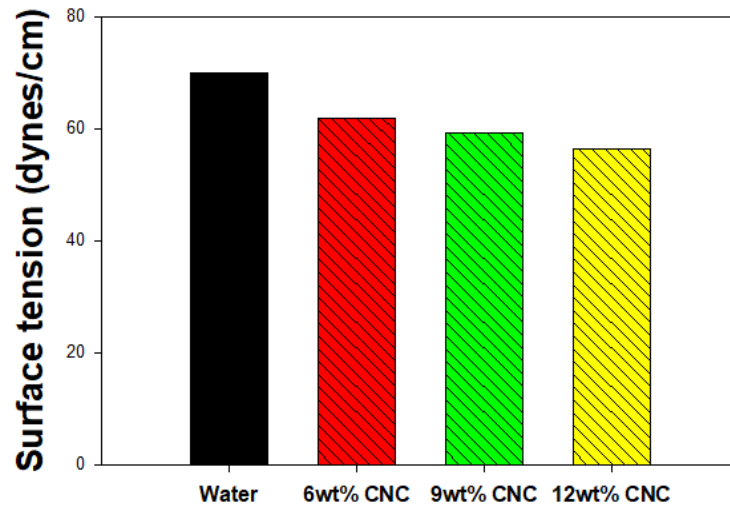


Figure AS5: Surface tension for three different CNC concentrations.

Microgravure properties

R30 microgravure is a small contact angle area gravure that creates a very uniform, and exceptional stable thin liquid layer on any flexible substrate. The gravure diameter is 20×10^{-3} m with a 20° tilt angle mesh direction. The gravure surface has 30 mesh lines per inch where cell volume and cell depth are $170 \text{ cm}^3/\text{m}^2$ and $300 \mu\text{m}$ respectively.

APPENDIX B

Chapter 3 Roll-to-Roll fabrication of cellulose nanocrystal-poly(vinyl alcohol) composite coatings with controlled anisotropy

Table BS1: Different parameters used for this fabrication process

Coating on PET substrate

Name	Parameter
Gravure type	30 R
Gravure speed	30 prm
Substrate speed	1 m/min
Substrate thickness	50 μm
Drying temperature	80 $^{\circ}\text{C}$
Speed ratio (gravure/substrate speed)	2

Coating on PLA substrate

Name	Parameter
Gravure type	90 R
Gravure speed	30 prm
Substrate speed	1 m/min
Substrate thickness	20 μm
Drying temperature	45 $^{\circ}\text{C}$
Speed ratio	2

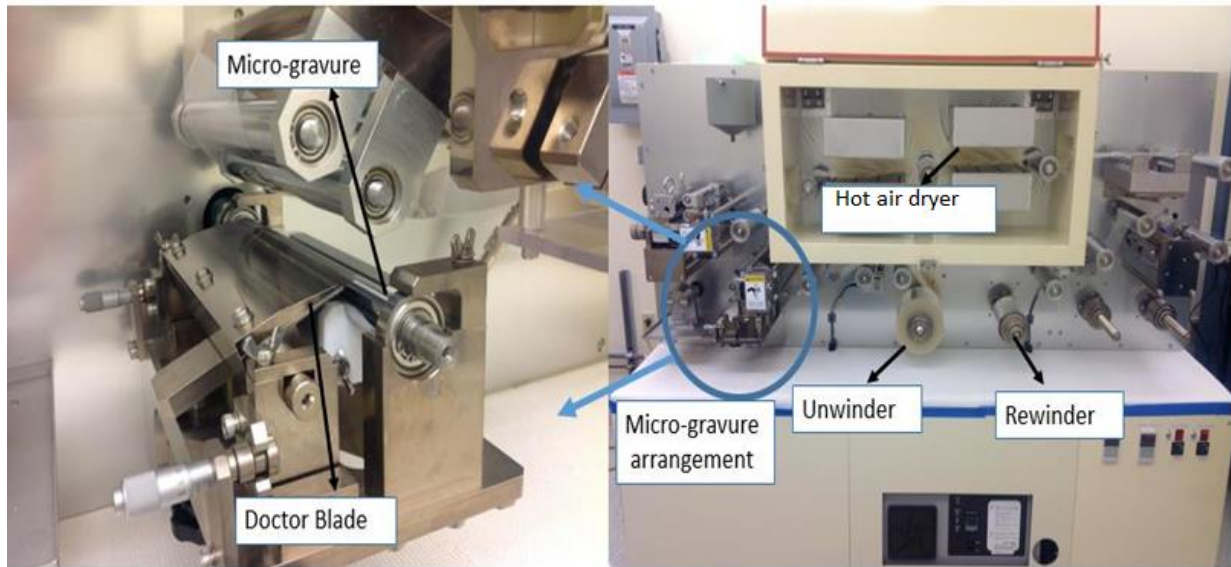


Figure BS1: Roll to roll microgravure system for PVA-CNC coating on a flexible substrate.

SEM micrograph for different coating:

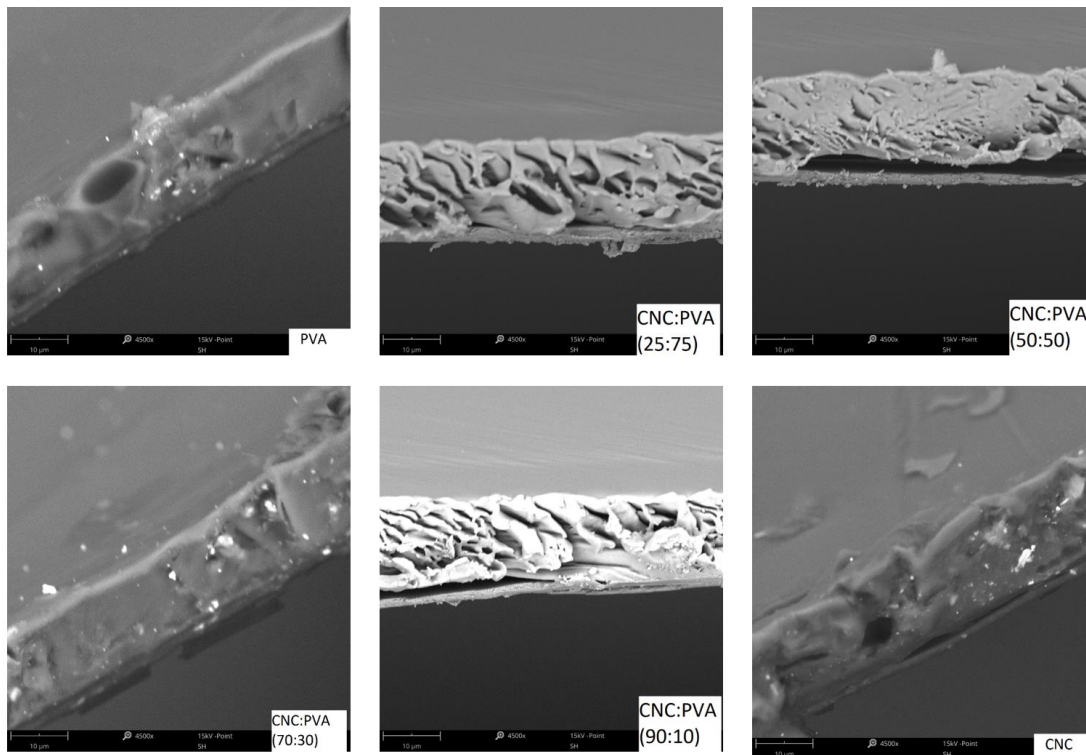


Figure BS2a: coating thickness on the PLA substrate

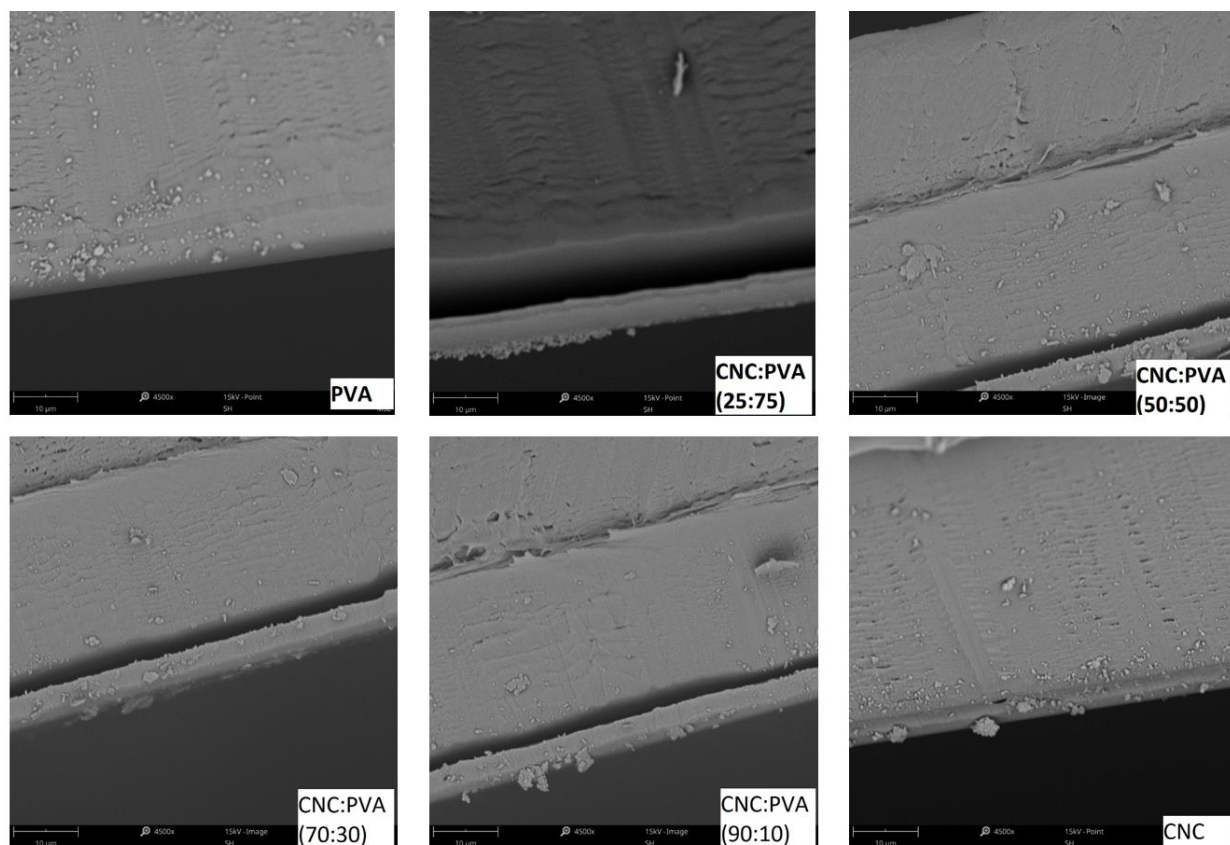
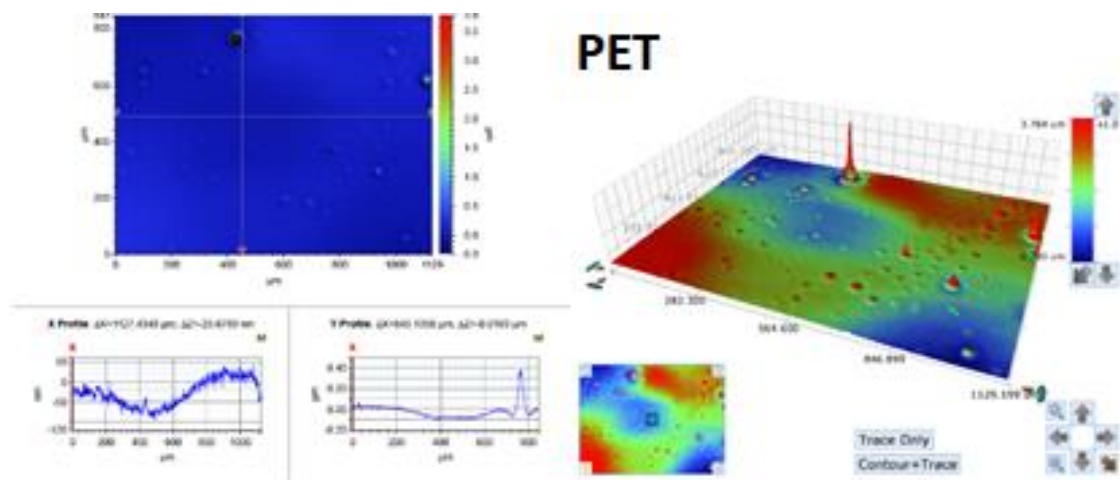
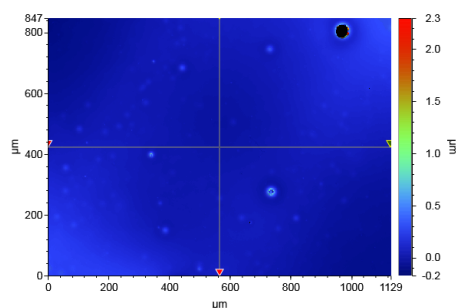


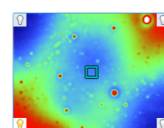
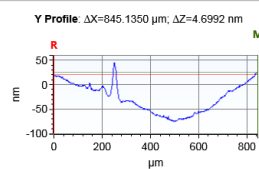
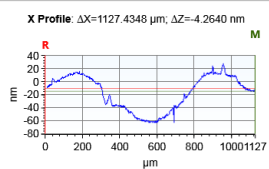
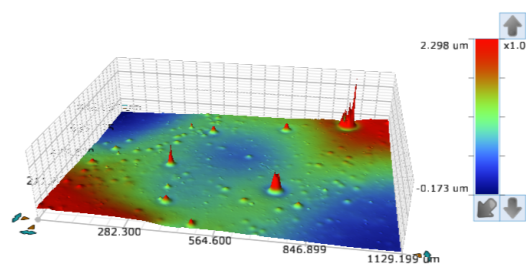
Figure BS2b: coating thickness on the PET substrate.

Surface roughness for different coating formulations:

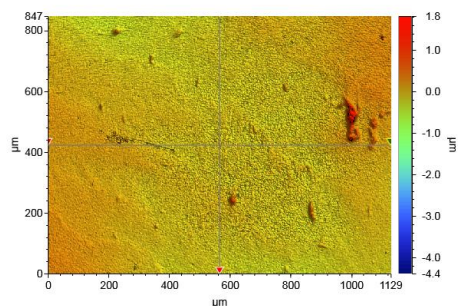




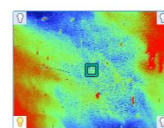
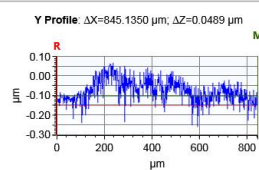
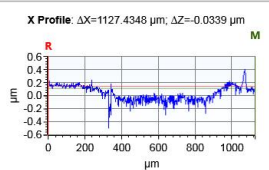
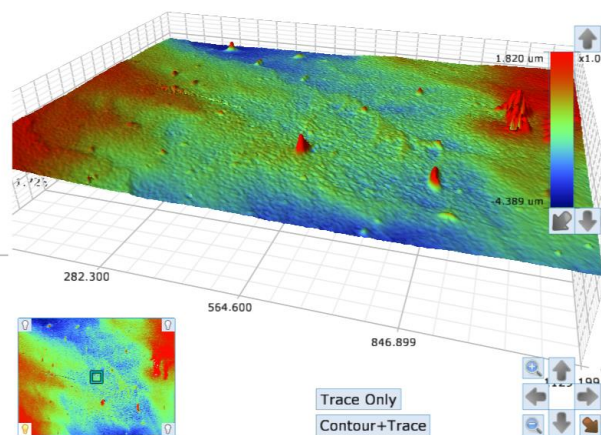
PVA



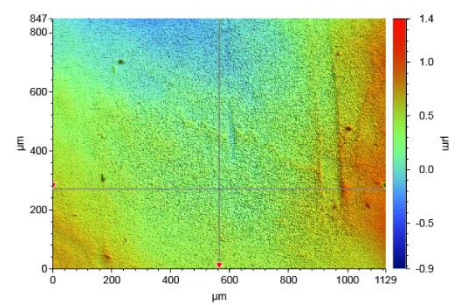
Trace Only
Contour+Trace



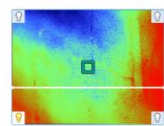
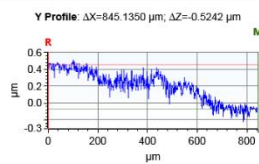
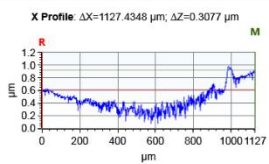
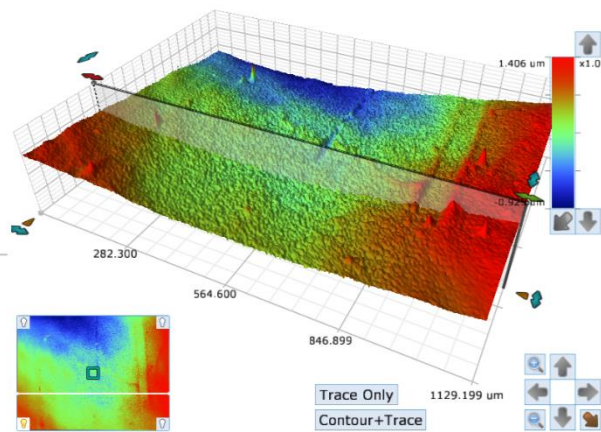
CNC-PVA (25:75)



Trace Only
Contour+Trace



CNC-PVA (50:50)



Trace Only
Contour+Trace



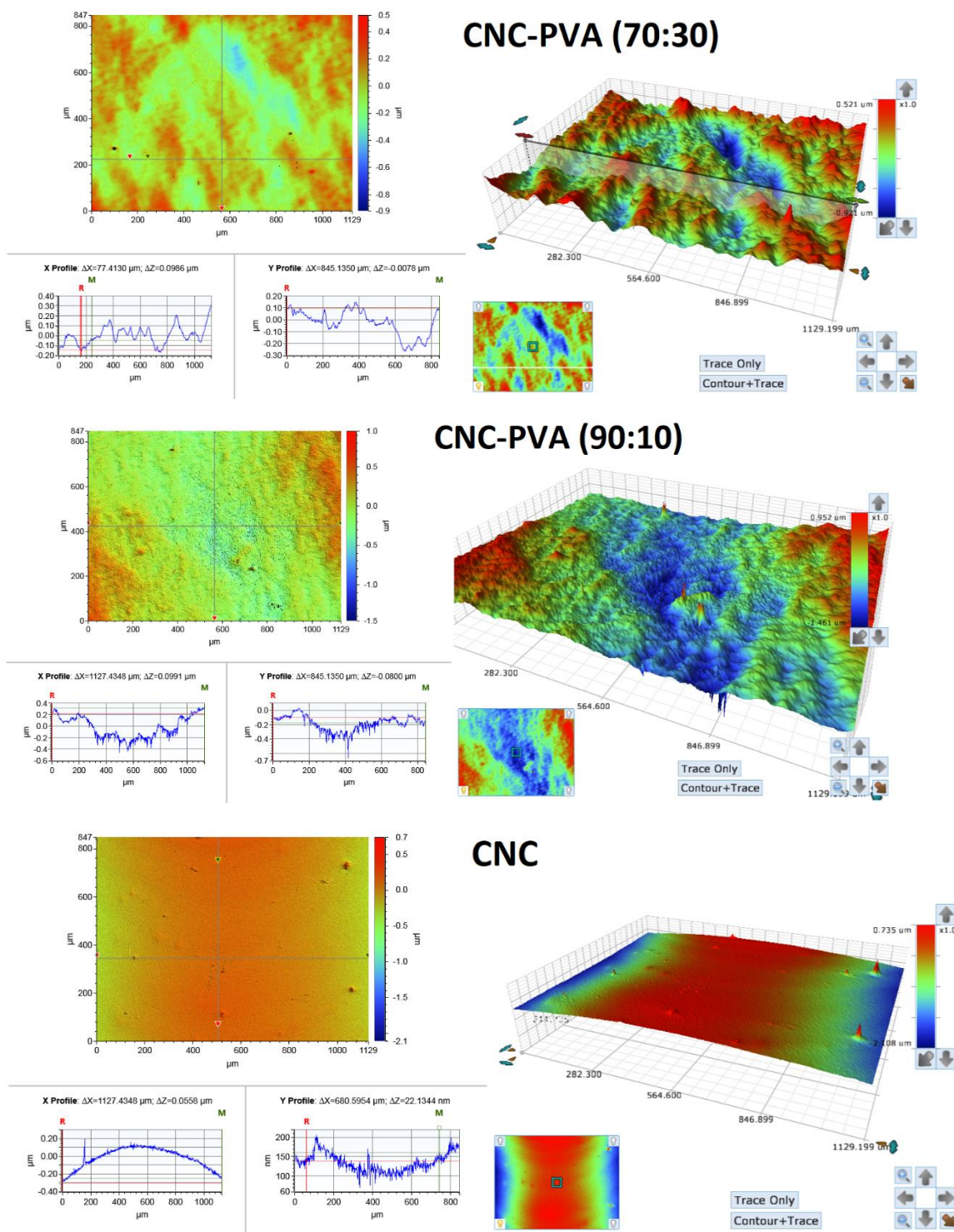


Figure BS3: 3D surface profile with corresponding surface roughness for different CNC-PVA compositions coating on the PET substrate.

Table BS2: surface roughness data for different coating compositions

Sample	roughness
PET	30 ± 1.5
CNC:PVA (0:100)	24 ± 1.3
CNC:PVA (25:75)	34 ± 1.7
CNC:PVA (50:50)	44 ± 2.2
CNC:PVA (70:30)	100 ± 5
CNC:PVA (90:10)	80 ± 4
CNC:PVA (100:0)	35 ± 1.75

Transmittance light intensity measurement for anisotropic coating:

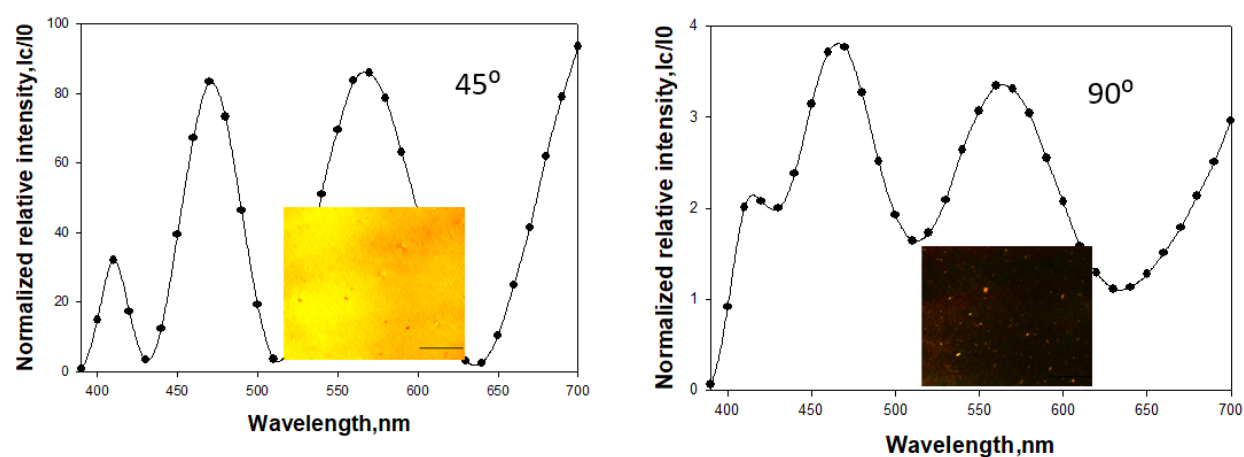


Figure BS4: Transmittance light intensity of anisotropic CNC-PVA coating for 45° and 90° configurations with corresponding optical images under a cross polarizer (scale bar 0.5mm).

Damage detecting in the Cross-hatch test:

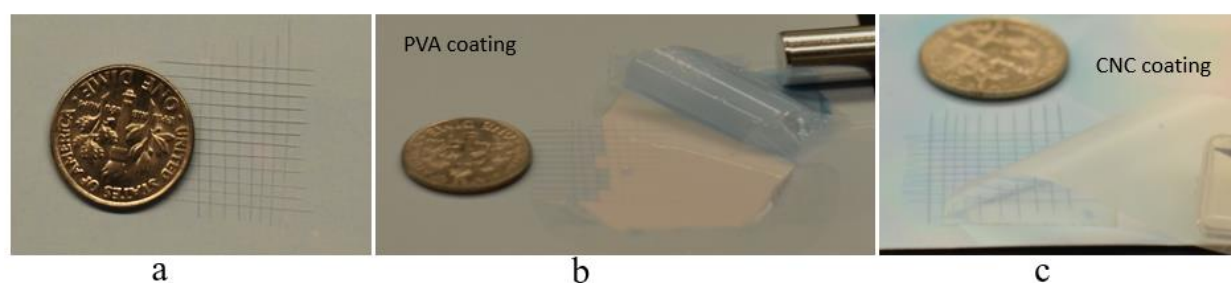


Figure BS5: Coating array before (a) and after (b, and c) crosshatch test. De-bonding spot with exposed PET surface was prominent for pure PVA coating compared to the CNC coating.

Microgravure properties:

Two different types of micro-gravure (such as R30 and R90) were used for this fabrication.

Both micro gravures are small contact angle area gravure and they can create very uniform, and exceptional stable thin liquid layer on any flexible substrate. Gravure diameter, cell volume and cell depth section for the micro-gravure systems are given below:

Micro-gravure	Gravure diameter	Cell volume, cm^3/m^2	Cell depth, μm	Mesh lines/inch
R30	20×10^{-3}	150	300	30
R90	20×10^{-3}	49	95	90

Surface energy of PET and PLA substrate:

Table BS3: Effect of corona treatment on the substrate surface energy

Substrate	Surface energy of the substrate roll		Surface energy after corona treatment	
	Inner surface, mN/m	Outer surface, mN/m	Inner surface, mN/m	Outer surface, mN/m
PET	44-46	44-46	64-66	64-66
PLA	52-54	44-46	64-66	62-64

Real time particle movement measurement process:

The aqueous thickness of any coating formulation, time of flight of a doctor blade and the length of a coating area control the applied shear rate. Following equation was used to calculate shear rate.

$$\text{shear rate} = \frac{\text{length}(l)}{\text{time} * \text{height}(h) \text{ from bottom surface}}$$

Here, length (l) was 3cm length of the PET strip, height (h) was 50 μ m PET strip thickness and time (t) was 2s time duration of the doctor blade to cover length (l) over the PET strip. Shear rate control process has been shown in figure S6. Immediately, the whole arrangement was placed at 45° configuration under a polarized microscope and data was recorded in video format, where a regular stopwatch is used to measure the time scale.

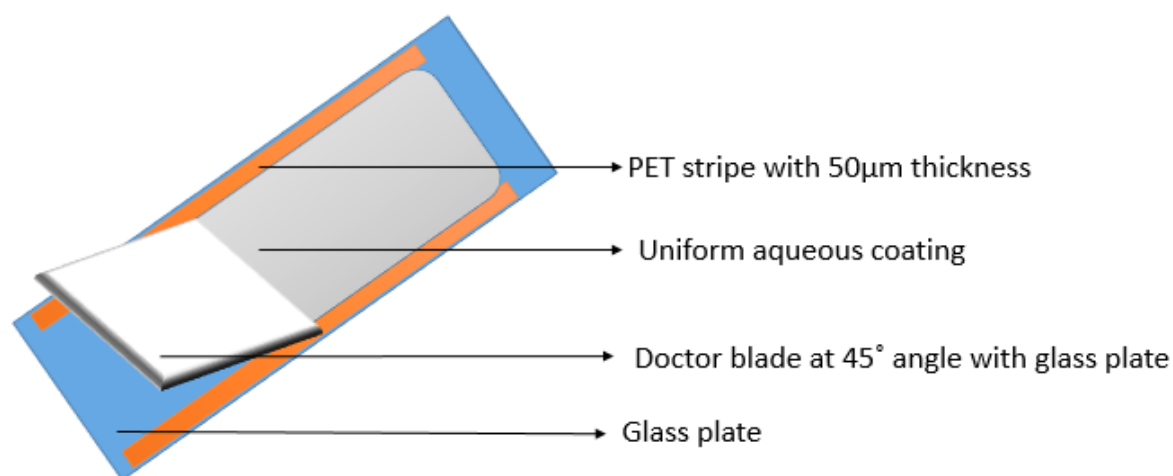
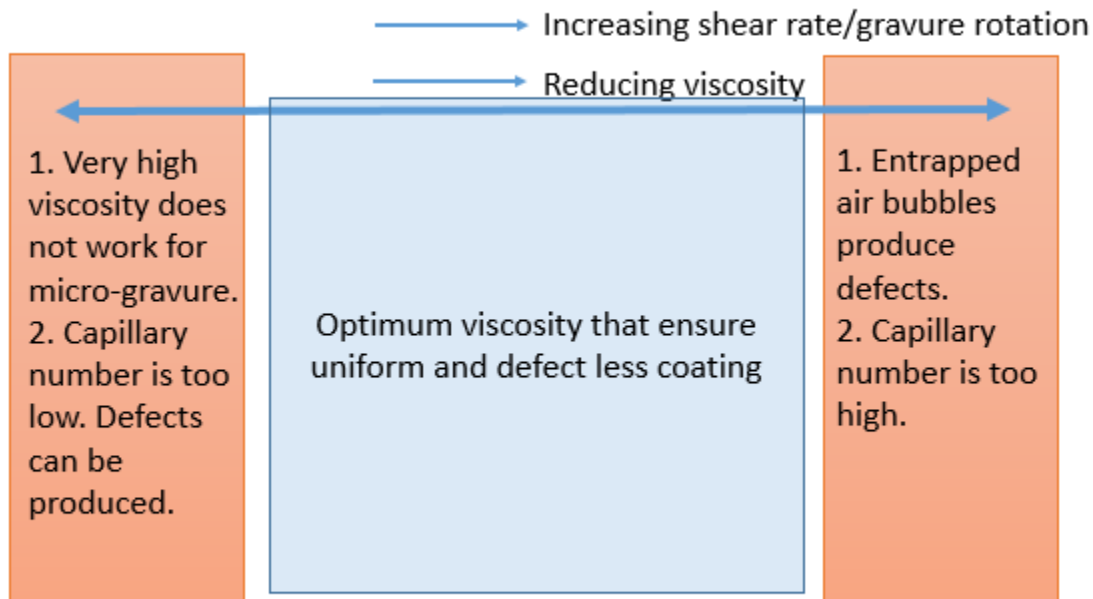


Figure BS6: Constant shear rate setup for the measurement of real time birefringence.

Selection of shear rate based on the coating formulation:

Viscosity of coating formulation based on Gravure rotation/ shear rate



Note: Capillary number can be controlled by both viscosity and roller speed. But, shear rate dominates capillary number for this fabrication process.

Optical profilometer:

3D Optical profilometer (OP) is a non-contact mode imaging system that can visualize a large sample area compare to the traditional methods. Some conventional imaging systems provide relatively small scan size, and it is difficult to correlate multiple scans for visualizing a large sample area with complex geometry.

3D OP, which uses interference to measure the surface and thus has a higher lateral resolution, in this case <0.5 micron as opposed to a typical AFM, which would be ~2 micron between lines and therefore a deconvolution would give ~10-micron resolution. At the same time, OP allows a much larger sample size and also gives similar z-resolution to AFM. Our intent was to determine the coating surface quality and if the gravure affected the structure, if there were micro-sized dewets, pinholes, line defects, etc. Thus, a large sample area is needed, and 1-micron lateral resolution is acceptable.

Coated PET film transparency for haze and clarity:



Figure BS7: Total transparency of coated PET film with very low haze and high clarity. (Black dotted line for showing film outline.)

The setting of shear rate measurement:

Rheology measurements were conducted starting with a 1-minute pre-shearing at 350 s^{-1} , then, after 30 seconds rest, a shear rate-controlled ramp with log increments from 1 to 500 s^{-1} was applied. Initial delay time (at $1/\text{s}$) was 30 seconds and 5 seconds integration time, both times decreased logarithmically until 5 seconds delay time and 1 second integration time at 500 s^{-1} . It was found in previous tests that after shearing at 350 s^{-1} for 1 minute, resting time of 1, 3, 10, 300 and 1000 seconds, and resuming the 350 s^{-1} rate, viscosity stabilized under 5 seconds. The apparent viscosity was under 1 Pa s at all times for shear rates above 2 s^{-1} .

APPENDIX C

Chapter 4: Cellulose Nanocrystal (CNC) Coatings with Controlled Anisotropy as High-Performance Gas Barrier Films

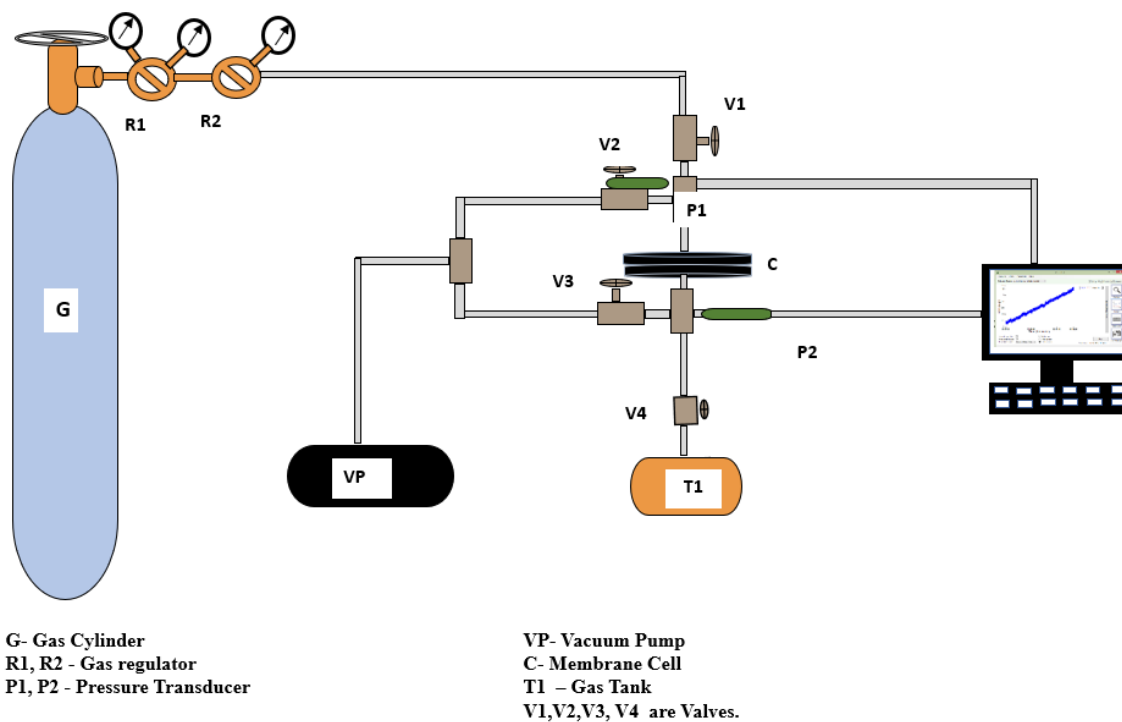


Figure CS1 : Schematic diagram of gas permeability instrument.

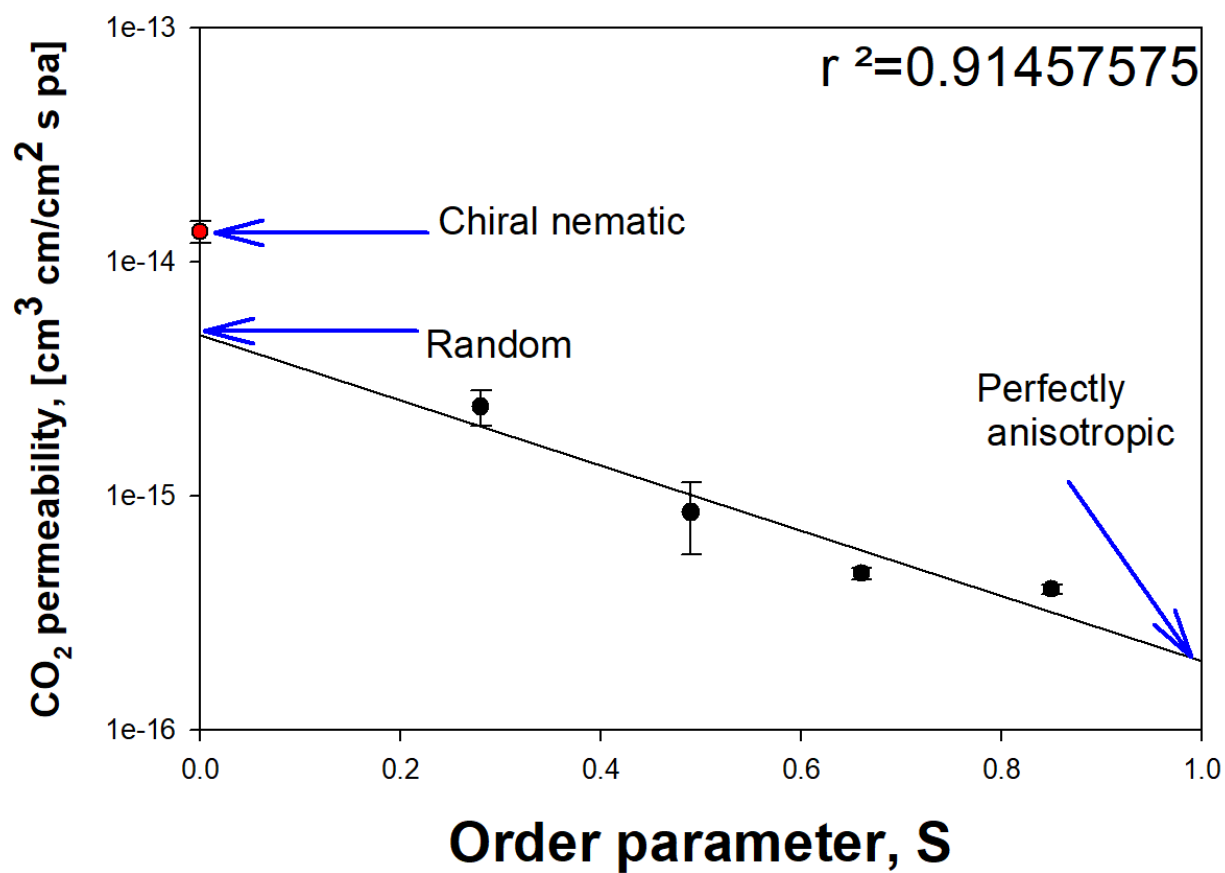


Figure CS2: Prediction of CO_2 gas permeability for completely random and anisotropic configuration.

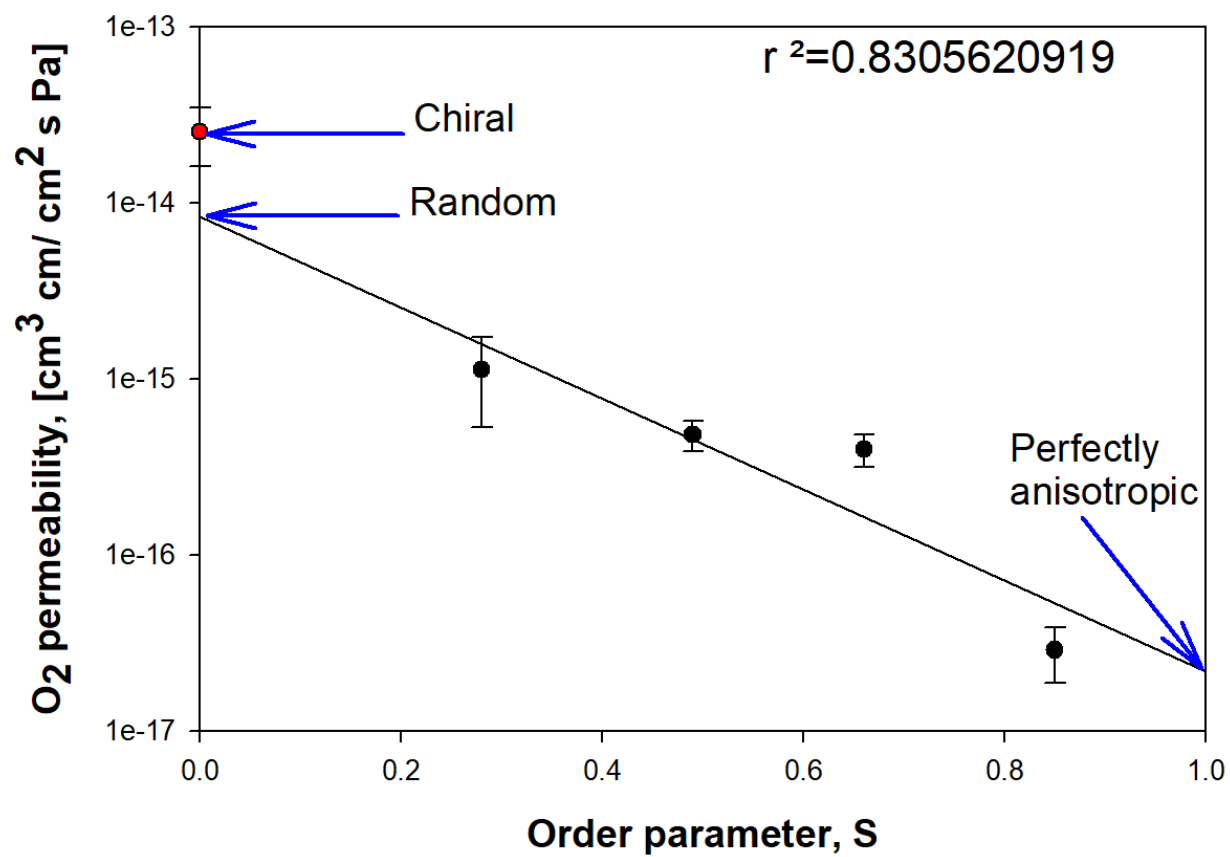


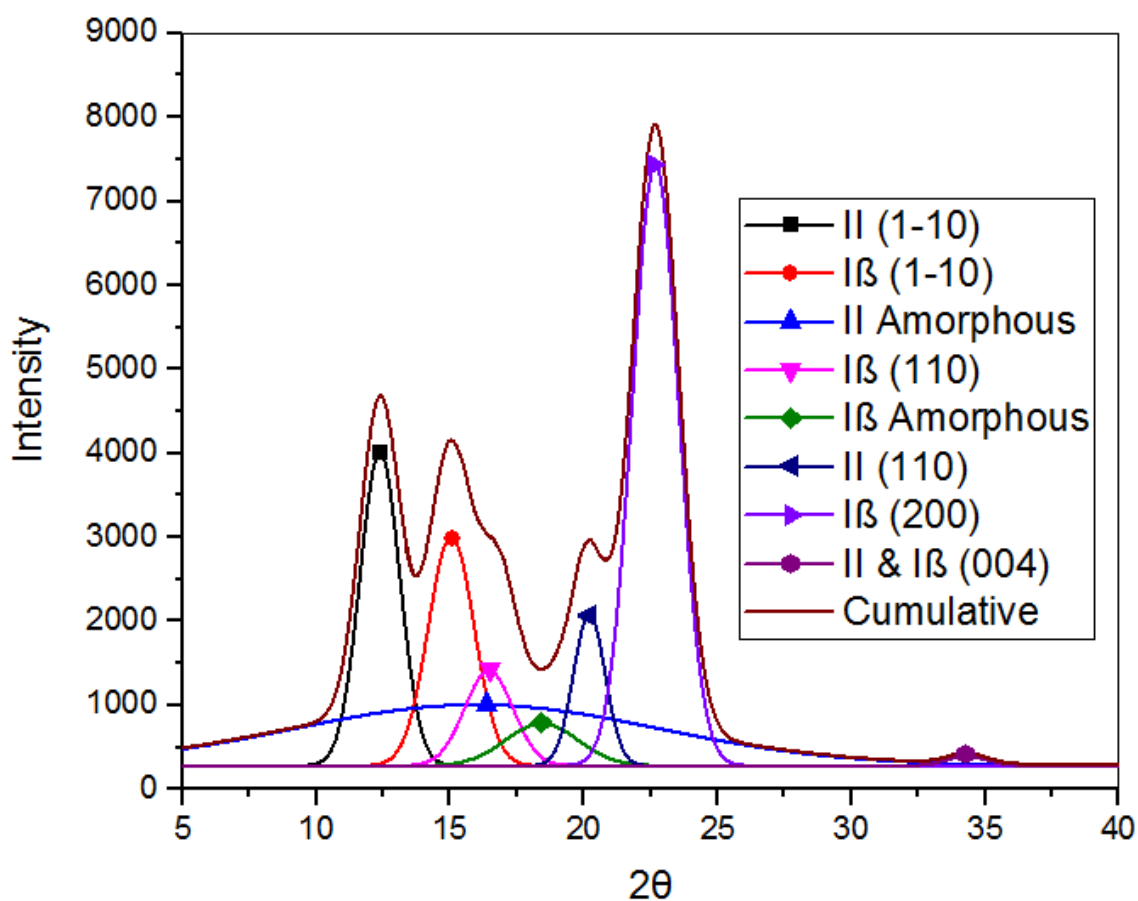
Figure CS3: Prediction of O_2 gas permeability for completely random and anisotropic configuration.

Table CS1: Gas permeability data for different polymer systems.

Name	CO ₂ (cm ³ cm/cm ² sPa)	O ₂ (cm ³ cm/cm ² sPa)	Reference
LDPE	9.50E-13	2.20E-13	190
HDPE	2.70E-14	3.00E-14	190
PP	6.90E-13	1.70E-13	190
PS	7.90E-13	2.00E-13	190
PM	2.33E-13	1.16E-14	190
PDS	3.49E-10	6.95E-11	190
PEM	3.79E-13	8.89E-14	190
PC	1.92E-12	2.96E-13	190
PMPS	1.73E-10	2.87E-11	190
PVC	1.20E-14	3.40E-15	190
PVA	1.52E-13	3.67E-14	190
Saran	2.10E-15	3.80E-16	190
Halar	4.60E-14	1.14E-14	190
PLA	9.34E-14	3.39E-14	190
Poly(acrylonitrile)	6.00E-17	1.50E-17	190
Barex	1.20E-15	4.10E-16	190
Lopac	8.10E-16	2.60E-16	190
PVOH	9.20E-16	6.60E-16	190
EVOH	1.10E-15	6.65E-16	190
Parylene C	3.40E-15	3.19E-15	190
Cellophane	9.70E-16	5.30E-16	190
CA	1.73E-12	5.80E-14	190
CN	1.59E-13	1.46E-13	190
Mylar A	1.18E-14	2.57E-15	190
nylon 6	6.60E-15	2.85E-15	190
CNF	2.72E-15	6.49E-15	This work
CNC (S=0)	1.35E-14	2.55E-14	This work
CNC (S=.28)	2.41E-15	1.13E-15	This work
CNC(S=.49)	8.52E-16	4.83E-16	This work
CNC (S=.66)	4.66E-16	3.99E-16	This work
CNC(S=.85)	3.98E-16	2.88E-17	This work

Crystallinity Index from XRD:

Sample Preparation: 24gr of a 5wt% solution of FPL071 was placed into a 50mm polystyrene petri dish and left inside a fume hood to dry over 72 hours. An approximately ~5mm thick film was obtained. An X-ray diffractogram was taken using a Panalytical Empyrean Powder X-ray diffractometer, with Cu radiation (1.540598 \AA) at 45 kV and 40 mA. The angular interval was set from 5 to 40 and the film was placed on a single crystal silicon wafer in rotational mode with a period of 2s. No background correction was made.



Plane	2θ	Peak Height	FWHM
II (1-10)	12.4	4018	1.7482
Iβ (1-10)	15.0	3010	2.0227
II Amorphous	16.0	1006	16.0787
Iβ (110)	16.5	1412	2.1244
Iβ Amorphous	18.4	784	3.1785
II (110)	20.2	2080	1.4048
Iβ (200)	22.7	7449	2.0444
II & Iβ (004)	34.3	395	1.7641

The diffractometry displayed 6 peaks characteristic of Cellulose Iβ and II. Peaks were identified and deconvoluted using OriginPro 2015 and Segal Crystallinity index was calculated² from the (200) plane of cellulose Iβ, using the following equation, where I is the intensity of the deconvoluted peak at the plane's characteristic angle.

$$CI\% = \frac{(I_{I\beta (200)} - I_{I\beta Amorphous})}{I_{I\beta (200)}}$$

$$CI\% = 89\%$$

Zeta Potential:

Cellulose slurries were diluted in pure/DI water (>18 MΩ/cm) and mixed using an ultrasonic sonic mixer (Branston Digital Sonifier Model 102C) for 30 s at 25% intensity. Zeta potential of the dilutions was then measured using a Zetasizer Nano ZS equipment (Malvern Instruments Ltd), at 23°C in a DTS1070 disposable cuvette. Measurements were repeated 10 times.¹⁹⁰

Z potential [mV]		
	Avg.	St.Dev.
FPL CNC 071	-45.5	1.55
FPL CNF 080	-29.1	5.66

TEM:

Using ImageJ, CNC length and width were manually measured from TEM micrographs from a Philips CM-100 operated at 100 kV. Measurements were calculated from the following figures. Image J software was used for the length and width measurement. The average length and width were 99 ± 27 nm and 5.4 ± 1.8 nm respectively. The average value was measured from 60 individual measurements on whole CNC.

The Bharadwaj model is based on the crystalline domains length and width. To reduce complexity in the model calculation, every crystal was considered to be 100 nm long and 5 nm width.



APPENDIX D

Chapter 5 Superior, Processing-Dependent Thermal Conductivity of Cellulose Nanocrystal-Poly(vinyl alcohol) Composite Films

Table DS1: Nanocomposite Preparation Material Concentrations for Isotropic Films.

Mw of PVA	Initial CNC wt%	Initial PVA wt%	CNC:PVA	CNC wt%	PVA wt%	Color ^a
124-186K	10.7	10.7	100;00	10.7	0	Y
124-186K	10.7	10.7	90;10	9.63	1.07	Y
124-186K	10.7	10.7	75;25	8.025	2.675	N
124-186K	10.7	10.7	50;50	5.35	5.35	N
124-186K	10.7	10.7	25;75	2.675	8.025	N
124-186K	10.7	10.7	0;100	0	10.7	N
124-186K	5	5	100;00	5	0	Y
124-186K	5	5	90;10	4.5	0.5	Y
124-186K	5	5	75;25	3.75	1.25	N
124-186K	5	5	50;50	2.5	2.5	N
124-186K	5	5	25;75	1.25	3.75	N
124-186K	5	5	0;100	0	5	N
124-186K	1	1	100;00	1	0	Y
124-186K	1	1	90;10	0.9	0.1	Y
124-186K	1	1	75;25	0.75	0.25	N
124-186K	1	1	50;50	0.5	0.5	N
124-186K	1	1	25;75	0.25	0.75	N
124-186K	1	1	0;100	0	1	N
89-98K	10.7	10.7	100;00	10.7	0	Y

89-98K	10.7	10.7	90;10	9.63	1.07	Y
89-98K	10.7	10.7	75;25	8.025	2.675	Y
89-98K	10.7	10.7	50;50	5.35	5.35	N
89-98K	10.7	10.7	25;75	2.675	8.025	N
89-98K	10.7	10.7	0;100	0	10.7	N
89-98K	5	5	100;00	5	0	Y
89-98K	5	5	90;10	4.5	0.5	Y
89-98K	5	5	75;25	3.75	1.25	Y
89-98K	5	5	50;50	2.5	2.5	N
89-98K	5	5	25;75	1.25	3.75	N
89-98K	5	5	0;100	0	5	N
89-98K	1	1	100;00	1	0	Y
89-98K	1	1	90;10	0.9	0.1	Y
89-98K	1	1	75;25	0.75	0.25	Y
89-98K	1	1	50;50	0.5	0.5	N
89-98K	1	1	25;75	0.25	0.75	N
89-98K	1	1	0;100	0	1	N

- a. Color appear (Y) defined for chiral nematic configuration and without any color (N) in composite should be for random configuration of liquid crystalline domains.

Table DS2: Nanocomposite Preparation Material Concentrations for Anisotropic Films.

Mw of PVA	Initial CNC wt%	Initial PVA wt%	CNC:PVA	CNC wt%	PVA wt%	Anisotropy
89-98K	12	12	100;00	12	0	Y
89-98K	12	12	90;10	10.8	1.2	Y
89-98K	12	12	75;25	9	3	Y
89-98K	12	12	50;50	6	6	N
89-98K	12	12	25;75	3	9	N
89-98K	12	12	0;100	0	12	N

CNC weight fraction (x):

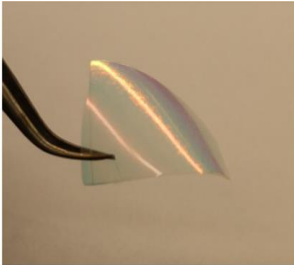
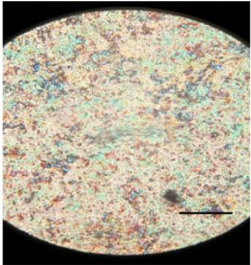
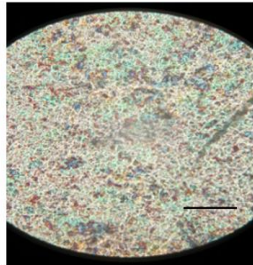
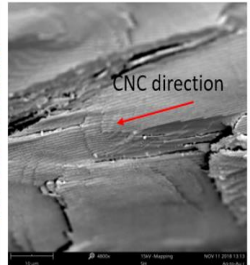

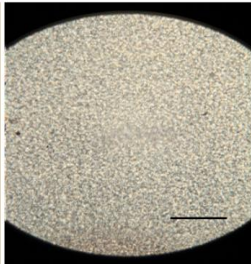
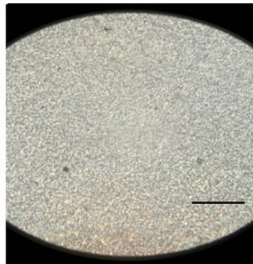
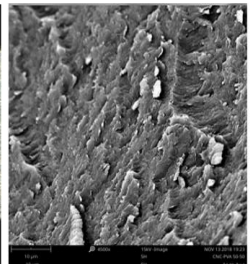

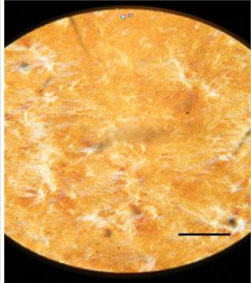
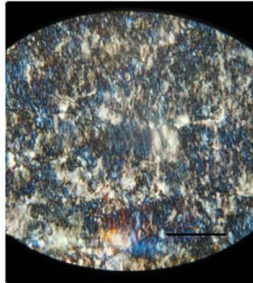
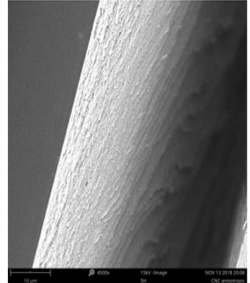
The EMT-CY model was actually developed to study the κ of semi-crystalline polymers that consist of axially symmetric crystallites embedded in an amorphous medium. We applied the same model for CNC-PVA nanocomposite assuming CNC as crystalline component and PVA as amorphous component. We are adding CNCs with PVA at a known content (CNC weight % of 75%), therefore the value of x is 0.75.

Table DS3: Properties of PVA raw materials.

Types of PVA	Molecular weight (Mw) g/mol	Degree of hydrolysis, %	Crystallinity index, %
PVA-1	89-98K	99	37.3
PVA-2	146-186K	87-89	29.95

Phase morphology for CNC-PVA composite films:

CNC-PVA compositions can form both isotropic (chiral nematic or random) and anisotropic configuration that is determined by CNC-PVA composition ratio, the molecular weight of PVA and the process condition. The investigation of CNC crystalline domains orientation with PVA long chains distribution is very challenging as both are organic materials. However, CNC-PVA (75:25) composition can form a chiral nematic arrangement with Mw 89-98K of PVA. The iridescent self-organized color was observed for a chiral nematic configuration and the SEM image also showed the layering and the pitch direction of the chiral nematic structure. Polarized optical images also confirm the presence of colorful domains in both dark field and bright field configuration. So, PVA long chains should be homogeneously dispersed in the CNC domains as the chiral nematic configuration is preserved. However, the random configuration and anisotropic films formed transparent films without showing any iridescence. SEM images of fracture samples showed a different morphology, and the dispersion of PVA chains in the CNC matrix is not observable. However, a similar optical micrograph was observed for random configuration in both dark field and bright field, hence, it is proved that no agglomeration is detected in the random configuration. It should be noted that a homogeneous distribution refers to similar optical micrographs for any configuration (dark field or bright field). Moreover, PVA is not responsive in linear polarized light at these thicknesses, hence, optical micrographs show different color intensity for non-uniform PVA distribution in CNC-PVA composite films. Based on the literature, anisotropic films also show a very intense color image for bright field configuration (45° to polarizers) and dark image for dark field configuration (0° or 90° to polarizers). Similar optical micrograph also observed for anisotropic CNC-PVA films. Therefore, PVA is also between CNCs due to the uniform optical intensity in the bright field configuration.

Composition (CNC: PVA)	Physical appearance	Polarized micrograph at 45°	Polarized micrograph at 0°	SEM at fracture surface
(75:25) with 89-98K PVA Isotropic (chiral nematic)				
(75:25) with 89-98K PVA Isotropic (random)				
(75:25) with 89-98K PVA anisotropic				

Scale bar = 100μm

Effect of interfacial resistance for cellulose nanocomposites:

For two component systems, total thermal conductivity of cellulose nanocomposites can be written as

$$T_{total} = T_{C^A} + T_{C^B} + R_{A-B} + T_s + D + A \dots \dots \dots (1)$$

Here,

T_{C^A} = Bulk thermal conductivity for Cellulose nanocrystal (CNC)

T_{C^B} = Bulk thermal conductivity for Polyvinyl Alcohol (PVA)

R_{A-B} = Thermal interface resistance between CNC & PVA

T_s = Orientation effect in thermal conductivity

D = Defects in bulk materials

A = Size of crystalline domains

However, crystalline domains size and defects factor can be eliminated as source materials, and fabrication process was fixed for this work. Therefore, order parameter and thermal interface resistance significantly control the overall κ in the bulk materials. Finally, we can also ignore the orientation effect (as it is known) to investigate the effect of thermal interface resistance between the CNC domains and PVA long chains.

In a non-compatible polymer blend, thermal interface resistance between polymer molecules must be higher than intramolecular thermal resistance. Therefore, heat conductivity for a binary system must follow a rule of mixture.

However, CNC and PVA can form a complete miscible polymer mixture due to their surface chemistry (-OH bond on the both polymer surfaces, hence, strong intramolecular H-bonding). It should be noted that strong H-bonding can reduced the thermal interfacial resistance, therefore, total κ of the polymer blend follows percolation theory rather than a simple rule of mixture

REFERENCES

1. Kaplan, D. L., Introduction to biopolymers from renewable resources. In *Biopolymers from renewable resources*, Springer: 1998; pp 1-29.
2. Yates, M. R.; Barlow, C. Y., Life cycle assessments of biodegradable, commercial biopolymers—A critical review. *Resources, Conservation and Recycling* **2013**, 78, 54-66.
3. Drzal, L. T.; Mohanty, A.; Misra, M., Bio-composite materials as alternatives to petroleum-based composites for automotive applications. *Magnesium* **2001**, 40 (60), 1.3-2.
4. Tabone, M. D.; Cregg, J. J.; Beckman, E. J.; Landis, A. E., Sustainability metrics: life cycle assessment and green design in polymers. *Environmental science & technology* **2010**, 44 (21), 8264-8269.
5. Moon, R. J.; Martini, A.; Nairn, J.; Simonsen, J.; Youngblood, J., Cellulose nanomaterials review: structure, properties and nanocomposites. *Chemical Society Reviews* **2011**, 40 (7), 3941-3994.
6. Beck-Candanedo, S.; Roman, M.; Gray, D. G., Effect of reaction conditions on the properties and behavior of wood cellulose nanocrystal suspensions. *Biomacromolecules* **2005**, 6 (2), 1048-1054.
7. Park, S.; Baker, J. O.; Himmel, M. E.; Parilla, P. A.; Johnson, D. K., Cellulose crystallinity index: measurement techniques and their impact on interpreting cellulase performance. *Biotechnology for biofuels* **2010**, 3 (1), 10.
8. Elazzouzi-Hafraoui, S.; Nishiyama, Y.; Putaux, J.-L.; Heux, L.; Dubreuil, F.; Rochas, C., The shape and size distribution of crystalline nanoparticles prepared by acid hydrolysis of native cellulose. *Biomacromolecules* **2007**, 9 (1), 57-65.
9. Leonardo, J.; Shishehbor, M.; Zavattieri, P. D., Mechanics of Crystalline Nano Cellulose Nanofilm. **2017**.
10. Shishehbor, M.; Zavattieri, P. D., Effects of interface properties on the mechanical properties of bio-inspired cellulose nanocrystal (CNC)-based materials. *Journal of the Mechanics and Physics of Solids* **2019**, 124, 871-896.
11. Chowdhury, R. A.; Rai, A.; Glynn, E.; Morgan, P.; Moore, A. L.; Youngblood, J. P., Superior, processing-dependent thermal conductivity of cellulose Nanocrystal-Poly (vinyl alcohol) composite films. *Polymer* **2019**, 164, 17-25.
12. Le Bras, D.; Strømme, M.; Mihranyan, A., Characterization of dielectric properties of nanocellulose from wood and algae for electrical insulator applications. *The Journal of Physical Chemistry B* **2015**, 119 (18), 5911-5917.
13. Chowdhury, R. A.; Nuruddin, M.; Clarkson, C.; Montes, F.; Howarter, J.; Youngblood, J. P., Cellulose Nanocrystal (CNC) Coatings with Controlled Anisotropy as High-Performance Gas Barrier Films. *ACS applied materials & interfaces* **2018**, 11 (1), 1376-1383.
14. Guidetti, G.; Atifi, S.; Vignolini, S.; Hamad, W. Y., Flexible photonic cellulose nanocrystal films. *Advanced Materials* **2016**, 28 (45), 10042-10047.
15. Charreau, H.; L Foresti, M.; Vázquez, A., Nanocellulose patents trends: a comprehensive review on patents on cellulose nanocrystals, microfibrillated and bacterial cellulose. *Recent patents on nanotechnology* **2013**, 7 (1), 56-80.

16. Duran, N.; Paula Lemes, A.; B Seabra, A., Review of cellulose nanocrystals patents: preparation, composites and general applications. *Recent patents on nanotechnology* **2012**, 6 (1), 16-28.
17. Siqueira, G.; Bras, J.; Dufresne, A., Cellulosic bionanocomposites: a review of preparation, properties and applications. *Polymers* **2010**, 2 (4), 728-765.
18. Peng, B. L.; Dhar, N.; Liu, H.; Tam, K., Chemistry and applications of nanocrystalline cellulose and its derivatives: a nanotechnology perspective. *The Canadian Journal of Chemical Engineering* **2011**, 89 (5), 1191-1206.
19. S ndergaard, R. R.; H sel, M.; Krebs, F. C., Roll-to-Roll fabrication of large area functional organic materials. *Journal of Polymer Science Part B: Polymer Physics* **2013**, 51 (1), 16-34.
20. Krebs, F. C.; Tromholt, T.; J rgensen, M., Upscaling of polymer solar cell fabrication using full roll-to-roll processing. *Nanoscale* **2010**, 2 (6), 873-886.
21. Jain, K.; Klosner, M.; Zemel, M.; Raghunandan, S., Flexible electronics and displays: high-resolution, roll-to-roll, projection lithography and photoablation processing technologies for high-throughput production. *Proceedings of the IEEE* **2005**, 93 (8), 1500-1510.
22. S ndergaard, R.; H sel, M.; Angmo, D.; Larsen-Olsen, T. T.; Krebs, F. C., Roll-to-roll fabrication of polymer solar cells. *Materials today* **2012**, 15 (1-2), 36-49.
23. Willmann, J.; Stocker, D.; D rsam, E., Characteristics and evaluation criteria of substrate-based manufacturing. Is roll-to-roll the best solution for printed electronics? *Organic Electronics* **2014**, 15 (7), 1631-1640.
24. Tracton, A. A., *Coatings technology handbook*. CRC press: 2005.
25. Diaz, J. A.; Ye, Z.; Wu, X.; Moore, A. L.; Moon, R. J.; Martini, A.; Boday, D. J.; Youngblood, J. P., Thermal conductivity in nanostructured films: from single cellulose nanocrystals to bulk films. *Biomacromolecules* **2014**, 15 (11), 4096-4101.
26. Isogai, A.; Saito, T.; Fukuzumi, H., TEMPO-oxidized cellulose nanofibers. *nanoscale* **2011**, 3 (1), 71-85.
27. Liu, J. C.; Martin, D. J.; Moon, R. J.; Youngblood, J. P., Enhanced thermal stability of biomedical thermoplastic polyurethane with the addition of cellulose nanocrystals. *Journal of Applied Polymer Science* **2015**, 132 (22).
28. Peng, S. X.; Moon, R. J.; Youngblood, J. P., Design and characterization of cellulose nanocrystal-enhanced epoxy hardeners. *Green Materials* **2014**, 2 (4), 193-205.
29. Yoo, Y.; Martinez, C.; Youngblood, J. P., Sustained dye release using poly (urea-urethane)/cellulose nanocrystal composite microcapsules. *Langmuir* **2017**, 33 (6), 1521-1532.
30. Zhou, Y.; Khan, T. M.; Liu, J.-C.; Fuentes-Hernandez, C.; Shim, J. W.; Najafabadi, E.; Youngblood, J. P.; Moon, R. J.; Kippelen, B., Efficient recyclable organic solar cells on cellulose nanocrystal substrates with a conducting polymer top electrode deposited by film-transfer lamination. *Organic Electronics* **2014**, 15 (3), 661-666.
31. Chindawong, C.; Johannsmann, D., An anisotropic ink based on crystalline nanocellulose: Potential applications in security printing. *Journal of Applied Polymer Science* **2014**, 131 (22).
32. Lavoine, N.; Desloges, I.; Dufresne, A.; Bras, J., Microfibrillated cellulose-Its barrier properties and applications in cellulosic materials: A review. *Carbohydrate polymers* **2012**, 90 (2), 735-764.

33. Yoo, Y.; Youngblood, J. P., Tung oil wood finishes with improved weathering, durability, and scratch performance by addition of cellulose nanocrystals. *ACS applied materials & interfaces* **2017**, 9 (29), 24936-24946.
34. Reising, A. B.; Moon, R. J.; Youngblood, J. P., Effect of particle alignment on mechanical properties of neat cellulose nanocrystal films. *J Sci Technol For Prod Process* **2012**, 2 (6), 32-41.
35. Yang, X.; Cranston, E. D., Chemically cross-linked cellulose nanocrystal aerogels with shape recovery and superabsorbent properties. *Chemistry of Materials* **2014**, 26 (20), 6016-6025.
36. Dong, H.; Snyder, J. F., Nanocellulose foam containing active ingredients. Google Patents: 2013.
37. Chen, S.; Schueneman, G.; Pipes, R. B.; Youngblood, J.; Moon, R. J., Effects of crystal orientation on cellulose nanocrystals–cellulose acetate nanocomposite fibers prepared by dry spinning. *Biomacromolecules* **2014**, 15 (10), 3827-3835.
38. Chowdhury, R. A.; Peng, S. X.; Youngblood, J., Improved order parameter (alignment) determination in cellulose nanocrystal (CNC) films by a simple optical birefringence method. *Cellulose* **2017**, 24 (5), 1957-1970.
39. Diaz, J. A.; Wu, X.; Martini, A.; Youngblood, J. P.; Moon, R. J., Thermal expansion of self-organized and shear-oriented cellulose nanocrystal films. *Biomacromolecules* **2013**, 14 (8), 2900-2908.
40. Wicklein, B.; Kocjan, A.; Salazar-Alvarez, G.; Carosio, F.; Camino, G.; Antonietti, M.; Bergström, L., Thermally insulating and fire-retardant lightweight anisotropic foams based on nanocellulose and graphene oxide. *Nature nanotechnology* **2015**, 10 (3), 277.
41. Kalia, S.; Kaith, B.; Kaur, I., *Cellulose fibers: bio-and nano-polymer composites: green chemistry and technology*. Springer Science & Business Media: 2011.
42. Shrestha, S.; Diaz, J. A.; Ghanbari, S.; Youngblood, J. P., Hygroscopic swelling determination of cellulose nanocrystal (CNC) films by polarized light microscopy digital image correlation. *Biomacromolecules* **2017**, 18 (5), 1482-1490.
43. Haywood, A. D.; Davis, V. A., Effects of liquid crystalline and shear alignment on the optical properties of cellulose nanocrystal films. *Cellulose* **2017**, 24 (2), 705-716.
44. Orts, W.; Godbout, L.; Marchessault, R.; Revol, J.-F., Enhanced ordering of liquid crystalline suspensions of cellulose microfibrils: A small angle neutron scattering study. *Macromolecules* **1998**, 31 (17), 5717-5725.
45. Park, J. H.; Noh, J.; Schütz, C.; Salazar-Alvarez, G.; Scalia, G.; Bergström, L.; Lagerwall, J. P., Macroscopic Control of Helix Orientation in Films Dried from Cholesteric Liquid-Crystalline Cellulose Nanocrystal Suspensions. *ChemPhysChem* **2014**, 15 (7), 1477-1484.
46. Cranston, E. D.; Gray, D. G., Birefringence in spin-coated films containing cellulose nanocrystals. *Colloids and Surfaces A: Physicochemical and Engineering Aspects* **2008**, 325 (1-2), 44-51.
47. Ahn, S. H.; Guo, L. J., High-speed roll-to-roll nanoimprint lithography on flexible plastic substrates. *Advanced materials* **2008**, 20 (11), 2044-2049.
48. Bae, S.; Kim, H.; Lee, Y.; Xu, X.; Park, J.-S.; Zheng, Y.; Balakrishnan, J.; Lei, T.; Kim, H. R.; Song, Y. I., Roll-to-roll production of 30-inch graphene films for transparent electrodes. *Nature nanotechnology* **2010**, 5 (8), 574.

49. Galagan, Y.; de Vries, I. G.; Langen, A. P.; Andriessen, R.; Verhees, W. J.; Veenstra, S. C.; Kroon, J. M., Technology development for roll-to-roll production of organic photovoltaics. *Chemical Engineering and Processing: Process Intensification* **2011**, 50 (5-6), 454-461.
50. Krebs, F. C., Polymer solar cell modules prepared using roll-to-roll methods: knife-over-edge coating, slot-die coating and screen printing. *Solar Energy Materials and Solar Cells* **2009**, 93 (4), 465-475.
51. Krebs, F. C.; Gevorgyan, S. A.; Alstrup, J., A roll-to-roll process to flexible polymer solar cells: model studies, manufacture and operational stability studies. *Journal of Materials Chemistry* **2009**, 19 (30), 5442-5451.
52. Lewis, B. G.; Paine, D. C., Applications and processing of transparent conducting oxides. *MRS bulletin* **2000**, 25 (8), 22-27.
53. Kumar, V.; Elfving, A.; Koivula, H.; Bousfield, D.; Toivakka, M., Roll-to-roll processed cellulose nanofiber coatings. *Industrial & Engineering Chemistry Research* **2016**, 55 (12), 3603-3613.
54. Rantanen, J. J.; Dimic-Misic, K.; Pirttiniemi, J.; Kuosmanen, P.; Maloney, T. C., Forming and dewatering of a microfibrillated cellulose composite paper. *BioResources* **2015**, 10 (2), 3492-3506.
55. Gardner, D. J.; Oporto, G. S.; Mills, R.; Samir, M. A. S. A., Adhesion and surface issues in cellulose and nanocellulose. *Journal of Adhesion Science and Technology* **2008**, 22 (5-6), 545-567.
56. Kumar, S., Liquid transfer in printing processes: liquid bridges with moving contact lines. *Annual Review of Fluid Mechanics* **2015**, 47, 67-94.
57. Dodds, S.; Carvalho, M. d. S.; Kumar, S., Stretching and slipping of liquid bridges near plates and cavities. *Physics of Fluids* **2009**, 21 (9), 092103.
58. Dodds, S.; Carvalho, M.; Kumar, S., Stretching liquid bridges with moving contact lines: The role of inertia. *Physics of Fluids* **2011**, 23 (9), 092101.
59. Patel, R.; Benkreira, H., Gravure roll coating of Newtonian liquids. *Chemical engineering science* **1991**, 46 (3), 751-756.
60. Hewson, R.; Kapur, N.; Gaskell, P., A two-scale model for discrete cell gravure roll coating. *Chemical engineering science* **2011**, 66 (16), 3666-3674.
61. Huang, W.-X.; Lee, S.-H.; Sung, H. J.; Lee, T.-M.; Kim, D.-S., Simulation of liquid transfer between separating walls for modeling micro-gravure-offset printing. *International Journal of Heat and Fluid Flow* **2008**, 29 (5), 1436-1446.
62. Hewson, R.; Kapur, N.; Gaskell, P., Tri-helical gravure roll coating. *Chemical Engineering Science* **2010**, 65 (4), 1311-1321.
63. Kapur, N., A parametric study of direct gravure coating. *Chemical engineering science* **2003**, 58 (13), 2875-2882.
64. Kendall, K., The adhesion and surface energy of elastic solids. *Journal of Physics D: Applied Physics* **1971**, 4 (8), 1186.
65. Lerouge, S.; Barrette, J.; Ruiz, J. C.; Sbai, M.; Savoji, H.; Saoudi, B.; Gauthier, M.; Wertheimer, M. R., Nitrogen-Rich Plasma Polymer Coatings for Biomedical Applications: Stability, Mechanical Properties and Adhesion Under Dry and Wet Conditions. *Plasma Processes and Polymers* **2015**, 12 (9), 882-895.
66. Chiang, M. Y.; Song, R.; Crosby, A. J.; Karim, A.; Chiang, C. K.; Amis, E. J., Combinatorial approach to the edge delamination test for thin film reliability—adaptability and variability. *Thin Solid Films* **2005**, 476 (2), 379-385.

67. Beck, S.; Bouchard, J.; Chauve, G.; Berry, R., Controlled production of patterns in iridescent solid films of cellulose nanocrystals. *Cellulose* **2013**, *20* (3), 1401-1411.
68. Kim, J.; Peretti, J.; Lahlil, K.; Boilot, J. P.; Gacoin, T., Optically Anisotropic Thin Films by Shear-Oriented Assembly of Colloidal Nanorods. *Advanced Materials* **2013**, *25* (24), 3295-3300.
69. Chowdhury, R. A.; Clarkson, C.; Youngblood, J., Continuous roll-to-roll fabrication of transparent cellulose nanocrystal (CNC) coatings with controlled anisotropy. *Cellulose* **2018**, *25* (3), 1769-1781.
70. Mäkelä, T.; Kainlahti, M.; Willberg-Keyriläinen, P.; Tammelin, T.; Forsström, U., Fabrication of micropillars on nanocellulose films using a roll-to-roll nanoimprinting method. *Microelectronic Engineering* **2016**, *163*, 1-6.
71. Abitbol, T.; Rivkin, A.; Cao, Y.; Nevo, Y.; Abraham, E.; Ben-Shalom, T.; Lapidot, S.; Shoseyov, O., Nanocellulose, a tiny fiber with huge applications. *Current opinion in biotechnology* **2016**, *39*, 76-88.
72. Li, F.; Biagioni, P.; Bollani, M.; Maccagnan, A.; Piergiovanni, L., Multi-functional coating of cellulose nanocrystals for flexible packaging applications. *Cellulose* **2013**, *20* (5), 2491-2504.
73. Sun, X.; Wu, Q.; Ren, S.; Lei, T., Comparison of highly transparent all-cellulose nanopaper prepared using sulfuric acid and TEMPO-mediated oxidation methods. *Cellulose* **2015**, *22* (2), 1123-1133.
74. He, J.; Liu, S.; Li, L.; Piao, G., Lyotropic liquid crystal behavior of carboxylated cellulose nanocrystals. *Carbohydrate polymers* **2017**, *164*, 364-369.
75. Vollick, B.; Kuo, P.-Y.; Alizadehgiashi, M.; Yan, N.; Kumacheva, E., From structure to properties of composite films derived from cellulose nanocrystals. *ACS Omega* **2017**, *2* (9), 5928-5934.
76. Habibi, Y.; Lucia, L. A.; Rojas, O. J., Cellulose nanocrystals: chemistry, self-assembly, and applications. *Chemical reviews* **2010**, *110* (6), 3479-3500.
77. Khan, A.; Khan, R. A.; Salmieri, S.; Le Tien, C.; Riedl, B.; Bouchard, J.; Chauve, G.; Tan, V.; Kamal, M. R.; Lacroix, M., Mechanical and barrier properties of nanocrystalline cellulose reinforced chitosan based nanocomposite films. *Carbohydrate polymers* **2012**, *90* (4), 1601-1608.
78. Slavutsky, A. M.; Bertuzzi, M. A., Water barrier properties of starch films reinforced with cellulose nanocrystals obtained from sugarcane bagasse. *Carbohydrate polymers* **2014**, *110*, 53-61.
79. Kumar, V.; Koppolu, V. R.; Bousfield, D.; Toivakka, M., Substrate role in coating of microfibrillated cellulose suspensions. *Cellulose* **2017**, *24* (3), 1247-1260.
80. Tang, J.; Sisler, J.; Grishkewich, N.; Tam, K. C., Functionalization of cellulose nanocrystals for advanced applications. *Journal of colloid and interface science* **2017**, *494*, 397-409.
81. Wong, W. S.; Salleo, A., *Flexible electronics: materials and applications*. Springer Science & Business Media: 2009; Vol. 11.
82. Kinnunen-Raudaskoski, K.; Hjelt, T.; Kenttä, E.; Forsström, U., Thin coatings for paper by foam coating. *Tappi J* **2014**, *13*, 9-19.
83. Lim, M.; Kwon, H.; Kim, D.; Seo, J.; Han, H.; Khan, S. B., Highly-enhanced water resistant and oxygen barrier properties of cross-linked poly (vinyl alcohol) hybrid films for packaging applications. *Progress in Organic Coatings* **2015**, *85*, 68-75.

84. Lee, S.-Y.; Mohan, D. J.; Kang, I.-A.; Doh, G.-H.; Lee, S.; Han, S. O., Nanocellulose reinforced PVA composite films: effects of acid treatment and filler loading. *Fibers and Polymers* **2009**, *10* (1), 77-82.
85. Mueller, S.; Sapkota, J.; Nicharat, A.; Zimmermann, T.; Tingaut, P.; Weder, C.; Foster, E. J., Influence of the nanofiber dimensions on the properties of nanocellulose/poly (vinyl alcohol) aerogels. *Journal of Applied Polymer Science* **2015**, *132* (13).
86. Tan, B.; Ching, Y.; Poh, S.; Abdullah, L.; Gan, S., A review of natural fiber reinforced poly (vinyl alcohol) based composites: Application and opportunity. *Polymers* **2015**, *7* (11), 2205-2222.
87. Mandal, A.; Chakrabarty, D., Studies on the mechanical, thermal, morphological and barrier properties of nanocomposites based on poly (vinyl alcohol) and nanocellulose from sugarcane bagasse. *Journal of Industrial and Engineering Chemistry* **2014**, *20* (2), 462-473.
88. Bhattacharya, A.; Ray, P., Studies on surface tension of poly (vinyl alcohol): effect of concentration, temperature, and addition of chaotropic agents. *Journal of applied polymer science* **2004**, *93* (1), 122-130.
89. Cen, J.; Kitsomboonloha, R.; Subramanian, V., Cell filling in gravure printing for printed electronics. *Langmuir* **2014**, *30* (45), 13716-13726.
90. Wang, P.-X.; Hamad, W. Y.; MacLachlan, M. J., Structure and transformation of tactoids in cellulose nanocrystal suspensions. *Nature communications* **2016**, *7*, 11515.
91. Schartel, B.; Wendling, J.; Wendorff, J., Cellulose/poly (vinyl alcohol) blends. 1. Influence of miscibility and water content on relaxations. *Macromolecules* **1996**, *29* (5), 1521-1527.
92. Fortunati, E.; Puglia, D.; Luzi, F.; Santulli, C.; Kenny, J. M.; Torre, L., Binary PVA bio-nanocomposites containing cellulose nanocrystals extracted from different natural sources: Part I. *Carbohydrate polymers* **2013**, *97* (2), 825-836.
93. Cozzolino, C. A.; Cerri, G.; Brundu, A.; Farris, S., Microfibrillated cellulose (MFC): pullulan bionanocomposite films. *Cellulose* **2014**, *21* (6), 4323-4335.
94. Damman, P.; Gabriele, S.; Coppée, S.; Desprez, S.; Villers, D.; Vilmin, T.; Raphaël, E.; Hamieh, M.; Al Akhrass, S.; Reiter, G., Relaxation of residual stress and reentanglement of polymers in spin-coated films. *Physical review letters* **2007**, *99* (3), 036101.
95. Farris, R. J.; Goldfarb, J.; Maden, M. A. In *The correlation between residual stresses and delamination behavior of polymer coatings*, Makromolekulare Chemie. Macromolecular Symposia, Wiley Online Library: 1993; pp 57-67.
96. Ching, Y. C.; Rahman, A.; Ching, K. Y.; Sukiman, N. L.; Cheng, H. C., Preparation and characterization of polyvinyl alcohol-based composite reinforced with nanocellulose and nanosilica. *BioResources* **2015**, *10* (2), 3364-3377.
97. Haugstad, G., Contrasting static-to-kinetic friction transitions on layers of an autophobically dewetted polymer film using Fourier-analyzed shear modulation force microscopy. *Tribology Letters* **2005**, *19* (1), 49-57.
98. Rickerby, D., A review of the methods for the measurement of coating-substrate adhesion. *Surface and coatings technology* **1988**, *36* (1-2), 541-557.
99. Sanchez-Garcia, M. D.; Lagaron, J. M., On the use of plant cellulose nanowhiskers to enhance the barrier properties of polylactic acid. *Cellulose* **2010**, *17* (5), 987-1004.
100. Wahyuningsih, K.; Iriani, E. S.; Fahma, F., Utilization of cellulose from pineapple leaf fibers as nanofiller in polyvinyl alcohol-based film. *Indonesian Journal of Chemistry* **2016**, *16* (2), 181-189.

101. Saxena, A.; Ragauskas, A. J., Water transmission barrier properties of biodegradable films based on cellulosic whiskers and xylan. *Carbohydrate polymers* **2009**, 78 (2), 357-360.
102. Aulin, C.; Salazar-Alvarez, G.; Lindström, T., High strength, flexible and transparent nanofibrillated cellulose–nanoclay biohybrid films with tunable oxygen and water vapor permeability. *Nanoscale* **2012**, 4 (20), 6622-6628.
103. Nair, S. S.; Zhu, J.; Deng, Y.; Ragauskas, A. J., High performance green barriers based on nanocellulose. *Sustainable Chemical Processes* **2014**, 2 (1), 23.
104. Ho, T. T.; Zimmermann, T.; Ohr, S.; Caseri, W. R., Composites of cationic nanofibrillated cellulose and layered silicates: water vapor barrier and mechanical properties. *ACS applied materials & interfaces* **2012**, 4 (9), 4832-4840.
105. Bedane, A. H.; Eić, M.; Farmahini-Farahani, M.; Xiao, H., Water vapor transport properties of regenerated cellulose and nanofibrillated cellulose films. *Journal of Membrane Science* **2015**, 493, 46-57.
106. Forrest, S. R., The path to ubiquitous and low-cost organic electronic appliances on plastic. *Nature* **2004**, 428 (6986), 911.
107. Khan, S.; Lorenzelli, L.; Dahiya, R. S., Technologies for printing sensors and electronics over large flexible substrates: a review. *IEEE Sensors Journal* **2015**, 15 (6), 3164-3185.
108. Leem, J. W.; Guan, X.-Y.; Choi, M.; Yu, J. S., Broadband and omnidirectional highly-transparent coverglasses coated with biomimetic moth-eye nanopatterned polymer films for solar photovoltaic system applications. *Solar Energy Materials and Solar Cells* **2015**, 134, 45-53.
109. Chen, Z.; Chen, Z.; Yang, Z.; Hu, J.; Yang, Y.; Chang, L.; Lee, L. J.; Xu, T., Preparation and characterization of vacuum insulation panels with super-stratified glass fiber core material. *Energy* **2015**, 93, 945-954.
110. Arora, A.; Padua, G., Nanocomposites in food packaging. *Journal of Food science* **2010**, 75 (1), R43-R49.
111. Silvestre, C.; Duraccio, D.; Cimmino, S., Food packaging based on polymer nanomaterials. *Progress in polymer science* **2011**, 36 (12), 1766-1782.
112. Humood, M.; Chowdhury, S.; Song, Y.; Tzeng, P.; Grunlan, J. C.; Polycarpou, A. A., Nanomechanical behavior of high gas barrier multilayer thin films. *ACS applied materials & interfaces* **2016**, 8 (17), 11128-11138.
113. Logothetidis, S., Flexible organic electronic devices: Materials, process and applications. *Materials Science and Engineering: B* **2008**, 152 (1-3), 96-104.
114. Michiels, Y.; Puyvelde, P.; Sels, B., Barriers and chemistry in a bottle: mechanisms in today's oxygen barriers for tomorrow's materials. *Applied Sciences* **2017**, 7 (7), 665.
115. Groner, M.; George, S.; McLean, R.; Carcia, P., Gas diffusion barriers on polymers using Al₂O₃ atomic layer deposition. *Applied Physics Letters* **2006**, 88 (5), 051907.
116. da Silva Sobrinho, A.; Czeremuszkin, G.; Latreche, M.; Wertheimer, M., Defect-permeation correlation for ultrathin transparent barrier coatings on polymers. *Journal of Vacuum Science & Technology A: Vacuum, Surfaces, and Films* **2000**, 18 (1), 149-157.
117. Yoo, B. M.; Shin, H. J.; Yoon, H. W.; Park, H. B., Graphene and graphene oxide and their uses in barrier polymers. *Journal of Applied Polymer Science* **2014**, 131 (1).
118. Graff, G. L.; Williford, R. E.; Burrows, P. E., Mechanisms of vapor permeation through multilayer barrier films: Lag time versus equilibrium permeation. *Journal of Applied Physics* **2004**, 96 (4), 1840-1849.

119. Priolo, M. A.; Gamboa, D.; Holder, K. M.; Grunlan, J. C., Super gas barrier of transparent polymer– clay multilayer ultrathin films. *Nano letters* **2010**, *10* (12), 4970-4974.
120. Dou, Y.; Xu, S.; Liu, X.; Han, J.; Yan, H.; Wei, M.; Evans, D. G.; Duan, X., Transparent, flexible films based on layered double hydroxide/cellulose acetate with excellent oxygen barrier property. *Advanced Functional Materials* **2014**, *24* (4), 514-521.
121. Xiang, F.; Givens, T. M.; Ward, S. M.; Grunlan, J. C., Elastomeric polymer multilayer thin film with sustainable gas barrier at high strain. *ACS applied materials & interfaces* **2015**, *7* (30), 16148-16151.
122. Song, Y.; Hagen, D. A.; Qin, S.; Holder, K. M.; Falke, K.; Grunlan, J. C., Edge charge neutralization of clay for improved oxygen gas barrier in multilayer nanobrick wall thin films. *ACS applied materials & interfaces* **2016**, *8* (50), 34784-34790.
123. Xiang, F.; Tzeng, P.; Sawyer, J. S.; Regev, O.; Grunlan, J. C., Improving the gas barrier property of clay–polymer multilayer thin films using shorter deposition times. *ACS applied materials & interfaces* **2013**, *6* (9), 6040-6048.
124. Laufer, G.; Kirkland, C.; Cain, A. A.; Grunlan, J. C., Clay–chitosan nanobrick walls: completely renewable gas barrier and flame-retardant nanocoatings. *ACS applied materials & interfaces* **2012**, *4* (3), 1643-1649.
125. Guin, T.; Stevens, B.; Kreckler, M.; D'Angelo, J.; Humood, M.; Song, Y.; Smith, R.; Polycarpou, A.; Grunlan, J. C., Ultrastrong, chemically resistant reduced graphene oxide-based multilayer thin films with damage detection capability. *ACS applied materials & interfaces* **2016**, *8* (9), 6229-6235.
126. Kim, H.; Miura, Y.; Macosko, C. W., Graphene/polyurethane nanocomposites for improved gas barrier and electrical conductivity. *Chemistry of Materials* **2010**, *22* (11), 3441-3450.
127. LeBaron, P. C.; Wang, Z.; Pinnavaia, T. J., Polymer-layered silicate nanocomposites: an overview. *Applied clay science* **1999**, *15* (1-2), 11-29.
128. Takahashi, S.; Goldberg, H.; Feeney, C.; Karim, D.; Farrell, M.; O'leary, K.; Paul, D., Gas barrier properties of butyl rubber/vermiculite nanocomposite coatings. *Polymer* **2006**, *47* (9), 3083-3093.
129. Choudalakis, G.; Gotsis, A., Permeability of polymer/clay nanocomposites: a review. *European polymer journal* **2009**, *45* (4), 967-984.
130. Lu, C.; Mai, Y.-W., Influence of aspect ratio on barrier properties of polymer-clay nanocomposites. *Physical review letters* **2005**, *95* (8), 088303.
131. Patel, N. P.; Miller, A. C.; Spontak, R. J., Highly CO₂-permeable and-selective membranes derived from crosslinked poly (ethylene glycol) and its nanocomposites. *Advanced Functional Materials* **2004**, *14* (7), 699-707.
132. Patel, N. P.; Miller, A. C.; Spontak, R. J., Highly CO₂-permeable and selective polymer nanocomposite membranes. *Advanced Materials* **2003**, *15* (9), 729-733.
133. Priolo, M. A.; Gamboa, D.; Grunlan, J. C., Transparent clay– polymer nano brick wall assemblies with tailorable oxygen barrier. *ACS Applied Materials & Interfaces* **2009**, *2* (1), 312-320.
134. Khan, A.; Huq, T.; Khan, R. A.; Riedl, B.; Lacroix, M., Nanocellulose-based composites and bioactive agents for food packaging. *Critical reviews in food science and nutrition* **2014**, *54* (2), 163-174.
135. Ferrer, A.; Pal, L.; Hubbe, M., Nanocellulose in packaging: Advances in barrier layer technologies. *Industrial Crops and Products* **2017**, *95*, 574-582.

136. Li, F.; Mascheroni, E.; Piergiovanni, L., The potential of nanocellulose in the packaging field: a review. *Packaging Technology and Science* **2015**, *28* (6), 475-508.
137. Zhu, H.; Xiao, Z.; Liu, D.; Li, Y.; Weadock, N. J.; Fang, Z.; Huang, J.; Hu, L., Biodegradable transparent substrates for flexible organic-light-emitting diodes. *Energy & Environmental Science* **2013**, *6* (7), 2105-2111.
138. Hubbe, M. A.; Ferrer, A.; Tyagi, P.; Yin, Y.; Salas, C.; Pal, L.; Rojas, O. J., Nanocellulose in thin films, coatings, and plies for packaging applications: A review. *BioResources* **2017**, *12* (1), 2143-2233.
139. Czichos, H.; Saito, T.; Smith, L., *Springer handbook of materials measurement methods*. Springer Berlin: 2006; Vol. 978.
140. Zeman, S.; Kubík, L., Permeability of polymeric packaging materials. *Technical Sciences/University of Warmia and Mazury in Olsztyn* **2007**, (10), 26-34.
141. Curro, J. G.; Honnell, K. G.; McCoy, J. D., Theory for the solubility of gases in polymers: application to monatomic solutes. *Macromolecules* **1997**, *30* (1), 145-152.
142. Belbekhouche, S.; Bras, J.; Siqueira, G.; Chappey, C.; Lebrun, L.; Khelifi, B.; Marais, S.; Dufresne, A., Water sorption behavior and gas barrier properties of cellulose whiskers and microfibrils films. *Carbohydrate Polymers* **2011**, *83* (4), 1740-1748.
143. Herrera, M. A.; Mathew, A. P.; Oksman, K., Gas permeability and selectivity of cellulose nanocrystals films (layers) deposited by spin coating. *Carbohydrate polymers* **2014**, *112*, 494-501.
144. Cui, Y.; Kumar, S.; Kona, B. R.; van Houcke, D., Gas barrier properties of polymer/clay nanocomposites. *Rsc Advances* **2015**, *5* (78), 63669-63690.
145. Car, A.; Stropnik, C.; Yave, W.; Peinemann, K. V., Tailor-made polymeric membranes based on segmented block copolymers for CO₂ separation. *Advanced Functional Materials* **2008**, *18* (18), 2815-2823.
146. Najari, S.; Hosseini, S. S.; Omidkhah, M.; Tan, N. R., Phenomenological modeling and analysis of gas transport in polyimide membranes for propylene/propane separation. *RSC Advances* **2015**, *5* (58), 47199-47215.
147. Kazarian, S. G.; Vincent, M. F.; Bright, F. V.; Liotta, C. L.; Eckert, C. A., Specific intermolecular interaction of carbon dioxide with polymers. *Journal of the American Chemical Society* **1996**, *118* (7), 1729-1736.
148. Börjesson, M.; Westman, G., Crystalline nanocellulose—preparation, modification, and properties. In *Cellulose-fundamental aspects and current trends*, IntechOpen: 2015.
149. Wind, J. D.; Sirard, S. M.; Paul, D. R.; Green, P. F.; Johnston, K. P.; Koros, W. J., Carbon dioxide-induced plasticization of polyimide membranes: pseudo-equilibrium relationships of diffusion, sorption, and swelling. *Macromolecules* **2003**, *36* (17), 6433-6441.
150. Bharadwaj, R. K., Modeling the barrier properties of polymer-layered silicate nanocomposites. *Macromolecules* **2001**, *34* (26), 9189-9192.
151. Peterlin, A., Dependence of diffusive transport on morphology of crystalline polymers. *Journal of Macromolecular Science, Part B: Physics* **1975**, *11* (1), 57-87.
152. Chen, H.; Ginzburg, V. V.; Yang, J.; Yang, Y.; Liu, W.; Huang, Y.; Du, L.; Chen, B., Thermal conductivity of polymer-based composites: Fundamentals and applications. *Progress in Polymer Science* **2016**, *59*, 41-85.
153. Hussain, A. R. J.; Alahyari, A. A.; Eastman, S. A.; Thibaud-Erkey, C.; Johnston, S.; Sobkowicz, M. J., Review of polymers for heat exchanger applications: Factors concerning thermal conductivity. *Applied Thermal Engineering* **2017**, *113*, 1118-1127.

154. Xue, Q.; Sun, J., Electrical conductivity and percolation behavior of polymer nanocomposites. In *Polymer Nanocomposites*, Springer: 2016; pp 51-82.
155. Liu, X.; Long, Y.-Z.; Liao, L.; Duan, X.; Fan, Z., Large-scale integration of semiconductor nanowires for high-performance flexible electronics. *ACS nano* **2012**, 6 (3), 1888-1900.
156. Zhou, Y.; Fuentes-Hernandez, C.; Khan, T. M.; Liu, J.-C.; Hsu, J.; Shim, J. W.; Dindar, A.; Youngblood, J. P.; Moon, R. J.; Kippelen, B., Recyclable organic solar cells on cellulose nanocrystal substrates. *Scientific reports* **2013**, 3, 1536.
157. Rule, D.; Smith, D.; Sparks, L. L. *Thermal conductivity of a polyimide film between 4.2 and 300K, with and without alumina particles as filler*; 1990.
158. Balachander, N.; Seshadri, I.; Mehta, R. J.; Schadler, L. S.; Borca-Tasciuc, T.; Keblinski, P.; Ramanath, G., Nanowire-filled polymer composites with ultrahigh thermal conductivity. *Applied Physics Letters* **2013**, 102 (9), 093117.
159. Yi, P.; Awang, R. A.; Rowe, W. S.; Kalantar-Zadeh, K.; Khoshmanesh, K., PDMS nanocomposites for heat transfer enhancement in microfluidic platforms. *Lab on a Chip* **2014**, 14 (17), 3419-3426.
160. Lee, P.; Lee, J.; Lee, H.; Yeo, J.; Hong, S.; Nam, K. H.; Lee, D.; Lee, S. S.; Ko, S. H., Highly stretchable and highly conductive metal electrode by very long metal nanowire percolation network. *Advanced materials* **2012**, 24 (25), 3326-3332.
161. Slee, D.; Stepan, J.; Wei, W.; Swart, J. In *Introduction to printed circuit board failures*, 2009 IEEE Symposium on Product Compliance Engineering, IEEE: 2009; pp 1-8.
162. Hanafi, M. Z. M.; Ismail, F. S.; Rosli, R. In *Radial plate fins heat sink model design and optimization*, 2015 10th Asian Control Conference (ASCC), IEEE: 2015; pp 1-5.
163. Bhanushali, S.; Jason, N. N.; Ghosh, P.; Ganesh, A.; Simon, G. P.; Cheng, W., Enhanced thermal conductivity of copper nanofluids: the effect of filler geometry. *ACS applied materials & interfaces* **2017**, 9 (22), 18925-18935.
164. Zhang, Y.; Heo, Y.-J.; Son, Y.-R.; In, I.; An, K.-H.; Kim, B.-J.; Park, S.-J., Recent advanced thermal interfacial materials: A review of conducting mechanisms and parameters of carbon materials. *Carbon* **2018**.
165. Zhang, Y.; Choi, J. R.; Park, S.-J., Enhancing the heat and load transfer efficiency by optimizing the interface of hexagonal boron nitride/elastomer nanocomposites for thermal management applications. *Polymer* **2018**, 143, 1-9.
166. Pratik, K.; Rai, A.; Ashton, T. S.; Moore, A. L., APCVD hexagonal boron nitride thin films for passive near-junction thermal management of electronics. *Nanotechnology* **2017**, 28 (50), 505705.
167. Rai, A.; Moore, A. L., Enhanced thermal conduction and influence of interfacial resistance within flexible high aspect ratio copper nanowire/polymer composites. *Composites Science and Technology* **2017**, 144, 70-78.
168. Alam, F. E.; Dai, W.; Yang, M.; Du, S.; Li, X.; Yu, J.; Jiang, N.; Lin, C.-T., In situ formation of a cellular graphene framework in thermoplastic composites leading to superior thermal conductivity. *Journal of Materials Chemistry A* **2017**, 5 (13), 6164-6169.
169. Wu, H.; Drzal, L. T., Graphene nanoplatelet paper as a light-weight composite with excellent electrical and thermal conductivity and good gas barrier properties. *Carbon* **2012**, 50 (3), 1135-1145.

170. Hamidinejad, S. M.; Chu, R. K.; Zhao, B.; Park, C. B.; Filleter, T., Enhanced Thermal Conductivity of Graphene Nanoplatelet–Polymer Nanocomposites Fabricated via Supercritical Fluid-Assisted in Situ Exfoliation. *ACS applied materials & interfaces* **2017**, *10* (1), 1225-1236.
171. Gonzalez-Gutierrez, J.; Duretek, I.; Kukla, C.; Poljšak, A.; Bek, M.; Emri, I.; Holzer, C., Models to predict the viscosity of metal injection molding feedstock materials as function of their formulation. *Metals* **2016**, *6* (6), 129.
172. Uetani, K.; Okada, T.; Oyama, H. T., Crystallite size effect on thermal conductive properties of nonwoven nanocellulose sheets. *Biomacromolecules* **2015**, *16* (7), 2220-2227.
173. Shimazaki, Y.; Miyazaki, Y.; Takezawa, Y.; Nogi, M.; Abe, K.; Ifuku, S.; Yano, H., Excellent thermal conductivity of transparent cellulose nanofiber/epoxy resin nanocomposites. *Biomacromolecules* **2007**, *8* (9), 2976-2978.
174. Uetani, K.; Okada, T.; Oyama, H. T., Thermally conductive and optically transparent flexible films with surface-exposed nanocellulose skeletons. *Journal of Materials Chemistry C* **2016**, *4* (41), 9697-9703.
175. Ureña-Benavides, E. E.; Ao, G.; Davis, V. A.; Kitchens, C. L., Rheology and phase behavior of lyotropic cellulose nanocrystal suspensions. *Macromolecules* **2011**, *44* (22), 8990-8998.
176. Chowdhury, R. A.; Clarkson, C.; Apalangya, V. A.; Islam, S. N.; Youngblood, J. P., Roll-to-roll fabrication of cellulose nanocrystal-poly (vinyl alcohol) composite coatings with controlled anisotropy. *Cellulose* **2018**, *25* (11), 6547-6560.
177. Benford, D.; Powers, T.; Moseley, S., Thermal conductivity of Kapton tape. *Cryogenics* **1999**, *39* (1), 93-95.
178. Lagerwall, J. P.; Schütz, C.; Salajkova, M.; Noh, J.; Park, J. H.; Scalia, G.; Bergström, L., Cellulose nanocrystal-based materials: from liquid crystal self-assembly and glass formation to multifunctional thin films. *NPG Asia Materials* **2014**, *6* (1), e80.
179. Dong, X. M.; Kimura, T.; Revol, J.-F.; Gray, D. G., Effects of ionic strength on the isotropic–chiral nematic phase transition of suspensions of cellulose crystallites. *Langmuir* **1996**, *12* (8), 2076-2082.
180. Kim, G.-H.; Lee, D.; Shanker, A.; Shao, L.; Kwon, M. S.; Gidley, D.; Kim, J.; Pipe, K. P., High thermal conductivity in amorphous polymer blends by engineered interchain interactions. *Nature materials* **2015**, *14* (3), 295.
181. Burger, N.; Laachachi, A.; Ferriol, M.; Lutz, M.; Toniazzi, V.; Ruch, D., Review of thermal conductivity in composites: mechanisms, parameters and theory. *Progress in Polymer Science* **2016**, *61*, 1-28.
182. Cahill, D. G.; Ford, W. K.; Goodson, K. E.; Mahan, G. D.; Majumdar, A.; Maris, H. J.; Merlin, R.; Phillpot, S. R., Nanoscale thermal transport. *Journal of applied physics* **2003**, *93* (2), 793-818.
183. Nan, C.-W.; Birringer, R., Determining the Kapitza resistance and the thermal conductivity of polycrystals: A simple model. *Physical Review B* **1998**, *57* (14), 8264.
184. Huxtable, S. T.; Cahill, D. G.; Shenogin, S.; Xue, L.; Ozisik, R.; Barone, P.; Usrey, M.; Strano, M. S.; Siddons, G.; Shim, M., Interfacial heat flow in carbon nanotube suspensions. *Nature materials* **2003**, *2* (11), 731.
185. Choy, C., Thermal conductivity of polymers. *Polymer* **1977**, *18* (10), 984-1004.
186. Cieloszyk, G.; Cruz, M.; Salinger, G., Thermal properties of dielectric solids below 4 K I—polycarbonate. *Cryogenics* **1973**, *13* (12), 718-721.

187. Choy, C.; Luk, W.; Chen, F., Thermal conductivity of highly oriented polyethylene. *Polymer* **1978**, *19* (2), 155-162.
188. Choy, C.; Young, K., Thermal conductivity of semicrystalline polymers—a model. *Polymer* **1977**, *18* (8), 769-776.
189. Choy, C.; Chen, F.; Luk, W., Thermal conductivity of oriented crystalline polymers. *Journal of Polymer Science: Polymer Physics Edition* **1980**, *18* (6), 1187-1207.
190. Brandrup, J.; Immergut, E. H.; Grulke, E. A.; Abe, A.; Bloch, D. R., *Polymer handbook*. Wiley New York: 1999; Vol. 89.

VITA

Reaz Chowdhury was born in Dhaka, Bangladesh. He received his B.S and M.S. degrees in Chemistry and Physical Chemistry from University of Dhaka, Dhaka, Bangladesh. He also received another M.S degree in Materials Science and Engineering from Tuskegee University, Alabama, U.S.A. Then, he went on to obtain his Ph.D. degree in Materials Engineering at Purdue University, West Lafayette, Indiana, U.S.A.